

MODELING DWARF SATELLITES OF THE MILKY WAY

by

SACHI WEERASOORIYA

Bachelor of Science, 2018
Midwestern State University
Wichita Falls, TX

Submitted to the Graduate Faculty of the
College of Science and Engineering
Texas Christian University
in partial fulfillment of the requirements
for the degree of

Master of Science

December 2020

Copyright by
Sachi Weerasooriya
2020

ACKNOWLEDGEMENTS

First and foremost, I would like to express my sincere gratitude to my advisor Dr. Mia Sauda Bovill for her immense support in conducting this research, for her kindness, patience, and knowledge. I am grateful for her support that extended beyond research to look out for her students. I would also like to thank Dr. Andrew Benson, the author of the semi-analytic model Galacticus for his support throughout this project from installing the package to understanding the code. I would not have been able to present this research without his guidance.

I would also like to thank the members of my thesis committee, Dr. Peter Frinchaboy, Dr. Kat Barger, and Dr. Hana Dobrovolny for their guidance in preparation of this work. Special thanks also goes to my undergraduate advisor Dr. Jackie Dunn who introduced me to research in dwarf galaxies.

I would like to thank my fellow graduate students for their support and company, especially my room mates Amy Ray, Natalie Myers, and former roommate Taylor Spoo. I would not have survived this time period without them. Special thanks also goes to my academic sister Alessa Ibrahim for her immense support during this process.

Last but not least I would like to thank my parents, my sisters, and brothers for their support. I would not be chasing my dreams without their help. I am in extreme debt to my sister Sandamali Weerasooriya for being an inspiration since my childhood and my elder sister Udayanthi Weerasooriya for always looking out for me like a second mother. Special thanks also goes to my high school physics teacher Mrs. Gayathri de Silva who was monumental in strengthening my goals towards learning Astronomy.

I would also like to acknowledge the University of Maryland supercomputing resources (<http://hpcc.umd.edu>) made available for conducting the research reported in this thesis. This work has also been benefitted by The Science & Engineering Research Center (SERC) grant for graduate students.

Contents

1	Introduction	1
1.1	Cosmology	3
1.1.1	Dark Matter	3
1.1.2	Dark Energy	4
1.2	Hierarchical Structure Formation of The Universe	5
1.3	Dwarf Galaxies and their Role in the Structure Formation of the Universe	6
1.4	Baryon Cycle	8
2	Computational Methods	10
2.1	Simulations	10
2.1.1	Building a Zoom Simulation	10
2.1.2	Milky Way Analog	11
2.2	Halo Finding	13
2.2.1	Friends Of Friends (FOF)	13
2.2.2	Spherical Overdensity Algorithms	15
2.2.3	ROCKSTAR vs AMIGA	15
2.3	Merger Tree Evolution	17
2.3.1	Consistent Trees	18
2.4	Modelling Physics of Star Formation	19
2.4.1	Semi-Analytic Modelling	19
3	Observational Sample	21
4	Results	35
4.1	Dependence on the Halo Finder	35
4.2	Gas Cooling	37
4.2.1	Cooling Rate Cutoff Velocity	37
4.3	Inflow of Baryons into Halos	38
4.3.1	Mass Accretion:	39
4.4	Molecular Clouds/Hot Halo Gas Cooling:	42
4.4.1	Cooling Functions:	43
4.5	Star Formation:	45
4.5.1	Metal Recycling:	46
4.5.2	Star Formation Rate	49

4.6	Outflow of Baryons	53
4.6.1	Tidal Stripping	53
4.6.2	Supernova Feedback	57
4.7	Best Fit Parameters	60
5	Discussion	62
5.0.1	Gas Cooling	62
5.0.2	Mass Accretion	62
5.0.3	Star Formation	63
5.0.4	Outflow of Baryons	63
5.1	Properties of Best Fit Model	64
6	Conclusion	71
7	Future Work	72
A	Halo Finders	74
A.1	AMIGA Halo Finder	74
A.2	ROCKSTAR Halo Finder	75
A.3	Other Parameters for Models based on AMIGA	75
A.3.1	Ram Pressure Stripping	75
A.3.2	Characteristic Velocity and Outflow Rate Exponent	78
A.3.3	Star Formation Laws	81
A.3.4	Initial Mass Function (IMF)	83

Vita

Abstract

List of Figures

1.1	We model the dwarf satellites of Milky Way in several stages. First, we run a dark matter only N-body simulation from ~ 100 million years after the big bang to present day. Next, we identify the halo boundaries and their properties using a halo finder. Then, we use a merger tree code to explore the merger history of the simulation. Finally, we introduce the stellar physics and galactic physics into the dark matter halos in the simulation using a Semi-Analytic Model (SAM). Properties of these galaxy models are then compared with observations from from McConnachie 2012 (October 2019 version). Figures in circled observations from (Taylor et al. 2016, Crnojevic 2020).	3
1.2	Comparison of galaxy distribution of the universe as predicted by the Millenium simulation with observations. The left and top slices shown in blue color are the observed galaxy distribution in our universe, gathered from the 2dF Galaxy Redshift Survey and the Sloan Digital Sky Survey respectively. Each dot inside the filaments represents a galaxy. The Earth is at the centre of the circle with distance increasing outward from the center. A redshift of 0.15 is approximately equal to a distance of 2 billion light years. Right and bottom slices of the circle colored in red shows the galaxy distribution on large scales computed using the Millennium Simulation assuming Λ CDM (Gerard Lemson & the Virgo Consortium 2020).	6
1.3	Baryon cycle for the Milky Way dwarf galaxies. Stage 1: cooling of gas inside the hot halo. Stage 2: cooled gas flows into the halo. Stage 3: the accreted material then form gas clouds. These gas clouds then start cooling due to molecular hydrogen and collisional ionization equilibrium. Stage 4: cooling of gas aids in the process of star formation. Stage 5: finally, some of the material inside halo flows back into the hot halo due to feedback effects such as tidal stripping, ram pressure stripping and supernovae.	9

2.1	Process of producing a zoom simulation. Step 1: Run a low resolution simulation and run the halo finder, Step 2: Identify candidate halos with the correct mass and right local environment, Step 3: Identify the Lagrange region. This is the region where progenitor particles of the present day host halo resides in the past, Step 4: Recenter the simulation box on the halo of interest using MUSIC (Hahn & Abel 2011), Step 5: Rerun the simulation with a higher resolution in the region of interest including a buffer zone.	12
2.2	Process of halo finding using Friends of friends (FOF) algorithm. Left: Simulation snapshot with dark matter particles: First, particles are grouped together based on their physical proximity and velocities. Here, the distance between particles and their velocities are used to calculate a linking length. If distance between a particle and a halo or two particles is less than this linking length, then they are grouped together. Right: Loosely bound particles are unbound using relative error in potential energy. Once, halo boundaries are identified the algorithm then calculate various properties of dark matter halos such as their mass, velocity, radius, etc. . . .	14
2.3	This figure shows how a spherical overdensity algorithm work. Top part of the figure shows how a halo boundary is identified. First, it calculates the density of the dark matter particles in the simulation and draws density contours. Once a threshold density is reached, it identifies the region enclosed as a halo. Loosely bound particles are unbound if the velocity of the particles are greater than their escape velocity. The plot below shows the density profile which gives the density of halos as a function of radius. Black dotted lines shows the density profile of the host halo while the red peaks shows density peaks of the sub halos. The algorithm identifies the density peaks of the sub-halos easily if they are located away from the center of the host halo.	16
2.4	Dark matter halo mass function of all the halos in the simulation for AMIGA and ROCKSTAR. AMIGA halo mass function is plotted in green color and ROCKSTAR halo mass function is colored in blue.	17
2.5	This figure shows the process of linking halos in the merger tree code consistent trees (Behroozi et al. 2013b). First, it identifies the dark matter particles in a halo at the present day (descendant halo). Then, it goes back in time to previous snapshot in the simulation to locate the halo which contains the most number of these same particles. Halo that contain these particles is called the progenitor halo. This process is repeated until the algorithm reaches the beginning of the simulation. If certain progenitors cannot be located, then positions and velocity of halos are used to gravitationally evolve their future/past positions and velocities to fix these links. Once every dark matter halo in the simulation is linked to their progenitor, a complete merger history of the simulation can be obtained.	19

3.1	Cumulative radial distribution of dwarf satellite galaxies orbiting within 400 kpc of the Milky Way. Y axis shows the number of galaxies (N) as a function of their distance from the galaxy’s center in kilo parsec (kpc). The observations are from updated data (October 2019) from McConnachie (2012).	23
3.2	Aitoff projection of the observed Milky Way Satellites. This figure marks dwarf satellites hosted by the Milky Way as seen in the sky from Helmut Jerjen. Jerjen, H., 2010, PASA, 29, 383.	24
3.3	Cumulative luminosity function for the Milky Way satellite dwarf galaxies orbiting within 400 kpc as a function of absolute V band magnitude (M_V). The black line shows the luminosity function that includes the Magellanic Clouds. Magellanic clouds are excluded since The dashed black line shows the luminosity function that do not include the Magellanic Clouds. N denotes the number of satellites galaxies per brightness bin. The observations are retrieved from updated data (October 2019) from McConnachie (2012)	30
3.4	Luminosity metallicity relation for the Milky Way satellite dwarf galaxies orbiting within 400 kpc as a function of absolute V band magnitude (M_V). The data points do not include the Magellanic Clouds. The observations are retrieved from updated data (October 2019) from McConnachie (2012).	31
3.5	Mass to light ratio of satellite dwarf galaxies orbiting Milky Way within 400 kpc (in solar units) as a function of absolute V band magnitude. The observations are from updated data (October 2019) from McConnachie (2012).	33
3.6	Velocity dispersion σ_* of satellite dwarf galaxies orbiting Milky Way within 400 kpc as a function of absolute V band magnitude. The observations are retrieved from updated data (October 2019) from McConnachie (2012).	34
4.1	We plot the cumulative luminosity function for the Milky Way satellite dwarf galaxies orbiting within 400 kpc as a function of absolute V band magnitude (M_V). The dashed black line shows the luminosity function that do not include the Magellanic Clouds. N denotes the number of satellites galaxies per brightness bin. The observations are retrieved from updated data (October 2019) of McConnachie (2012). Green curve shows the galaxy models based on AMIGA halo finder (best fit for observed luminosity function) and the blue curve shows the models based on ROCK-STAR halo finder	36
4.2	Cumulative luminosity function for the Milky Way satellite dwarf galaxies orbiting within 400 kpc as a function of absolute V band magnitude (M_V). The dashed black line shows the luminosity function that do not include the Magellanic Clouds. N denotes the number of satellites galaxies per brightness bin. The observations are retrieved from updated data (October 2019) of McConnachie (2012). Colored curves shows the galaxy models for various cooling rate cut off velocities with red curve showing the best fitting model	38

4.3	Cumulative luminosity function for the Milky Way satellite dwarf galaxies orbiting within 400 kpc as a function of absolute V band magnitude (M_V). The dashed black line shows the luminosity function that do not include the Magellanic Clouds. The observations are from (McConnachie 2012, see table 3.1). N denotes the number of satellites galaxies per brightness bin. Colored curves shows the preliminary galaxy models for different reionization suppression reshifts.	40
4.4	We plot the cumulative luminosity function for the Milky Way satellite dwarf galaxies orbiting within 400 kpc as a function of absolute V band magnitude (M_V). The dashed black line shows the luminosity function that do not include the Magellanic Clouds. N denotes the number of satellites galaxies per brightness bin. The observations are retrieved from updated Table 1 (October 2019) of McConnachie (2012). Colored curves shows the galaxy models for various reionization suppression velocities	42
4.5	Cumulative luminosity function for the Milky Way satellite dwarf galaxies orbiting within 400 kpc as a function of absolute V band magnitude (M_V). The dashed black line shows the luminosity function that do not include the Magellanic Clouds. N denotes the number of satellites galaxies per brightness bin. The observations are retrieved from updated data (October 2019) of McConnachie (2012). Colored curves shows the galaxy models for different cooling functions incorporated. Turquoise curve shows the model with cooling due collisional ionization equilibrium of atomic gas together with molecular hydrogen cooling while the blue curve shows cooling due to atomic collisional ionization equilibrium cooling. Both curves overlap with each other.	44
4.6	This figure shows the luminosity metallicity relation for the Milky Way satellite dwarf galaxies orbiting within 400 kpc as a function of absolute V band magnitude (M_V). The black dots shows the observed metallicity values. Note that these data do not include the Magellanic Clouds. The observations are retrieved from updated data (October 2019) of McConnachie (2012). Left: Turquoise dots shows the model with cooling due collisional ionization equilibrium of atomic gas together with molecular hydrogen cooling while the blue dots shows cooling due to atomic collisional ionization equilibrium cooling.	45
4.7	Cumulative luminosity function for the Milky Way satellite dwarf galaxies orbiting within 400 kpc as a function of absolute V band magnitude (M_V). The dashed black line shows the observed luminosity function that do not include the Magellanic Clouds. These observations are retrieved from updated data (October 2019) of McConnachie (2012). N denotes the number of satellites galaxies per brightness bin. Colored curves shows the galaxy models for different metal enrichment types. Blue curve shows the model with non-instantaneous form of metal enrichment while the yellow curve shows instantaneous form of metal enrichment.	48

4.8	Luminosity metallicity relation for the Milky Way satellite dwarf galaxies orbiting within 400 kpc as a function of absolute V band magnitude (M_V). The black dots shows the observed metallicity values from updated data (October 2019) of McConnachie (2012). Note that these data do not include the Magellanic Clouds. The observations are retrieved from updated table 1 (October 2019) of McConnachie (2012). Left: red dots shows the model with non-instantaneous metal enrichment. Right: blue dots shows instantaneous metal enrichment	49
4.9	Cumulative luminosity function for the Milky Way satellite dwarf galaxies orbiting within 400 kpc as a function of absolute V band magnitude (M_V). The dashed black line shows the observed luminosity function that do not include the Magellanic Clouds. These observations are from updated data (October 2019) of McConnachie (2012). N denotes the number of satellites galaxies per brightness bin. Colored curves shows the galaxy models for different star formation methods. Red curve shows the model with Extended-Schmidt empirical law while the orange curve shows Blitz Rosolowsky empirical law.	52
4.10	Luminosity metallicity relation for dwarf satellites galaxies of the Milky Way within 400 kpc. Observed values are shown in black dots. Observations from updated data (October 2019) of McConnachie (2012). Left: Galaxy model where star formation is determined by Extended-Schmidt empirical law. Right: Galaxy model with star formation determined by prescription Blitz Rosolowsky empirical law.	53
4.11	Cumulative luminosity function for the Milky Way satellite dwarf galaxies orbiting within 400 kpc as a function of absolute V band magnitude (M_V). The dashed black line shows the observed luminosity function that do not include the Magellanic Clouds. Observations are from updated data (October 2019) of McConnachie (2012). N denotes the number of satellites galaxies per brightness bin. Colored curves shows the galaxy models for galaxy models with non-tidal stripping and tidal stripping respectively. Green curve include only tidal stripping of dark matter while the red curve include tidal stripping of both dark matter and baryons.	56
4.12	Luminosity metallicity relation for the Milky Way satellite dwarf galaxies orbiting within 400 kpc as a function of absolute V band magnitude (M_V). The black dots shows the observed metallicity values. Note that these data do not include the Magellanic Clouds. The observations are retrieved from updated data (October 2019) of McConnachie (2012). Left: green dots shows the model without tidal stripping while the red dots shows galaxy models that include tidal stripping of baryons.	57

4.13	Cumulative luminosity function for the Milky Way satellite dwarf galaxies orbiting within 400 kpc as a function of absolute V band magnitude (M_V). The dashed black line shows the observed luminosity function that do not include the Magellanic Clouds. These observations are from updated data (October 2019) of McConnachie (2012). N denotes the number of satellites galaxies per brightness bin. Colored curves shows the galaxy models for galaxy models for different stellar feedback models. Power law in red and fixed method in green (with a fraction of 0.5).	60
5.1	Cumulative luminosity function for the Milky Way satellite dwarf galaxies orbiting within 400 kpc as a function of M_V . N denotes the number of satellites galaxies per brightness bin. The dashed black line shows the observed luminosity function that do not include the Magellanic Clouds. Observations are from McConnachie (2012) (see table 3.1). Galaxy models run with AMIGA and ROCKSTAR halo finder outputs are color coded with green and blue respectively.	65
5.2	Luminosity metallicity relation for the Milky Way satellite dwarf galaxies orbiting within 400 kpc as a function of M_V . The black dots shows the observed metallicity values retrieved from updated data (October 2019) of McConnachie (2012). Note that these data do not include the Magellanic Clouds. Green dots shows the model the current best fit galaxy model.	66
5.3	Velocity dispersion vs luminosity relation of Milky Way satellites. Black points represents the observations while green points represents the best fit galaxy model. See table 3.1 for observations from McConnachie (2012).	67
5.4	Mass to Light ratio of dwarf satellites orbiting Milky Way. We plot mass to light ratio of galaxies in solar units as a function of absolute V band magnitude. Black points represents the observations while green points represents the best fit galaxy model. See table 3.1 for observations from McConnachie (2012).	68
5.5	Luminosity vs half light radius relation of Milky Way satellites. Black points represents the observations while green points represents the best fit galaxy model. See table 3.1 for observations from McConnachie (2012).	69
5.6	Distance of the dwarf satellites orbiting Milky Way (in kpc) as a function of absolute V band magnitude. Observed distances are shown in black triangles. Green triangles shows the distances predicted by the best fit model. See table 3.1 for observations from McConnachie (2012).	70
A.1	Cumulative luminosity function for the Milky Way satellite dwarf galaxies orbiting within 400 kpc as a function of M_V . N denotes the number of satellites galaxies per brightness bin. The dashed black line shows the observed luminosity function that do not include the Magellanic Clouds. Observations are from McConnachie (2012) (see table 3.1). Colored lines shows the simulated dwarf galaxies for different ram pressure stripping efficiencies.	78

A.2	Luminosity function of dwarf satellites within 400 kpc of the Milky Way. Observations are from McConnachie (2012). See Table 3.1 for details. Colored curves represent simulated models with different characteristic velocities.	79
A.3	Luminosity function of dwarf satellites within 400 kpc of the Milky Way. Observations are from McConnachie (2012). See Table 3.1 for details. Colored curves represent simulated models with different outflow velocity exponents.	80
A.4	Luminosity function of galaxy models based on AMIGA with non-instantaneous stellar population for different characteristic velocities. (b)Luminosity function of galaxy models based on AMIGA with non-instantaneous stellar population for different outflow velocity exponents	81
A.5	Cumulative luminosity function for the Milky Way satellite dwarf galaxies orbiting within 400 kpc as a function of M_V . denotes the number of satellites galaxies per brightness bin. The dashed black line shows the observed luminosity function that do not include the Magellanic Clouds. Observations are from McConnachie (2012) (see Table 3.1). Colored curves shows the luminosity functions for different star formation rate density empirical laws.	83
A.6	Cumulative luminosity function of the simulated Milky Way satellites within 400 kpc for different initial mass functions. Number of satellites as a function of M_V . Black dashed curve shows the observed luminosity function. These observations are from updated data (October 2019) of McConnachie (2012). Colored curves shows luminosity functions for different IMFs.	84
A.7	Cumulative luminosity function for the Milky Way satellite dwarf galaxies orbiting within 400 kpc as a function of M_V . denotes the number of satellites galaxies per brightness bin. The dashed black line shows the observed luminosity function that do not include the Magellanic Clouds. Observations are from McConnachie (2012) (Table 3.1). Galaxy models run with different IMFs are shown in different colors. Top left: Chabrier 2001, Top right: Kennicutt 1983, Bottom left: Kroupa 2001, Bottom Right: Miller-Scalo 1979.	85

List of Tables

2.1	This table summarizes information on the halo finders, their type of algorithm, and time required to analyze one snapshot on a Mac mini. Note, each simulation has > 200 snapshots.	15
3.1	Sample of updated observations (October 2019) from McConnachie (2012). Summary of observed quantities for dwarf satellite galaxies orbiting within 400 kpc of Milky Way. Column 1: Galaxy name, Column 2: Right Ascension, Column 3: Declination, Column 4: Foreground reddening, Column 5: $E(B-V)$, measured directly from the Schlegel et al 1998 maps (they do not include the recalibration by Schlafly & Finbiener 2011), Column 6: Distance Modulus, $(m - M)_o$, Column 7: Heliocentric radial velocity, Column 8: Apparent V magnitude in Vega mags, Column 9: Position Angle of major axis in degrees measured east from north, Column 9: Projected ellipticity, Column 10: Central V surface brightness, Column 11: Half-light radius measured on major axis, Column 12: Stellar radial velocity dispersion, Column 13: Stellar peak/max rotation velocity, Column 14: Mass of HI (calculated for the adopted distance modulus), Column 15: HI radial velocity dispersion, Column 16: HI peak/max rotation velocity, Column 17: Stellar mean metallicity in dex.	25
3.1	Sample of updated observations (October 2019) from McConnachie (2012). Summary of observed quantities for dwarf satellite galaxies orbiting within 400 kpc of Milky Way. Column 1: Galaxy name, Column 2: Right Ascension, Column 3: Declination, Column 4: Foreground reddening, Column 5: $E(B-V)$, measured directly from the Schlegel et al 1998 maps (they do not include the recalibration by Schlafly & Finbiener 2011), Column 6: Distance Modulus, $(m - M)_o$, Column 7: Heliocentric radial velocity, Column 8: Apparent V magnitude in Vega mags, Column 9: Position Angle of major axis in degrees measured east from north, Column 9: Projected ellipticity, Column 10: Central V surface brightness, Column 11: Half-light radius measured on major axis, Column 12: Stellar radial velocity dispersion, Column 13: Stellar peak/max rotation velocity, Column 14: Mass of HI (calculated for the adopted distance modulus), Column 15: HI radial velocity dispersion, Column 16: HI peak/max rotation velocity, Column 17: Stellar mean metallicity in dex.	26

3.1	Sample of updated observations (October 2019) from McConnachie (2012). Summary of observed quantities for dwarf satellite galaxies orbiting within 400 kpc of Milky Way. Column 1: Galaxy name, Column 2: Right Ascension, Column 3: Declination, Column 4: Foreground reddening, Column 5: E(B-V), measured directly from the Schlegel et al 1998 maps (they do not include the recalibration by Schlafly & Finbiener 2011), Column 6: Distance Modulus, $(m - M)_o$, Column 7: Heliocentric radial velocity, Column 8: Apparent V magnitude in Vega mags, Column 9: Position Angle of major axis in degrees measured east from north, Column 9: Projected ellipticity, Column 10: Central V surface brightness, Column 11: Half-light radius measured on major axis, Column 12: Stellar radial velocity dispersion, Column 13: Stellar peak/max rotation velocity, Column 14: Mass of HI (calculated for the adopted distance modulus), Column 15: HI radial velocity dispersion, Column 16: HI peak/max rotation velocity, Column 17: Stellar mean metallicity in dex.	27
3.1	Sample of updated observations (October 2019) from McConnachie (2012). Summary of observed quantities for dwarf satellite galaxies orbiting within 400 kpc of Milky Way. Column 1: Galaxy name, Column 2: Right Ascension, Column 3: Declination, Column 4: Foreground reddening, Column 5: E(B-V), measured directly from the Schlegel et al 1998 maps (they do not include the recalibration by Schlafly & Finbiener 2011), Column 6: Distance Modulus, $(m - M)_o$, Column 7: Heliocentric radial velocity, Column 8: Apparent V magnitude in Vega mags, Column 9: Position Angle of major axis in degrees measured east from north, Column 9: Projected ellipticity, Column 10: Central V surface brightness, Column 11: Half-light radius measured on major axis, Column 12: Stellar radial velocity dispersion, Column 13: Stellar peak/max rotation velocity, Column 14: Mass of HI (calculated for the adopted distance modulus), Column 15: HI radial velocity dispersion, Column 16: HI peak/max rotation velocity, Column 17: Stellar mean metallicity in dex.	28
4.1	Summary of best fit parameters for satellite dwarf galaxies orbiting within 400 kpc of Milky Way. Note that these simulated models are based on AMIGA's halo finder.	61

Chapter 1

Introduction

Over the last several decades, numerous studies have expanded our knowledge of dwarf galaxies in the Milky Way (Albareti et al. 2017, Abbott et al. 2018), Andromeda (e.g. Aguado et al. 2019, Martin et al. 2016), and beyond the Local Group in larger mass galaxy clusters like Fornax (Rong et al. 2019) and Virgo (Cantiello et al. 2018). The Local Group (LG) is the region up to 1 Mpc from the center of Milky Way. It is dominated by the Milky Way and Andromeda (M31) galaxies (Karachentsev et al. 2002). The dwarf satellites of the Local Group show similar characteristics (Sawala et al. 2012), though recent work has shown some potential differences. Do these similarities extend across all environments? What about dwarf galaxies that live in intermediate mass environments between groups and clusters? Our final goal is to explore the dependence of stellar physics of dwarf galaxies on host environments. To specifically assess whether or not star formation in dwarf galaxies is universal across different environments. We begin the exploration of these concepts by modelling stellar physics of the well studied dwarf satellites of the Milky Way.

This Master's thesis focuses on constraining the parameter space for star formation physics of the Milky Way satellites, as our galaxy and its satellite population are very well studied, and the properties of its dwarf satellites are well known. Therefore, the Milky Way satellites are perfect laboratories to calibrate our model for low mass dwarf galaxies, since default parameters are not known for dwarf galaxies. They are lower mass compared to galaxies like the Milky Way. Thus, the physics governing star formation in dwarf galaxies is likely to be different from massive galaxies. Therefore, the purpose of our project is to calibrate a Semi Analytic Model (SAM). We use the SAM Galacticus by Benson (2011) to explore the physics of star formation in Milky Way satellites. The complete process we use to model galaxies is shown in Figure 1.1.

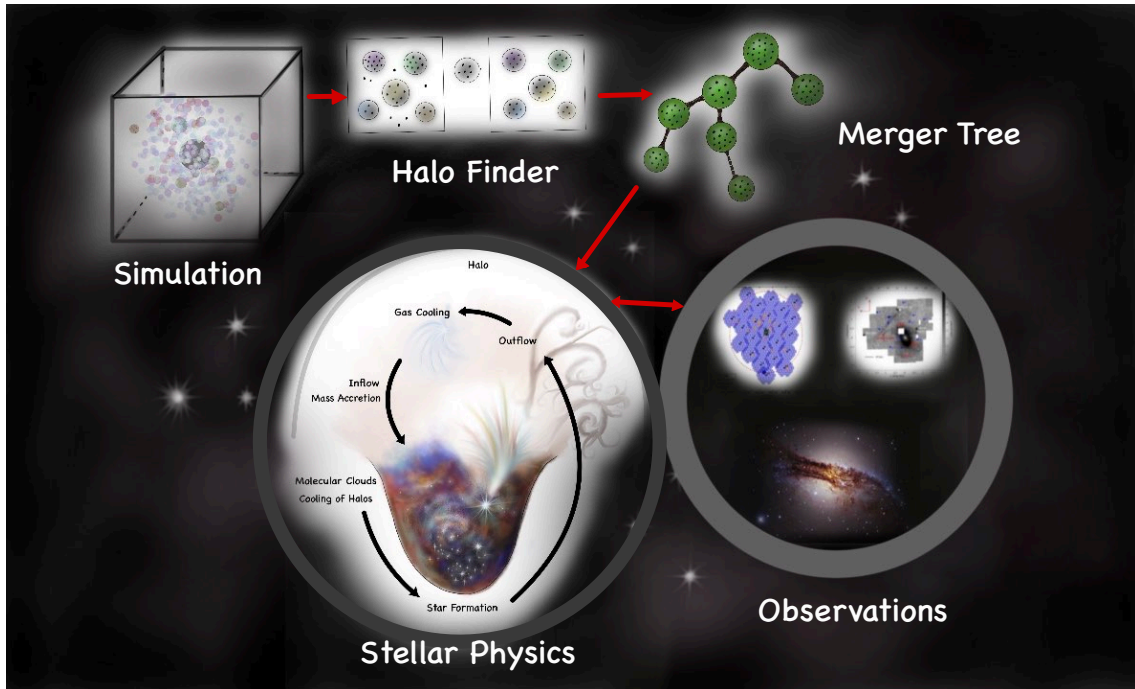


Figure 1.1: We model the dwarf satellites of Milky Way in several stages. First, we run a dark matter only N-body simulation from ~ 100 million years after the big bang to present day. Next, we identify the halo boundaries and their properties using a halo finder. Then, we use a merger tree code to explore the merger history of the simulation. Finally, we introduce the stellar physics and galactic physics into the dark matter halos in the simulation using a Semi-Analytic Model (SAM). Properties of these galaxy models are then compared with observations from from McConnachie 2012 (October 2019 version). Figures in circled observations from (Taylor et al. 2016, Crnojevic 2020).

1.1 Cosmology

Before discussing the details of the star formation physics of dwarf galaxies and how we model it, we will outline the underlying cosmology we assume for these simulations.

1.1.1 Dark Matter

Dark matter plays an important role in the formation and evolution of dwarf galaxies as they are the most dark matter dominant galaxies known. Specifically dwarf spheroidal

galaxies have few stars and little gas, and their velocity dispersions suggest that $> 99\%$ of their mass is made up of dark matter (van Dokkum et al. 2016). Dark matter is non-baryonic matter is observed only through its gravitational interactions with stars and gas. Roughly 90% of all the mass in the universe is thought to be dark matter as mass of gas and stars alone cannot account for the observed dynamics within galaxies. The most likely candidates for dark matter is the Weakly Interacting Massive Particles (WIMPs), while another possibility is Massive Compact Halo Objects (MACHOs) (Griest 2002).

1.1.2 Dark Energy

While dark matter plays an important role in the formation and evolution of dwarf galaxies, only 27% of the energy density of the universe is made of baryons and dark matter. The remaining 68% consists of dark energy (Planck Collaboration et al. 2016). Dark Energy is the energy associated with the vacuum of “empty” space itself that causes acceleration of the expansion of the universe. It is a repulsive force that counteracts gravity. While dark energy does not affect the evolution of dwarf galaxies, it governs the rate of expansion in the universe. The expansion of the universe causes the distance between galaxy clusters to increase with time, and determines how the universe will evolve with time.

1.2 Hierarchical Structure Formation of The Universe

Hierarchical structure formation is the process by which larger structures are formed through continuous merging of smaller structures. Lambda Cold Dark Matter Theory (Λ CDM) suggests that the universe was intensely hot ($\sim T > 10^{10}K$), smooth, and uniform just after the Big Bang (White 1988). This hot universe started out expanding relatively slowly for $10^{-36}s$ until the period known as inflation. During inflation time, subatomic quantum fluctuations became macroscopic, creating slight (10^{-5}) overdensities and underdensities of dark matter. When underdensities grow to five times the average density of the universe they became gravitationally unstable and collapse to form dark matter halos (Dalal et al. 2010). Since baryons follow gravity, gas and dust condense into potential wells of the dark matter to form stars. Over time, these first galaxies merged to form the galaxies seen today. Hence, small galaxies rich in dark matter are the building blocks of the observable universe (Frebel et al. 2010).

The hierarchical structure formation suggested by Λ CDM has been observed for large scale structure of the universe. Observers have seen filament like structure of galaxies in surveys such as 2dF Galaxy REdshift Survey (Colless 2002) and Sloan Digital Sky Survey (Albaret et al. 2017) (See Figure 1.2) and cosmological simulations reproduce the structure (Millenium (Boylan-Kolchin et al. 2009) and Illustris (Vogelsberger et al. 2014)). However, how structures form on the small scales of dwarf galaxies is not well constrained. Therefore, we need models and observations of these small galaxies to

expand our knowledge in structure formation of the universe.

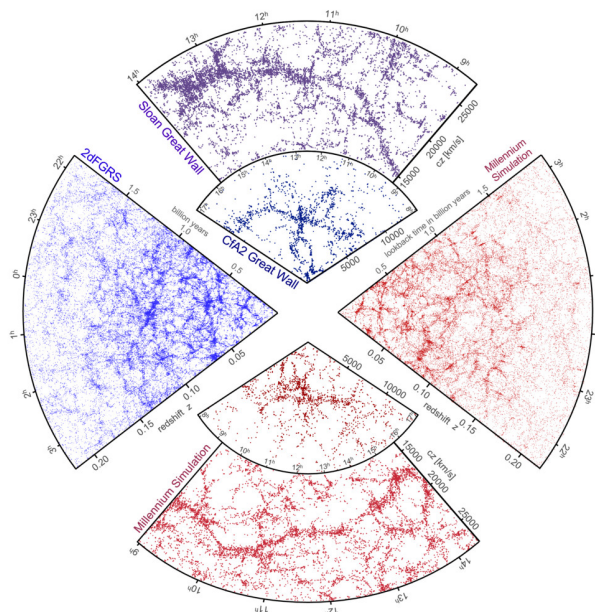


Figure 1.2: Comparison of galaxy distribution of the universe as predicted by the Millennium simulation with observations. The left and top slices shown in blue color are the observed galaxy distribution in our universe, gathered from the 2dF Galaxy Redshift Survey and the Sloan Digital Sky Survey respectively. Each dot inside the filaments represents a galaxy. The Earth is at the centre of the circle with distance increasing outward from the center. A redshift of 0.15 is approximately equal to a distance of 2 billion light years. Right and bottom slices of the circle colored in red shows the galaxy distribution on large scales computed using the Millennium Simulation assuming Λ CDM (Gerard Lemson & the Virgo Consortium 2020).

1.3 Dwarf Galaxies and their Role in the Structure Formation of the Universe

A dwarf galaxy is type of a galaxy that is fainter than $M_B \sim -16 \text{ mag}$ in absolute B band magnitudes (Tammann 1994) and at least ten thousand times smaller than the size of the Milky Way. Note that the absolute magnitude is a measure of the luminosity of a celestial object, on the inverse logarithmic astronomical magnitude scale. They have low surface

brightness and are the most abundant type of galaxies in the universe, and their observed number density of dwarf galaxies is largest near massive galaxies. However, the exact criteria for how low the luminosity and mass can be is not well understood and defined (McConnachie 2012). In addition, faint nature makes it harder to detect them without deep, targeted observations. According to Simon (2019), the faintest dwarf galaxies are less than $< 10^5 L_{\odot}$ (in units of solar luminosity) with dark matter masses $\sim 10^9 M_{\odot}$ (in units of solar masses). There are three main types of dwarf galaxies, dwarf spheroidal (dSph), dwarf irregulars (dIrr), and dwarf ellipticals (dE), based on their morphology (Lin & Murray 1994). Despite their low brightness and mass, they play a major role in the structure formation of the universe.

Dwarf galaxies have very shallow gravitational potentials (Lin & Murray 1994). Gravitational potential wells are responsible for capturing baryons inside galaxies. The shallow depth of the potential wells cause them to be very sensitive to feedback processes such as stellar winds, and supernova explosions. Their sensitivity to feedback makes them excellent probes of their local environment. Dwarf galaxies are the building blocks of larger galaxies. Dwarf galaxies surround their host galaxy eventually falling into the potential well of the host contributing to the growth of the host, forming a larger galaxy by accumulation of many dwarf galaxies. Stellar activity varies within greatly within these galaxies during this process it can greatly impact their structure. Even a relatively small scale stellar feedback process can expel stars and dust off a dwarf galaxy's potential. Shallow gravitational potentials of dwarf galaxies make them vulnerable to stellar feedback and turbulence. Hence, changes to their star-formation physics such as star

formation rate, supernovae feedback, are very apparent. Therefore, they are excellent probes of star formation physics in galaxies.

1.4 Baryon Cycle

The cycle of inflow and outflow of gas in galaxies, and the subsequent star formation, is fundamental to the evolution of galaxies. This baryon cycle describes how galaxies acquire, store, and expel baryons (e.g. gas, stars, dust) (Chisholm & Matsushita 2016). The baryon cycle (Figure 1.3) determines the star-formation in dark matter halos and establishes the star-formation history of the universe (Chisholm & Matsushita 2016, Oppenheimer & Davé 2008).

The first stage of the cycle starts with cooling gas into and in dark matter halos. As the gas in the Intergalactic Medium (IGM) cools down, gas accretes onto halos. Furthermore, galaxy mergers and interactions speed up the inflow process (Chisholm & Matsushita 2016, Springel et al. 2005). Once there is enough gas in halos, molecular hydrogen, atomic collisional ionization equilibrium processes, and metals in the halos cool the gas inside the halos. molecular gas clouds containing the effective coolant CO form, further gas cooling and precipitating star formation in the halos. Turbulence within these cold gas clouds gives rise gravitational instabilities within the cloud, that eventually collapse the gas cloud and form stars. The matter ejected by the feedback mechanisms such as supernova explosions goes back into the Interstellar Medium (ISM) of the galaxy and surrounding IGM to start the cycle again.

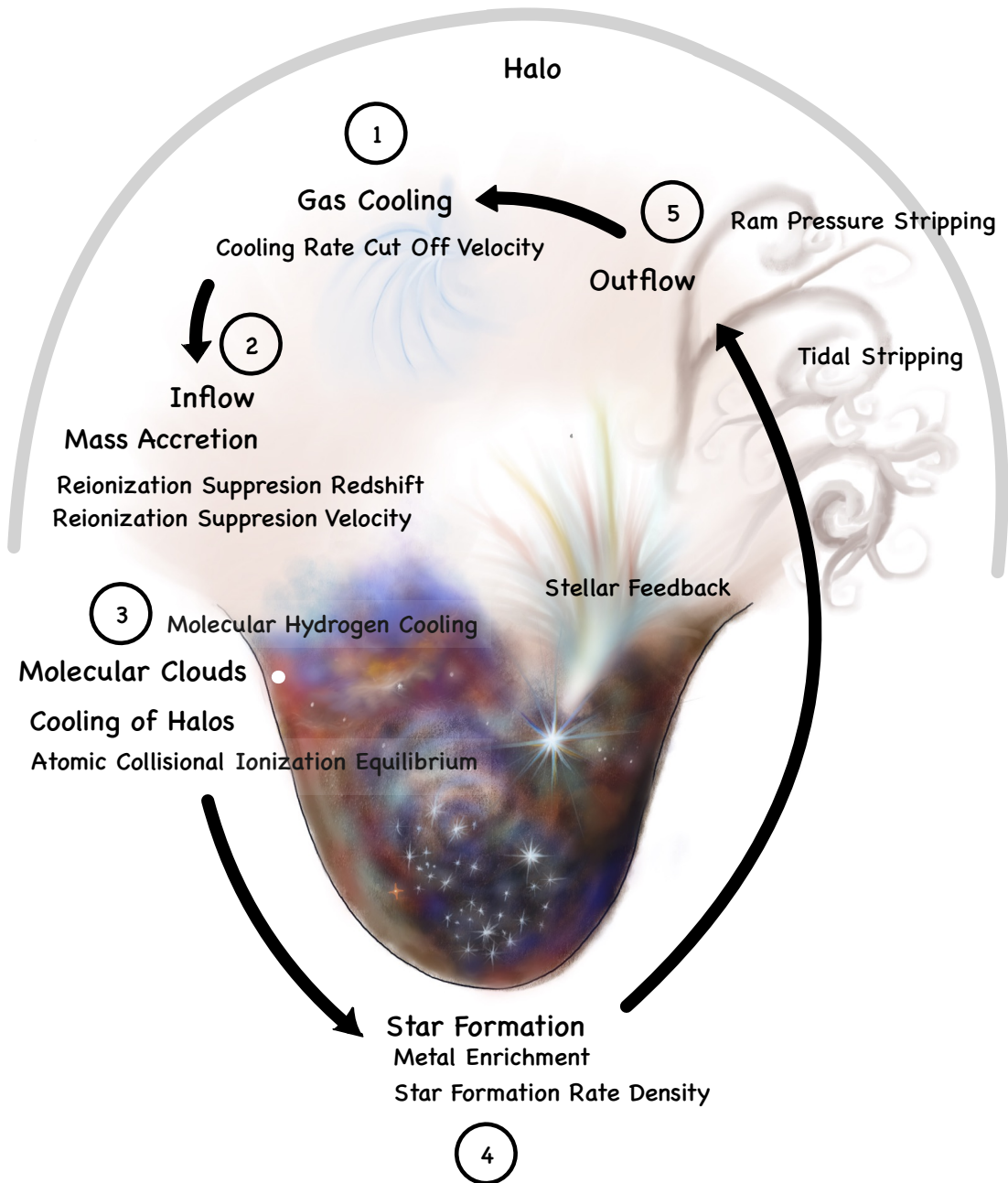


Figure 1.3: Baryon cycle for the Milky Way dwarf galaxies. Stage 1: cooling of gas inside the hot halo. Stage 2: cooled gas flows into the halo. Stage 3: the accreted material then form gas clouds. These gas clouds then start cooling due to molecular hydrogen and collisional ionization equilibrium. Stage 4: cooling of gas aids in the process of star formation. Stage 5: finally, some of the material inside halo flows back into the hot halo due to feedback effects such as tidal stripping, ram pressure stripping and supernovae.

Chapter 2

Computational Methods

2.1 Simulations

We use a N-body simulation of a Milky Way analog run with Gadget 2 code (Springel 2005) and analyzed with AMIGA (Knollmann & Knebe 2009), ROCKSTAR (Behroozi et al. 2013a), and `consistent_trees` (Behroozi et al. 2013b). Code testing and preliminary simulations were performed on the University of Maryland High Performance Computer Cluster Deepthought 2 (University of Maryland supercomputing resources (<http://hpcc.umd.edu>)). The host galaxy is selected to be a $\sim 10^{12} M_{\odot}$ halo with no massive halos within 3 Mpc (about 3 times the size of the Local Group).

2.1.1 Building a Zoom Simulation

While simulating a single Milky Way mass galaxy at the required resolution is computationally expensive, simulating a large representative volume of the Universe at the required resolution is computationally prohibitive. Hence, we zoom into the specific re-

gions of interest within a lower resolution cosmological simulation and rerun it at higher resolution. The procedure is as follows (Figure 2.1). First, we run a large low-resolution simulation and identify a candidate dark matter halo with the correct mass and local environment. Once the candidate halo is identified, we trace back the halo particles from the present day ($z = 0$) to the beginning of the simulation ($z = 150$). The region where these particles reside is called the Lagrange Region. Following the identification of the Lagrange Region, we recenter the host halo and generate new initial conditions using Multi Scale Initial Conditions (MUSIC) by Hahn & Abel (2011) and rerun the simulation at the higher resolution required.

2.1.2 Milky Way Analog

We run the Milky Way analog from about 100 million years after the Big Bang ($z = 150$) to the present day ($z = 0$), outputting a snapshot every 100 Myr. The simulation is initially run on a $50 \text{ Mpc } h^{-1}$ box with a low resolution ($N = 256^3$), resolving Milky Way candidates at $z = 0$ with > 1000 particles. We select Milky Way analogs with $M_{vir} \geq 10^{12} M_{\odot}$ ² within $3 \text{ Mpc } h^{-1}$ of Milky Way analog at present day ($z = 0$), with a region of interest four times the radius of the Milky Way dark matter halo (R_{vir}). Both Milky Way and Andromeda galaxies are located in dark matter halo of about $10^{12} M_{\odot}$ and located $\sim 800 \text{ kpc}$ apart (Garrison-Kimmel et al. 2014). Neither M31 or the Milky Way are within each others virial radii. Therefore, it is safe to assume that presence (or absence) of an Andromeda galaxy (M31) analog in our simulations will not affect the

¹ $\text{Mpc } h^{-1}$ gives the distance in comoving units. It factors out the expansion of space.

²Virial radius (R_{vir}) is the radius at which the dark matter particles are gravitationally bound to the dark matter halo. It is the radius at which the enclosed density drops below 200 times the background density. Virial mass (M_{Vir}) is the mass enclosed within the virial radius

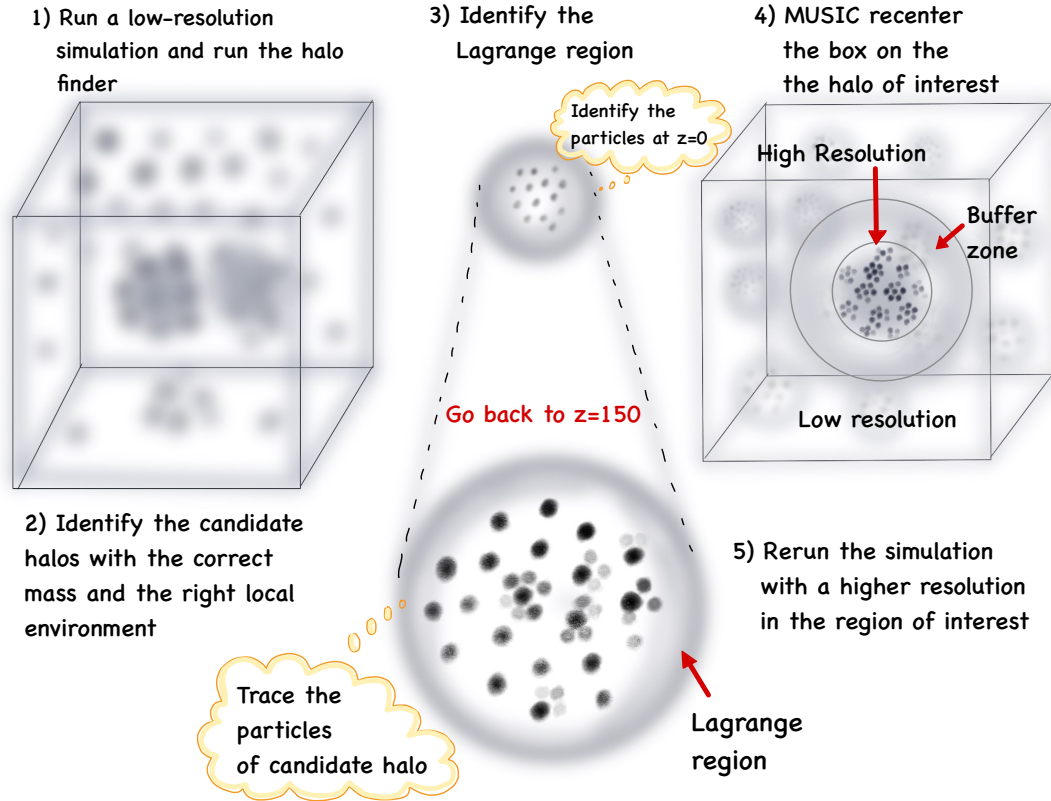


Figure 2.1: Process of producing a zoom simulation. Step 1: Run a low resolution simulation and run the halo finder, Step 2: Identify candidate halos with the correct mass and right local environment, Step 3: Identify the Lagrange region. This is the region where progenitor particles of the present day host halo resides in the past, Step 4: Recenter the simulation box on the halo of interest using MUSIC (Hahn & Abel 2011), Step 5: Rerun the simulation with a higher resolution in the region of interest including a buffer zone.

properties and distribution of the dwarf satellites within the virial halo of the Milky Way.

In addition, we are constrained by the computational resources. Even if we have a Local Group analog in our low resolution box, it may not remain as a Local Group analog when simulation is rerun at higher resolutions. As a result, it is standard practice to simulate isolated analogs of the Milky Way (e.g. Springel et al. 2008, Gottloeber et al. 2010, Bovill & Ricotti 2011, Hopkins et al. 2014, Akins et al. 2020). Only the proprietary simulations ELVIS suite of simulations simulate Local Group analogs (Garrison-Kimmel et al. 2014).

Once Milky Way analog is identified at $z = 0$, particles belonging to that halo are traced to the $z = 150$ snapshot. We then perform a resimulation on the lagrangian region up to with new initial conditions at a higher resolution ($N^3 = 4096^3$) resolving all halos with $M_{vir} > 10^7 M_\odot$ in the highest resolution region.

2.2 Halo Finding

Halo finders identify dark-matter halos in the simulation and calculate the halo properties such as virial radius, mass, circular velocity, etc. We use two halo finders: (1) Robust Overdensity Calculation using K-Space Topologically Adaptive Refinement, (ROCKSTAR, Behroozi et al. 2013a) and (2) Adaptive Mesh Investigations of Galaxy Assembly, (AMIGA, Knollmann & Knebe 2009) to identify the dark matter halos. These two halo finders use two different algorithms, phase space Friends of Friends (FOF) and spherical overdensity algorithms, respectively. See Appendix A for more details of the halo finders.

2.2.1 Friends Of Friends (FOF)

Friends of Friends algorithms use positions and velocities in 6D space to identify particles within an adaptive linking length and group particles into halos (Figure 2.2). Specifically, ROCKSTAR (Behroozi et al. 2013a) applies this algorithm as follows. First, the simulation volume is divided into 3D FOF groups, groups in which particles are within the linking length in position space. For each 3D FOF group, particle positions and velocities are divided by the group positions and velocity dispersion. This process repeats for each

³ N is the number of particles in the simulation as if the entire $50 \text{ Mpc} h^{-1}$ box were simulated at the highest resolution.

subgroup and a new level of substructure is calculated. Once all levels of substructure are identified, particles are assigned hierarchically to the closest halo in both position and velocity space. Then, unbound particles are removed based on which particles have the minimum gravitational potential. Finally, halo properties such as virial radius, virial mass, maximum circular velocity etc. are calculated.

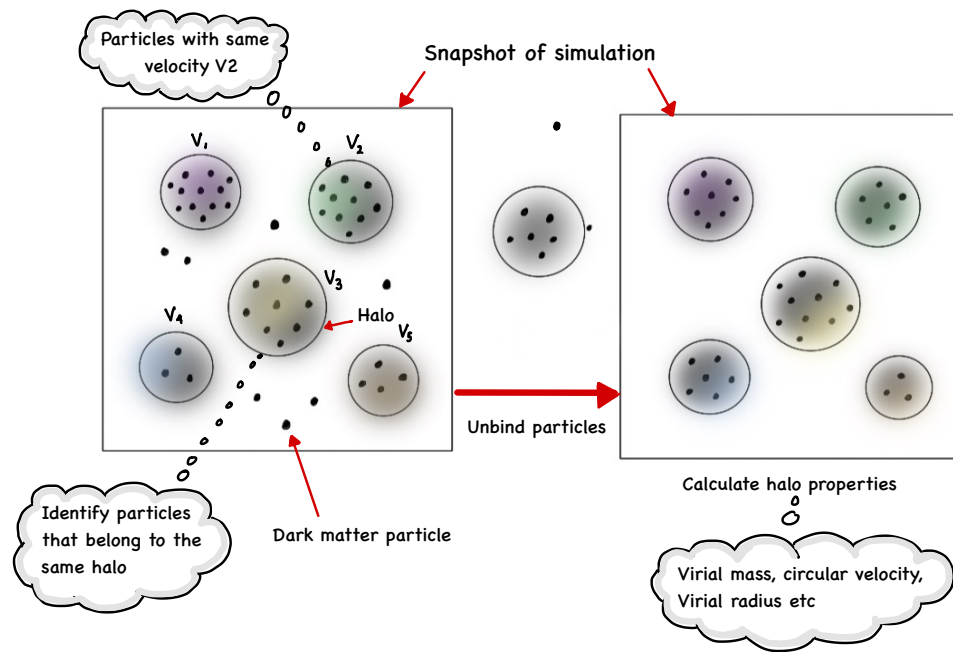


Figure 2.2: Process of halo finding using Friends of friends (FOF) algorithm. Left: Simulation snapshot with dark matter particles: First, particles are grouped together based on their physical proximity and velocities. Here, the distance between particles and their velocities are used to calculate a linking length. If distance between a particle and a halo or two particles is less than this linking length, then they are grouped together. Right: Loosely bound particles are unbound using relative error in potential energy. Once, halo boundaries are identified the algorithm then calculate various properties of dark matter halos such as their mass, velocity, radius, etc.

2.2.2 Spherical Overdensity Algorithms

According to Knollmann & Knebe (2009), spherical overdensity algorithms locate density peaks and identify density contours about them until a certain overdensity threshold is reached (Figure 2.3). The Amiga Halo Finder (AMIGA) by Knollmann & Knebe (2009) uses a spherical overdensity algorithm and analyzes the simulation using Adaptive Mesh Refinement (AMR), identifying halos based on the locations of dense regions. Adaptive mesh refinement is a technique used to selectively refine the current mesh in regions of higher density.

Both halo finders find and determine the properties of halos. However, as shown in Table 2.1, ROCKSTAR is faster than AMIGA (~ 10 min vs. 2 hours per snapshot).

2.2.3 ROCKSTAR vs AMIGA

<i>Halo finder</i>	<i>Algorithm</i>	<i>Time per snapshot</i>
ROCKSTAR	FOF	10 min
AMIGA	Overdensity	2.61 hrs

Table 2.1: This table summarizes information on the halo finders, their type of algorithm, and time required to analyze one snapshot on a Mac mini. Note, each simulation has > 200 snapshots.

ROCKSTAR halo finder identifies smaller mass halos down to $\sim 10^6 M_{\odot}$ while AMIGA has halo masses down to $\sim 10^7 M_{\odot}$ (Figure 2.4). Although, ROCKSTAR is efficient, like many FOF algorithms it may be artificially breaking large halos into smaller components.

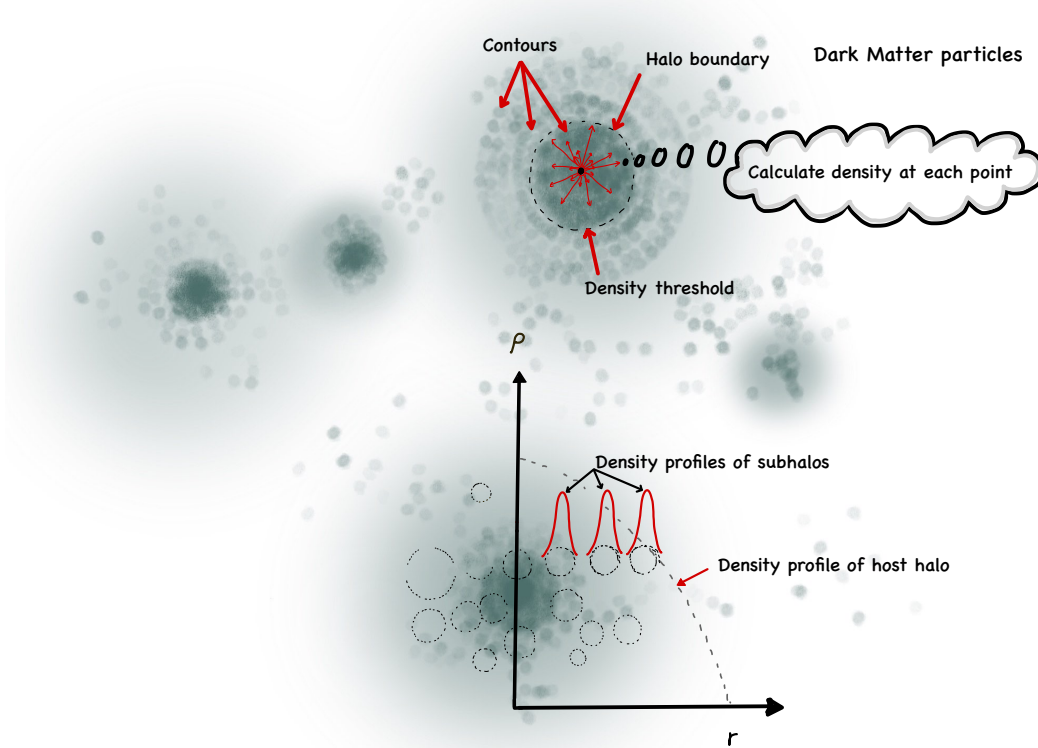


Figure 2.3: This figure shows how a spherical overdensity algorithm work. Top part of the figure shows how a halo boundary is identified. First, it calculates the density of the dark matter particles in the simulation and draws density contours. Once a threshold density is reached, it identifies the region enclosed as a halo. Loosely bound particles are unbound if the velocity of the particles are greater than their escape velocity. The plot below shows the density profile which gives the density of halos as a function of radius. Black dotted lines shows the density profile of the host halo while the red peaks shows density peaks of the sub halos. The algorithm identifies the density peaks of the sub-halos easily if they are located away from the center of the host halo.

Parameters of ROCKSTAR halo finder needs to be explored in order to alleviate this problem. Halo mass function plots the number of galaxies per mass of each galaxy (in solar units) in the simulation as shown in Figure 2.4.

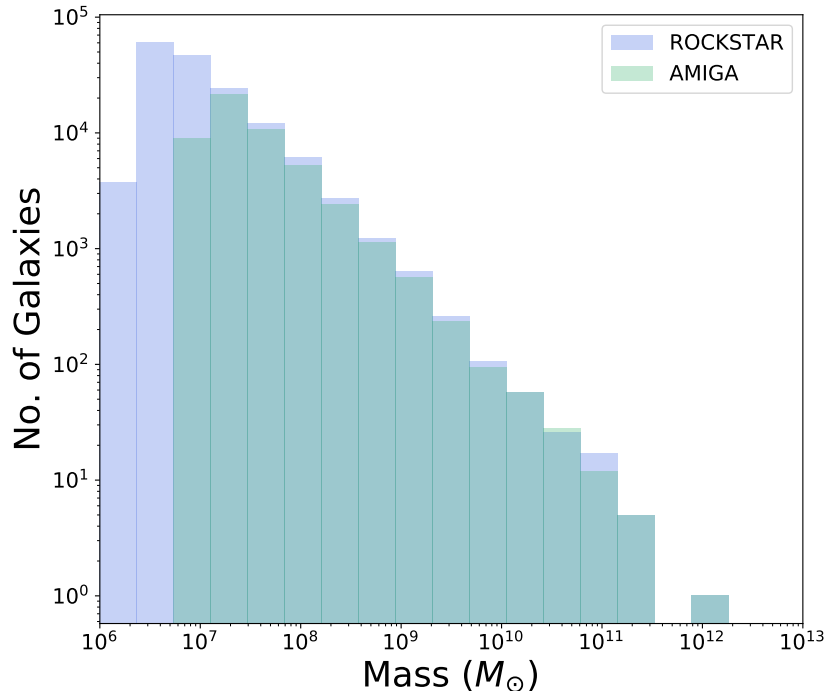


Figure 2.4: Dark matter halo mass function of all the halos in the simulation for AMIGA and ROCKSTAR. AMIGA halo mass function is plotted in green color and ROCKSTAR halo mass function is colored in blue.

2.3 Merger Tree Evolution

Once halo properties are calculated, we determine the evolution of the halos through cosmic time using the merger tree code, `consistent_trees` (Behroozi et al. 2013b). This is done by identifying particles which are members of each halo at $z = 0$ and tracking the particles back in time. At each snapshot the halos which contain particles found in a halo in the previous snapshot are identified and linked to each other. Halos that have the highest number of particles in common with the halo in the previous snapshot are identified as the most massive progenitor. This process is repeated for each snapshot until

all progenitor halos are identified back to formation of the first halos in the simulation. If a halo drops below the resolution limit in one snapshot, then the algorithm approximates halo properties in each time step linking broken links if necessary. If a halo have no descendants ⁴and the statistical significance for that halo's existence is low, a halos is removed.

2.3.1 Consistent Trees

`Consistent_trees` uses the following steps to determine the merger history of halos (Figure 2.5). First, it identifies the descendant halo based on the halo at which the next time step receives the largest fraction of particles for a certain halo. Next, it calculates the gravitational acceleration between two halos, which is gravitationally evolved to calculate the velocities and positions at the previous time step. After identification of the descendants, it removes the links to spurious descendants. Now that the position and velocity of the previous time step are known, it proceeds to link halos with likely progenitors. If a progenitor is missing, then a new halo is created with position and velocity calculated by gravitational evolution. However, if progenitors are missing for several time steps, then such halos are removed. The code also assumes a merger has occurred, exerting a strong tidal field across a halo, if halos at previous time steps have no descendants and are located close to other halos. Otherwise, such halos are removed (Behroozi et al. 2013b).

⁴A descendant halo is a halo that contain the particles from a parent halo in a previous snapshot.

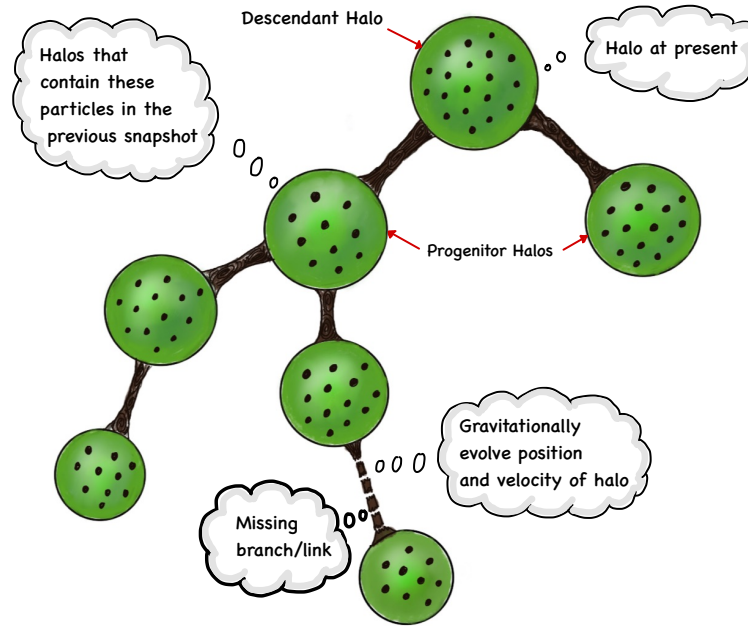


Figure 2.5: This figure shows the process of linking halos in the merger tree code consistent trees (Behroozi et al. 2013b). First, it identifies the dark matter particles in a halo at the present day (descendant halo). Then, it goes back in time to previous snapshot in the simulation to locate the halo which contains the most number of these same particles. Halo that contain these particles is called the progenitor halo. This process is repeated until the algorithm reaches the beginning of the simulation. If certain progenitors cannot be located, then positions and velocity of halos are used to gravitationally evolve their future/past positions and velocities to fix these links. Once every dark matter halo in the simulation is linked to their progenitor, a complete merger history of the simulation can be obtained.

2.4 Modelling Physics of Star Formation

2.4.1 Semi-Analytic Modelling

Semi-analytic modelling is a modelling technique where the baryonic physics is approximated by a set of interconnected differential equations, and the baryonic evolution of galaxies is solved through cosmic time. In the SAM we use , star formation physics is

formulated for a various options for stellar feedback, star formation rate, stellar winds, etc. This physics is applied to a dark matter only simulation. This method is efficient and allows a more effective exploration of parameter space than hydrodynamic simulations. However, it also has some setbacks. Since the computational formulations of physics are approximations, SAMs have trouble with the stochastic processes such as star formation during the epoch of reionization.

2.4.1.1 Galacticus

We use a semi-analytic model Galacticus (Benson 2011). This provides a powerful toolkit to model the physics of how galaxies form. Galacticus takes in merger tree outputs of a simulation and formulates stellar physics. Details of these how Galacticus determines the baryonic physics is in Chapter 4.

Chapter 3

Observational Sample

The number of dwarf satellites of the Local Group has more than doubled over the past 15 years (e.g. Karachentseva & Karachentsev 1998, Karachentseva et al. 1999, Whiting et al. 1997, Zucker et al. 2006, Belokurov et al. 2006, Willman et al. 2005, Walsh et al. 2007, Irwin et al. 2007, Belokurov et al. 2007, Drlica-Wagner et al. 2015; 2016, Torrealba et al. 2018; 2019). Some of the newly discovered dwarf galaxies includes Segue I (Belokurov et al. 2007), Segue II (Belokurov et al. 2009), PiscesII and SegueIII (Belokurov et al. 2010). We use a set of observed data of all nearby dwarf galaxies within 1 Mpc (the dwarf satellites of the Milky Way, M31 galaxies, and the quasi-isolated dwarfs in the outer regions of the Local Group) listed (in the October 2019 version of the [McConnachie 2012](#)). From this sample, we select a subset of satellite galaxies within 400 kpc of Milky Way (Table 3.1). This selected sample consist of 142 dwarf satellites of the Local Group, 62 of which are satellites of the Milky Way. We then use the distribution of various properties of dwarf satellites such as the luminosity function, luminosity metallicity relation, mass to light ratio, velocity dispersion, so forth to constrain our models of dwarf galaxies. See

Table 3.1 for details of the observations.

Radial Distribution: Figure 3.1 shows the radial distribution of dwarf satellite galaxies orbiting within 400 kpc of the Milky Way.

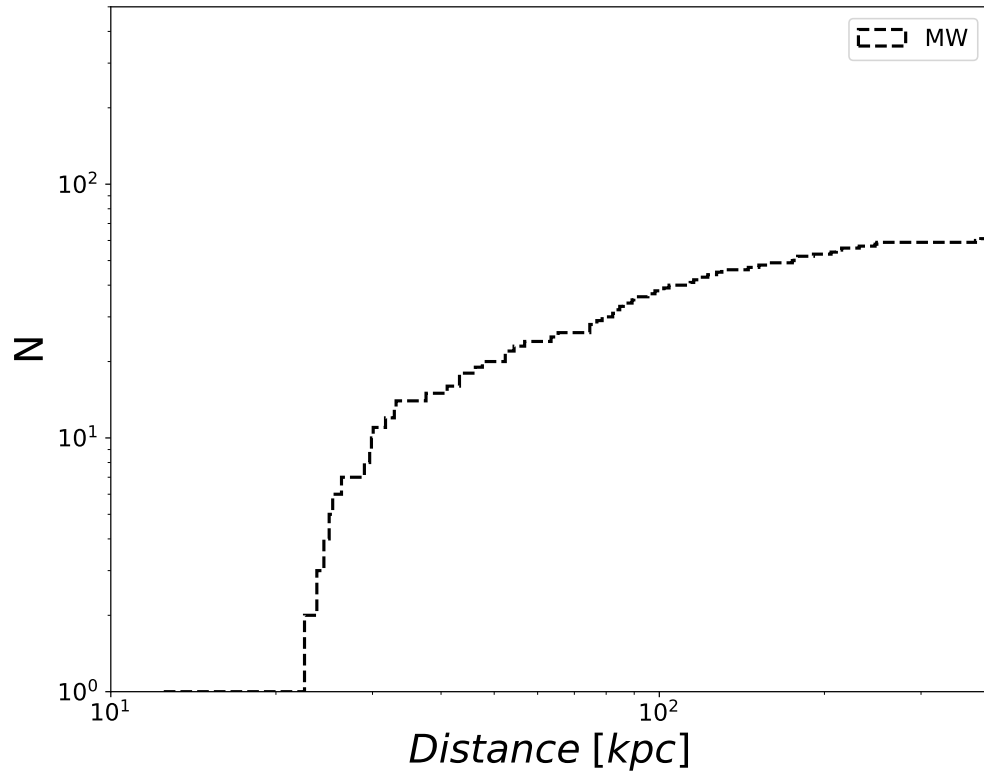


Figure 3.1: Cumulative radial distribution of dwarf satellite galaxies orbiting within 400 kpc of the Milky Way. Y axis shows the number of galaxies (N) as a function of their distance from the galaxy's center in kilo parsec (kpc). The observations are from updated data (October 2019) from McConnachie (2012).

Distribution of Milky Way Dwarf Satellites: Figure 3.2 shows a distribution of satellites within 400 kpc of Milky Way projected onto the sky. Note the zone of inclusion ~ 30 deg north and south of the galactic plane where high foreground densities of stars preclude the detection of dwarf satellites.

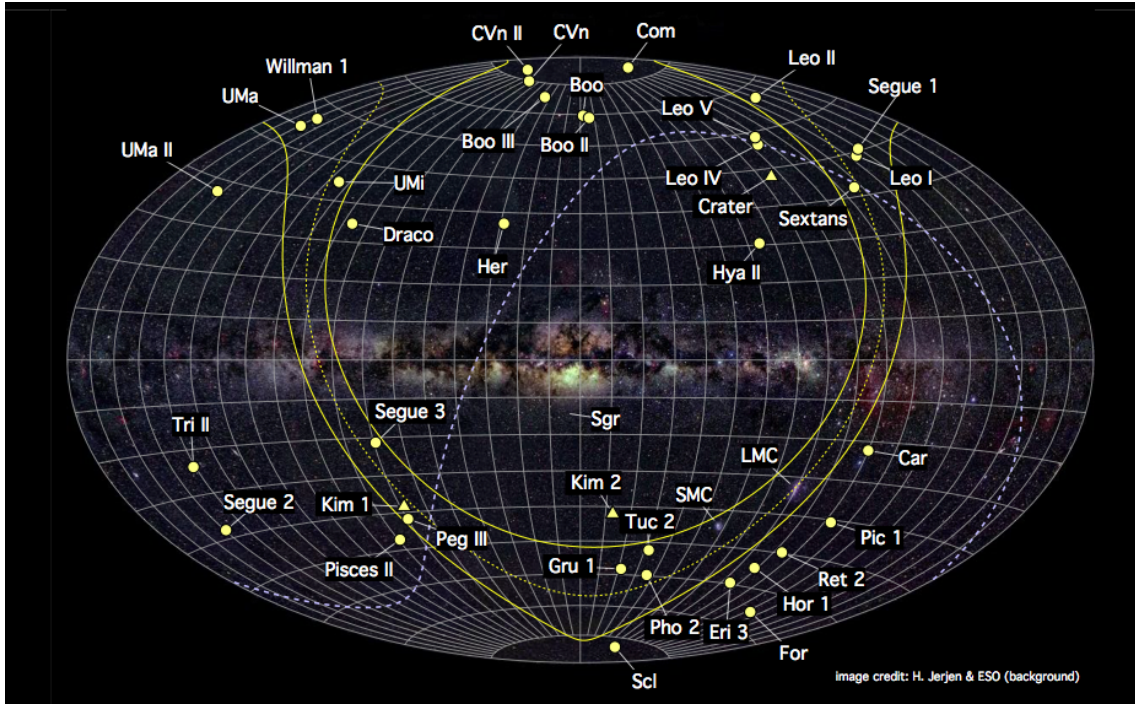


Figure 3.2: Aitoff projection of the observed Milky Way Satellites. This figure marks dwarf satellites hosted by the Milky Way as seen in the sky from Helmut Jerjen. Jerjen, H., 2010, PASA, 29, 383.

<i>Galaxy</i>	<i>R.A.</i>	<i>Decl.</i>	<i>E(B-V)</i>	$(m-M)_0$	v_0 (km/s)	<i>V</i>	<i>PA</i>	<i>e</i>	μ_{V0}	r_h (arcmin)	σ_* (km/s)	v_*^* (km/s)	$M_{HI}(10^6 M_\odot)$	σ_{HI} (km/s)	v_{rot}^{HI} (km/s)	$[Fe/H]$
CanisMajor	7 ^h 12 ^m 35.0 ^s	-27 ^o 40 ^m 0.0 ^s	0.264	14.29	87.0	-0.1	123.0	0.99.0	24.0	999.0	20.0	999.0	999.0	999.0	999.0	-0.5
SagittariusdSph	18 ^h 55 ^m 19.5 ^s	-30 ^o 32 ^m 43.0 ^s	0.153	17.1	140.0	3.6	102.0	0.64	25.2	342.0	11.4	0.0	0.0	0.0	0.0	-0.4
Hydra1	8 ^h 55 ^m 36.0 ^s	3 ^o 36 ^m 0.0 ^s	0.039	15.52	89.4	13.02	999.0	0.99.0	999.0	999.0	8.4	6.0	999.0	999.0	999.0	-0.91
Tucana3	23 ^h 56 ^m 36.0 ^s	-59 ^o 36 ^m 0.0 ^s	0.012	17.01	-102.3	14.6	999.0	0.99.0	28.25	6.0	0.1	999.0	999.0	999.0	999.0	-2.42
Hydrus1	2 ^h 29 ^m 33.4 ^s	-79 ^o 18 ^m 32.0 ^s	0.091	17.2	80.4	12.49	97.0	0.21	26.35	7.42	2.69	999.0	999.0	999.0	999.0	-2.52
Draco2	15 ^h 52 ^m 47.6 ^s	64 ^o 33 ^m 55.0 ^s	0.018	16.9	999.0	14.0	70.0	0.24	25.62	2.7	999.0	999.0	999.0	999.0	999.0	-2.2
Segue(1)	10 ^h 7 ^m 4.0 ^s	16 ^o 4 ^m 55.0 ^s	0.031	16.8	208.5	15.5	75.0	0.34	28.06	3.95	3.9	0.0	0.0	0.0	0.0	-2.72
Carina3	7 ^h 38 ^m 31.2 ^s	-57 ^o 53 ^m 59.0 ^s	0.196	17.22	284.6	14.82	150.0	0.55	26.58	3.75	5.6	999.0	999.0	999.0	999.0	-1.8
Reticulum2	3 ^h 35 ^m 42.1 ^s	-54 ^o 2 ^m 57.0 ^s	0.018	17.4	64.7	13.52	69.0	0.56	26.77	5.59	3.22	999.0	999.0	999.0	999.0	-2.46
Cetus2	1 ^h 17 ^m 52.8 ^s	-17 ^o 25 ^m 12.0 ^s	0.02	17.38	999.0	17.4	999.0	0.99.0	28.55	1.9	999.0	999.0	999.0	999.0	999.0	-2.0
Triangulum2	2 ^h 13 ^m 17.4 ^s	36 ^o 10 ^m 42.0 ^s	0.079	17.4	999.0	15.6	56.0	0.21	28.06	3.9	999.0	999.0	999.0	999.0	999.0	-2.2
Carina2	7 ^h 36 ^m 25.6 ^s	-57 ^o 59 ^m 57.0 ^s	0.188	17.79	477.2	13.29	170.0	0.34	27.29	8.69	3.4	0.0	999.0	999.0	999.0	-2.44
UrsaMajor2	8 ^h 51 ^m 30.0 ^s	63 ^o 7 ^m 48.0 ^s	0.094	17.5	-116.5	13.25	-77.0	0.56	28.07	13.95	6.7	0.0	0.0	0.0	0.0	-2.47
Bootes2	13 ^h 58 ^m 0.0 ^s	12 ^o 51 ^m 0.0 ^s	0.031	18.1	-117.0	15.16	-70.0	0.24	27.55	3.05	10.5	999.0	0.0	0.0	0.0	-1.79
Segue2	2 ^h 19 ^m 16.0 ^s	20 ^o 10 ^m 31.0 ^s	0.185	17.7	-39.2	15.84	166.0	0.21	28.48	3.64	3.4	999.0	999.0	999.0	999.0	-2.22

Table 3.1: Sample of updated observations (October 2019) from McConnachie (2012). Summary of observed quantities for dwarf satellite galaxies orbiting within 400 kpc of Milky Way. Column 1: Galaxy name, Column 2: Right Ascension, Column 3: Declination, Column 4: Foreground reddening, Column 5: E(B-V), measured directly from the Schlegel et al 1998 maps (they do not include the recalibration by Schlafly & Finkbeiner 2011), Column 6: Distance Modulus, $(m-M)_0$, Column 7: Heliocentric radial velocity, Column 8: Apparent V magnitude in Vega mags, Column 9: Position Angle of major axis in degrees measured east from north, Column 9: Projected ellipticity, Column 10: Central V surface brightness, Column 11: Half-light radius measured on major axis, Column 12: Stellar radial velocity dispersion, Column 13: Stellar peak/max rotation velocity, Column 14: Mass of HI (calculated for the adopted distance modulus), Column 15: HI radial velocity dispersion, Column 16: HI peak/max rotation velocity, Column 17: Stellar mean metallicity in dex.

<i>Galaxy</i>	<i>R.A.</i>	<i>Decl.</i>	<i>E(B-V)</i>	$(m - M)_0$	v_0 (km/s)	<i>V</i>	<i>PA</i>	<i>e</i>	μ_{V0}	r_h (arcmin)	σ_* (km/s)	v_c^* (km/s)	$M_{HI}(10^6 M_\odot)$	σ_{HI} (km/s)	v_{rot}^{HI} km/s	[Fe/H]
Willman1'	10 ^h 49 ^m 21.0 ^s	51 ^d 3 ^m 0.0 ^s	0.014	17.9	-12.3	15.37	74.0	0.47	25.87	2.53	4.3	999.0	0.0	0.0	0.0	-2.1
ComaBerenices'	12 ^h 26 ^m 59.0 ^s	23 ^d 54 ^m 15.0 ^s	0.017	18.2	98.1	13.82	-58.0	0.37	26.98	5.63	4.6	0.0	0.0	0.0	0.0	-2.6
Tucana4	0 ^h 2 ^m 55.2 ^s	-60 ^d 51 ^m 0.0 ^s	0.012	18.41	999.0	14.9	11.0	0.4	28.9	9.1	999.0	999.0	999.0	999.0	999.0	-2.3
Bootes3	13 ^h 57 ^m 12.0 ^s	26 ^d 48 ^m 0.0 ^s	0.021	18.35	197.5	12.6	90.0	0.5	31.3	999.0	14.0	999.0	999.0	999.0	999.0	-2.1
Pictor2	6 ^h 44 ^m 43.2 ^s	-59 ^d 53 ^m 49.0 ^s	0.108	18.3	999.0	15.1	14.0	0.13	27.61	3.8	999.0	999.0	999.0	999.0	999.0	-1.8
Grus2	22 ^h 4 ^m 4.8 ^s	-46 ^d 26 ^m 24.0 ^s	0.016	18.62	999.0	14.7	999.0	999.0	28.35	6.0	999.0	999.0	999.0	999.0	999.0	-2.0
Tucana5	23 ^h 37 ^m 24.0 ^s	-63 ^d 16 ^m 12.0 ^s	0.022	18.71	999.0	17.1	30.0	0.7	25.55	1.0	999.0	999.0	999.0	999.0	999.0	-1.8
Tucana2	22 ^h 51 ^m 55.1 ^s	-58 ^d 34 ^m 8.0 ^s	0.019	18.8	-129.1	15.0	107.0	0.39	29.19	9.83	8.6	0.0	999.0	999.0	999.0	-2.23
Sagittarius2	19 ^h 52 ^m 40.5 ^s	-22 ^d 4 ^m 5.0 ^s	0.11	19.13	-177.3	13.9	72.0	0.23	24.88	2.0	2.7	999.0	999.0	999.0	999.0	-2.2
Bootes(1)	14 ^h 0 ^m 6.0 ^s	14 ^d 30 ^m 0.0 ^s	0.017	19.11	99.0	13.09	7.0	0.25	28.38	11.26	2.4	999.0	0.0	0.0	0.0	-2.55
Draco	17 ^h 20 ^m 12.4 ^s	57 ^d 54 ^m 55.0 ^s	0.027	19.4	-291.0	10.69	87.0	0.3	25.12	9.93	9.1	0.0	0.0	0.0	0.0	-1.93
UrsaMinor'	15 ^h 9 ^m 8.5 ^s	67 ^d 13 ^m 21.0 ^s	0.032	19.4	-246.9	10.37	50.0	0.55	25.77	17.32	9.5	0.0	0.0	0.0	0.0	-2.13
Horologium2'	3 ^h 16 ^m 32.1 ^s	-50 ^d 1 ^m 5.0 ^s	0.02	19.46	168.7	17.9	130.0	0.86	27.64	2.83	999.0	999.0	999.0	999.0	999.0	-2.1
Horologium1	2 ^h 55 ^m 31.7 ^s	-54 ^d 7 ^m 8.0 ^s	0.014	19.5	112.8	15.95	50.0	0.31	26.28	1.54	4.9	999.0	999.0	999.0	999.0	-2.76
Phoenix2	23 ^h 39 ^m 59.4 ^s	-54 ^d 24 ^m 22.0 ^s	0.013	19.6	32.4	16.3	-19.0	0.61	25.85	1.61	11.0	999.0	999.0	999.0	999.0	999.0
Sculptor	1 ^h 0 ^m 9.4 ^s	-33 ^d 42 ^m 33.0 ^s	0.018	19.67	111.4	8.85	94.0	0.37	23.29	12.33	9.2	0.0	0.22	0.0	0.0	-1.68

Table 3.1: Sample of updated observations (October 2019) from McConnachie (2012). Summary of observed quantities for dwarf satellite galaxies orbiting within 400 kpc of Milky Way. Column 1: Galaxy name, Column 2: Right Ascension, Column 3: Declination, Column 4: Foreground reddening, Column 5: $E(B-V)$, measured directly from the Schlegel et al 1998 maps (they do not include the recalibration by Schlafly & Finkbeiner 2011), Column 6: Distance Modulus, $(m - M)_0$, Column 7: Heliocentric radial velocity, Column 8: Apparent V magnitude in Vega mags, Column 9: Position Angle of major axis in degrees measured east from north, Column 9: Projected ellipticity, Column 10: Central V surface brightness, Column 11: Half-light radius measured on major axis, Column 12: Stellar radial velocity dispersion, Column 13: Stellar peak/max rotation velocity, Column 14: Mass of HI (calculated for the adopted distance modulus), Column 15: HI radial velocity dispersion, Column 16: HI peak/max rotation velocity, Column 17: Stellar mean metallicity in dex.

<i>Galaxy</i>	<i>R.A.</i>	<i>Decl.</i>	<i>E(B-V)</i>	$(m - M)_0$	v_0 (km/s)	<i>V</i>	<i>PA</i>	<i>e</i>	μ_{V0}	r_h (arcmin)	σ_* (km/s)	v_*^* (km/s)	$M_{HI}(10^6 M_\odot)$	σ_{HI} (km/s)	v_{rot}^{HI} (km/s)	[Fe/H]
Eridanus3'	2 ^h 22 ^m 45.5 ^s	-52 ^d 17 ^m 1.0 ^s	0.025	19.7	999.0	17.33	62.0	0.32	22.84	0.29	999.0	999.0	999.0	999.0	999.0	999.0
Sextans(1)	10 ^h 13 ^m 3.0 ^s	-1 ^d 36 ^m 53.0 ^s	0.047	19.67	224.2	10.4	56.0	0.35	27.1	27.8	7.9	0.0	0.0	0.0	0.0	-1.33
Virgo1	12 ^h 0 ^m 9.1 ^s	0 ^d 40 ^m 51.6 ^s	0.024	19.8	999.0	19.47	62.0	0.59	29.49	1.76	999.0	999.0	999.0	999.0	999.0	999.0
Reticulum3	3 ^h 45 ^m 26.4 ^s	-60 ^d 27 ^m 0.0 ^s	0.048	19.81	274.2	16.5	99.0	0.99	28.16	2.4	999.0	999.0	999.0	999.0	999.0	999.0
Indus1'	21 ^h 8 ^m 49.1 ^s	-51 ^d 9 ^m 56.0 ^s	0.031	20.0	999.0	16.68	5.0	0.72	24.38	0.87	999.0	999.0	999.0	999.0	999.0	999.0
UrsaMajor(1)'	10 ^h 34 ^m 52.8 ^s	51 ^d 55 ^m 12.0 ^s	0.02	19.93	-55.3	14.81	67.0	0.57	29.11	8.34	7.6	999.0	0.0	0.0	0.0	-2.18
Aquarius2	22 ^h 33 ^m 55.5 ^s	-9 ^d 19 ^m 39.0 ^s	0.067	20.16	-71.1	15.8	121.0	0.39	28.56	5.1	5.4	999.0	999.0	999.0	999.0	-2.3
Carina'	6 ^h 41 ^m 36.7 ^s	-50 ^d 57 ^m 58.0 ^s	0.061	20.11	222.9	10.68	60.0	0.37	25.35	11.43	6.6	0.0	0.0	0.0	0.0	-1.72
Grus1	22 ^h 56 ^m 42.4 ^s	-50 ^d 9 ^m 48.0 ^s	0.008	20.4	-140.5	16.93	11.0	0.54	26.86	2.08	9.8	999.0	999.0	999.0	999.0	-1.42
Crater2	11 ^h 49 ^m 14.4 ^s	-18 ^d 24 ^m 47.0 ^s	0.03	20.35	87.5	12.15	0.0	0.0	29.38	31.2	2.7	0.6	999.0	999.0	999.0	-1.98
Pictoris1	4 ^h 43 ^m 47.4 ^s	-50 ^d 16 ^m 59.0 ^s	0.013	20.3	999.0	16.85	72.0	0.24	24.5	0.66	999.0	999.0	999.0	999.0	999.0	999.0
Hercules	16 ^h 31 ^m 2.0 ^s	12 ^d 47 ^m 30.0 ^s	0.062	20.6	45.2	14.77	-73.0	0.69	26.82	5.99	3.7	999.0	0.0	0.0	0.0	-2.41
Hydra2	12 ^h 21 ^m 42.1 ^s	-31 ^d 59 ^m 7.0 ^s	0.061	20.64	303.1	16.04	29.0	0.17	26.14	1.5	999.0	999.0	999.0	999.0	999.0	-2.02
Antlia2	9 ^h 35 ^m 32.8 ^s	-36 ^d 46 ^m 2.0 ^s	0.15	20.6	290.7	11.57	156.0	0.38	30.22	76.2	5.71	999.0	999.0	999.0	999.0	-1.36
Fornax	2 ^h 39 ^m 59.3 ^s	-34 ^d 26 ^m 57.0 ^s	0.021	20.84	55.3	7.38	46.0	0.28	23.59	18.4	11.7	0.0	0.17	0.0	0.0	-0.99

Table 3.1: Sample of updated observations (October 2019) from McConnachie (2012). Summary of observed quantities for dwarf satellite galaxies orbiting within 400 kpc of Milky Way. Column 1: Galaxy name, Column 2: Right Ascension, Column 3: Declination, Column 4: Foreground reddening, Column 5: E(B-V), measured directly from the Schlegel et al 1998 maps (they do not include the recalibration by Schlafly & Finkbeiner 2011), Column 6: Distance Modulus, $(m - M)_0$, Column 7: Heliocentric radial velocity, Column 8: Apparent V magnitude in Vega mags, Column 9: Position Angle of major axis in degrees measured east from north, Column 9: Projected ellipticity, Column 10: Central V surface brightness, Column 11: Half-light radius measured on major axis, Column 12: Stellar radial velocity dispersion, Column 13: Stellar peak/max rotation velocity, Column 14: Mass of HI (calculated for the adopted distance modulus), Column 15: HI radial velocity dispersion, Column 16: HI peak/max rotation velocity, Column 17: Stellar mean metallicity in dex.

<i>Galaxy</i>	<i>R.A.</i>	<i>Decl.</i>	<i>E(B-V)</i>	$(m - M)_0$	v_0 (km/s)	<i>V</i>	<i>PA</i>	<i>e</i>	μ_{V0}	r_h (arcmin)	σ_* (km/s)	v_r^* (km/s)	$M_{HI}(10^6 M_\odot)$	σ_{HI} (km/s)	v_{rot}^{HI} (km/s)	[Fe/H]
Leo4	11 ^h 32 ^m 57.0 ^s	0 ^h 32 ^m 0.0 ^s	0.026	20.94	132.3	15.95	-29.0	0.19	27.8	2.61	3.3	999.0	0.0	0.0	0.0	-2.54
CanesVenatici2	12 ^h 57 ^m 10.0 ^s	34 ^d 19 ^m 15.0 ^s	0.01	21.02	-128.9	15.85	10.0	0.46	26.5	1.51	4.6	999.0	0.0	0.0	0.0	-2.21
Leo5	11 ^h 31 ^m 9.6 ^s	2 ^d 13 ^m 12.0 ^s	0.027	21.25	173.3	16.85	-65.0	0.35	24.89	1.0	3.7	999.0	0.0	0.0	0.0	-2.0
Pisces2	22 ^h 58 ^m 31.0 ^s	5 ^d 57 ^m 9.0 ^s	0.065	21.3	-226.5	17.08	99.0	0.4	26.52	1.22	5.4	999.0	999.0	999.0	999.0	-2.45
Columba1	5 ^h 31 ^m 26.4 ^s	-28 ^d 1 ^m 48.0 ^s	0.025	21.3	153.7	16.8	999.0	999.0	27.95	1.9	999.0	999.0	999.0	999.0	999.0	999.0
Pegasus3	22 ^h 24 ^m 22.6 ^s	5 ^d 25 ^m 12.0 ^s	0.147	21.56	-222.9	17.5	133.0	0.46	27.16	1.3	5.4	999.0	999.0	999.0	999.0	-2.1
Indus2	20 ^h 38 ^m 52.8 ^s	-46 ^d 9 ^m 36.0 ^s	0.034	21.65	999.0	17.4	999.0	999.0	29.47	2.9	999.0	999.0	999.0	999.0	999.0	999.0
Bootes4	15 ^h 34 ^m 45.4 ^s	43 ^d 43 ^m 34.0 ^s	0.025	21.6	999.0	17.07	3.0	0.64	30.12	7.6	999.0	999.0	999.0	999.0	999.0	999.0
CanesVenatici(1)	13 ^h 28 ^m 3.5 ^s	33 ^d 33 ^m 21.0 ^s	0.014	21.69	30.9	13.1	70.0	0.39	27.1	8.9	7.6	999.0	0.0	0.0	0.0	-1.98
Leo2	11 ^h 13 ^m 28.8 ^s	22 ^d 9 ^m 6.0 ^s	0.017	21.84	78.0	12.1	43.0	0.07	24.24	2.48	6.6	999.0	0.0	0.0	0.0	-1.62
Cetus3	2 ^h 5 ^m 19.4 ^s	-4 ^d 16 ^m 12.0 ^s	0.024	22.0	999.0	19.55	101.0	0.76	28.21	1.23	999.0	999.0	999.0	999.0	999.0	999.0
Leo1	10 ^h 8 ^m 28.1 ^s	12 ^d 18 ^m 23.0 ^s	0.036	22.02	282.5	10.24	78.0	0.3	22.61	3.3	9.2	0.0	0.0	0.0	0.0	-1.43
IC10	0 ^h 20 ^m 17.3 ^s	59 ^d 18 ^m 14.0 ^s	1.568	24.5	-348.0	9.5	999.0	0.19	24.6	2.65	999.0	999.0	50.0	8.0	34.0	-1.28
Eridanus2	3 ^h 44 ^m 21.1 ^s	-43 ^d 32 ^m 0.0 ^s	0.01	22.9	75.6	15.69	82.0	0.37	26.63	1.81	6.9	0.0	999.0	999.0	999.0	-2.38
SMC	0 ^h 52 ^m 44.8 ^s	-72 ^d 49 ^m 43.0 ^s	0.419	19.03	145.6	2.2	999.0	999.0	999.0	999.0	27.6	0.0	460.0	22.0	60.0	-1.0
LMC	5 ^h 23 ^m 34.5 ^s	-69 ^d 45 ^m 22.0 ^s	0.927	18.52	262.2	0.4	999.0	999.0	999.0	999.0	20.2	49.8	460.0	15.8	63.0	-0.5

Table 3.1: Sample of updated observations (October 2019) from McConnachie (2012). Summary of observed quantities for dwarf satellite galaxies orbiting within 400 kpc of Milky Way. Column 1: Galaxy name, Column 2: Right Ascension, Column 3: Declination, Column 4: Foreground reddening, Column 5: $E(B-V)$, measured directly from the Schlegel et al 1998 maps (they do not include the recalibration by Schlafly & Finkbeiner 2011), Column 6: Distance Modulus, $(m - M)_0$, Column 7: Heliocentric radial velocity, Column 8: Apparent V magnitude in Vega mags, Column 9: Position Angle of major axis in degrees measured east from north, Column 9: Projected ellipticity, Column 10: Central V surface brightness, Column 11: Half-light radius measured on major axis, Column 12: Stellar radial velocity dispersion, Column 13: Stellar peak/max rotation velocity, Column 14: Mass of HI (calculated for the adopted distance modulus), Column 15: HI radial velocity dispersion, Column 16: HI peak/max rotation velocity, Column 17: Stellar mean metallicity in dex.

Luminosity Function: The luminosity function is the cumulative distribution of luminosities for a sample of galaxies. We plot the luminosity function of the dwarf satellites orbiting within 400 kpc of the Milky Way in Figure 3.3. As expected, there are more halos with low luminosity and few with higher luminosities. We use the luminosity function as the primary constraint to our model. The dashed line in Figure ?? shows the luminosity function of the Milky Way satellites when we exclude the Small Magellanic Cloud (SMC) and the Large Magellanic Cloud (LMC). This is done because the presence of an SMC/LMC around a Milky Way mass halo is rare (Liu et al. 2011, Busha et al. 2011, Tollerud et al. 2011).

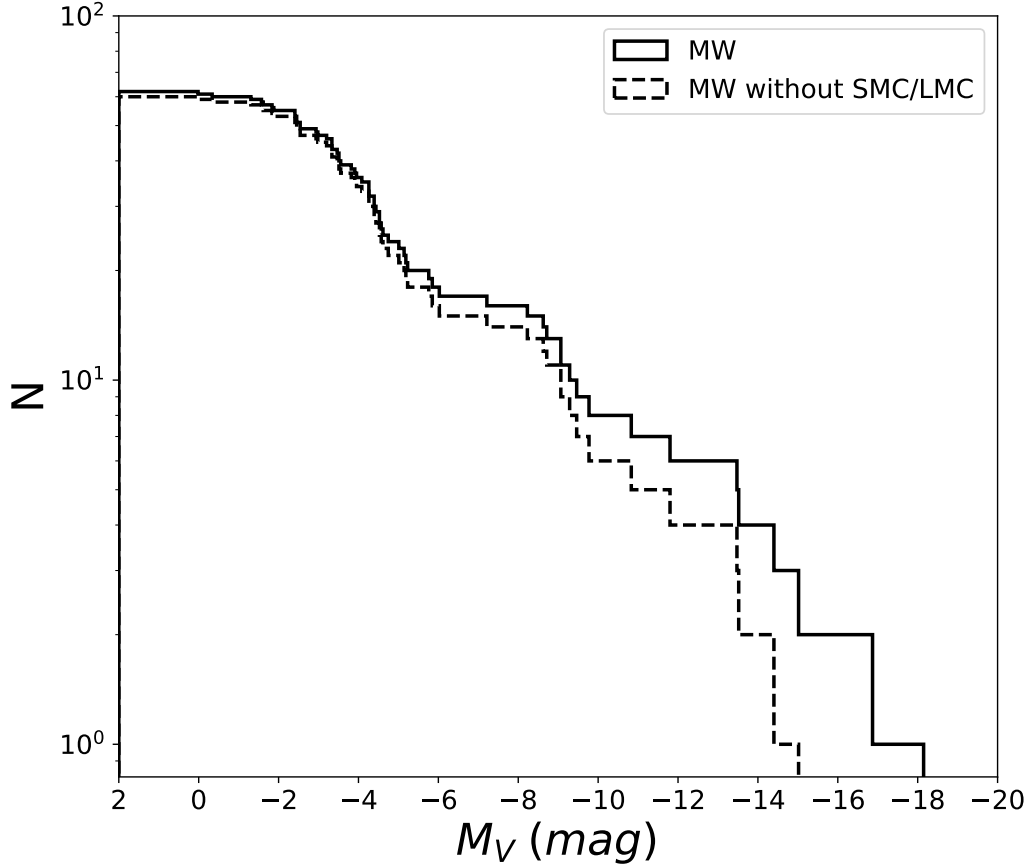


Figure 3.3: Cumulative luminosity function for the Milky Way satellite dwarf galaxies orbiting within 400 kpc as a function of absolute V band magnitude (M_V). The black line shows the luminosity function that includes the Magellanic Clouds. Magellanic clouds are excluded since The dashed black line shows the luminosity function that do not include the Magellanic Clouds. N denotes the number of satellites galaxies per brightness bin. The observations are retrieved from updated data (October 2019) from McConnachie (2012)

Luminosity Metallicity Relation: The luminosity metallicity relation is an excellent constraint for our model since it forms a smooth function across luminous spiral galaxies to less luminous dwarf galaxies. Metallicity gives the proportion of elements heavier than Helium in stars of the satellite dwarf galaxies. Metallicity for observations is defined by

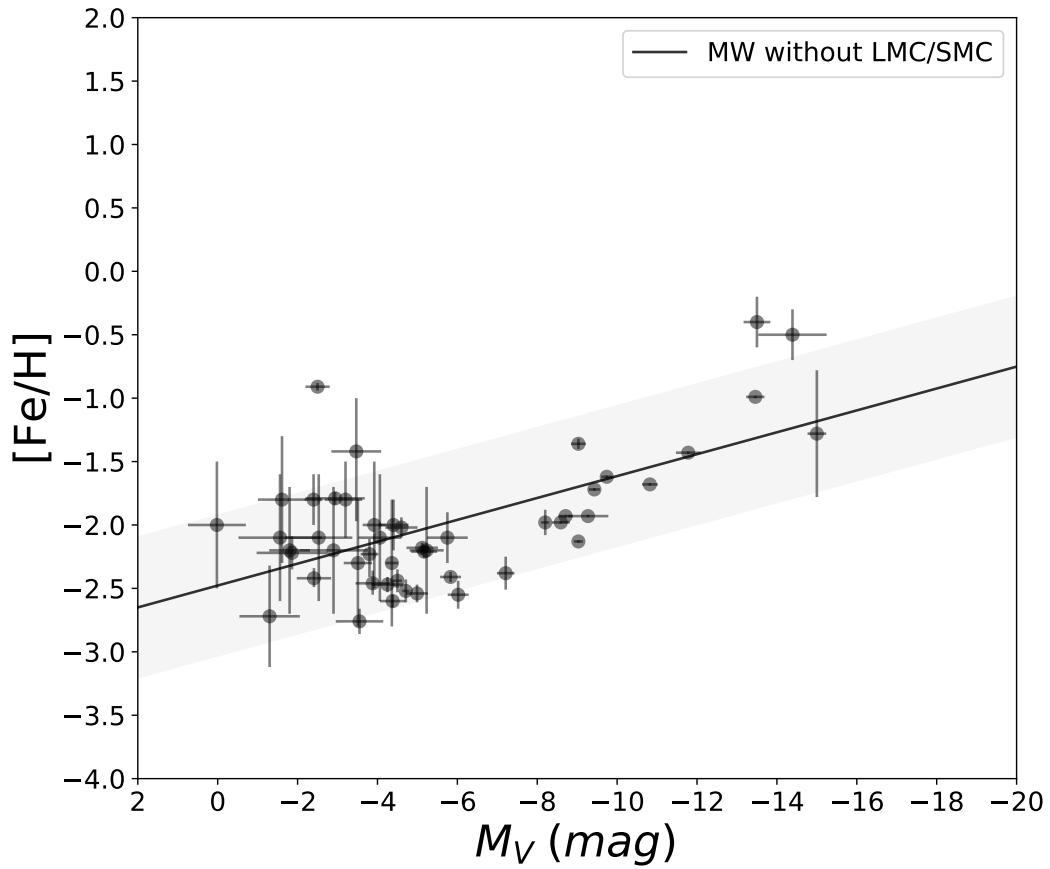


Figure 3.4: Luminosity metallicity relation for the Milky Way satellite dwarf galaxies orbiting within 400 kpc as a function of absolute V band magnitude (M_V). The data points do not include the Magellanic Clouds. The observations are retrieved from updated data (October 2019) from McConnachie (2012).

$[Fe/H] = \log_{10} \left(\frac{N_{Fe}}{N_H} \right)_* - \log_{10} \left(\frac{N_{Fe}}{N_H} \right)_\odot$ (Figure 3.4). Unlike luminosity which depends on stellar mass of the galaxies at the present day, metallicity leaves an imprint of the peak mass of galaxies even if tidal and ram pressure strips stars and gas. This is because the metallicity of a galaxy is determined by the depth of the potential well and M_{Peak} ¹ and the galaxies subsequent ability to hold onto enriched ejecta from supernova. Tidal stripping is the stripping of matter from satellite galaxies due to the tidal field of the host galaxy, while ram pressure stripping is the loss of mass due to ram pressure created as satellite galaxies fall into the halo of the host.

Mass to Light Ratio: The total mass relative to the total light within a given radius specifies the strength of the dark matter component to the mass of a particular galaxy. It can be used to convert observed light distributions in galaxies into estimates of mass distributions, thereby providing information for dynamical analysis. Mass to light ratios of the Milky Way satellites fall in the range $10 \leq M/L \leq 1000 M_\odot/L_\odot$. Figure 3.5 gives the mass to light ratio of satellite dwarf galaxies orbiting the Milky Way. Mass to light ratio within the half light radius $M_{1/2}/L_{1/2}$, is calculated with $M_{1/2} = 3G^{-1} \langle \sigma_{los}^2 \rangle r_{1/2}$ (Wolf et al. 2010).

¹ M_{peak} is the maximum mass a halo gas during its evolution.

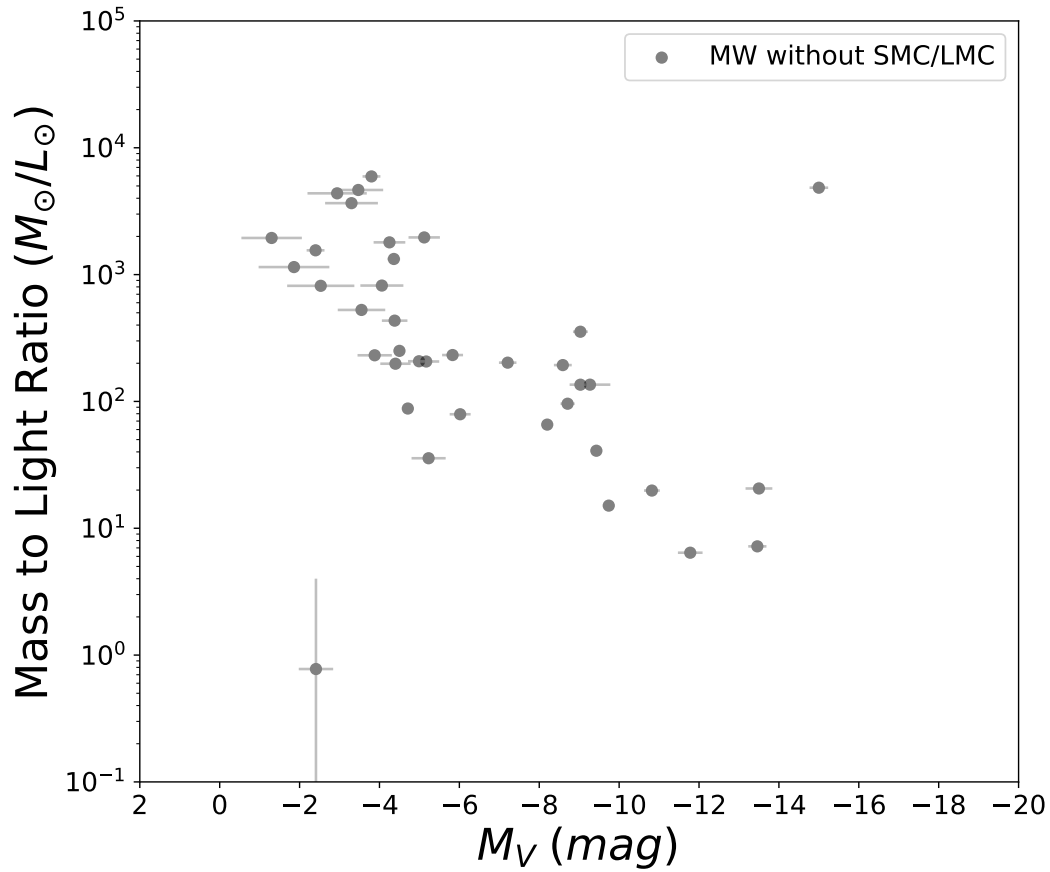


Figure 3.5: Mass to light ratio of satellite dwarf galaxies orbiting Milky Way within 400 kpc (in solar units) as a function of absolute V band magnitude. The observations are from updated data (October 2019) from McConnachie (2012).

Velocity Dispersion: The stellar velocity dispersion (σ_*) of a galaxy measures the random line-of-sight motion of stars due to the gravitational potential of the total mass enclosed in within the radius of the stars. It is used to measure the mass of a galaxy, probing the depth of galactic gravitational potential wells where stars are captured, and hence is a good indication for how dark matter dominated a galaxy is. In Figure 3.6, We plot the velocity dispersion as a function of absolute V band magnitude.

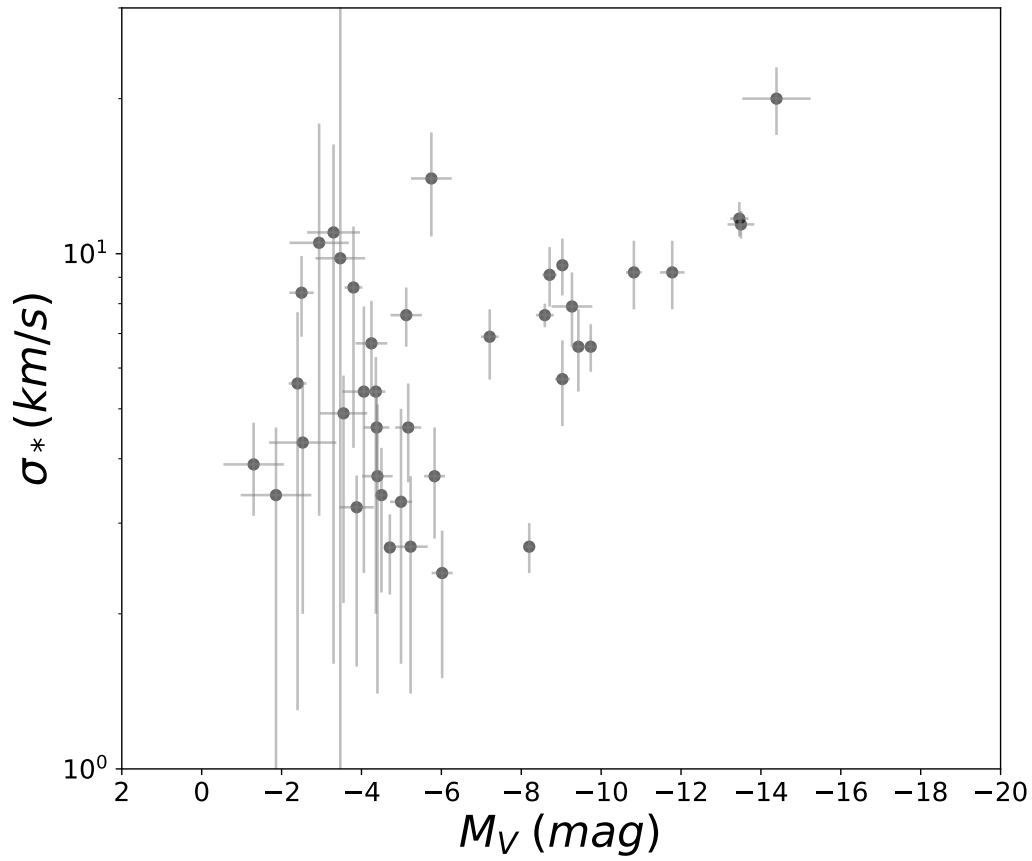


Figure 3.6: Velocity dispersion σ_* of satellite dwarf galaxies orbiting Milky Way within 400 kpc as a function of absolute V band magnitude. The observations are retrieved from updated data (October 2019) from McConnachie (2012).

Chapter 4

Results

We present the best fit parameters of the SAM Galacticus for dwarf galaxies constrained using observations of the Milky Way dwarf satellites.

4.1 Dependence on the Halo Finder

Galacticus is run on the outputs of both the ROCKSTAR and AMIGA halo finders produces similar trends in parameter space with the exception of tidal stripping. However, the luminosity functions produced from AMIGA outputs better matches with observations, (Figure 4.1). Although halos of both algorithms produce luminosities extending over the observed luminosities, ROCKSTAR results do not produce sufficient halos with absolute V band magnitude (M_V) between -8 and -13 magnitudes. This may be due to ROCKSTAR artificially splitting high mass halos into smaller halos in its 6D FOF algorithm, whereas AMIGA identifies halos based on density peaks and does not have this issue. However, as ROCKSTAR uses a fraction of the resources of AMIGA, ROCKSTAR

parameters need to be explored to produce results similar to those of AMIGA. In the remainder of this work, we will show Galacticus run on merger trees generated AMIGA being the halo finder for the best fit parameters of the of Milky Way dwarfs.

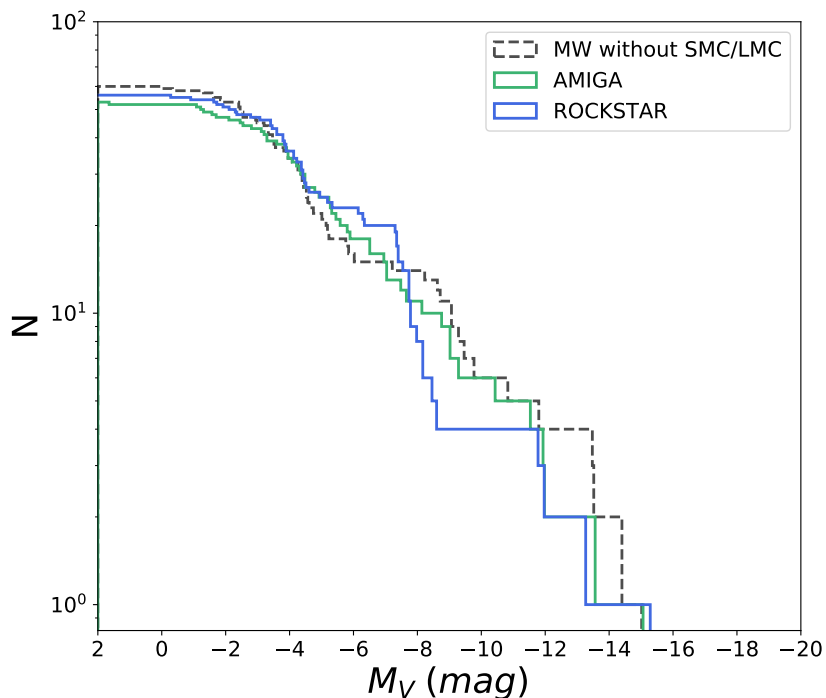


Figure 4.1: We plot the cumulative luminosity function for the Milky Way satellite dwarf galaxies orbiting within 400 kpc as a function of absolute V band magnitude (M_V). The dashed black line shows the luminosity function that do not include the Magellanic Clouds. N denotes the number of satellites galaxies per brightness bin. The observations are retrieved from updated data (October 2019) of McConnachie (2012). Green curve shows the galaxy models based on AMIGA halo finder (best fit for observed luminosity function) and the blue curve shows the models based on ROCKSTAR halo finder

4.2 Gas Cooling

4.2.1 Cooling Rate Cutoff Velocity

Cooling of gas inside the hot halo in the simulated dwarf galaxies can be controlled by introducing a parameter called cooling rate cut off velocity ($v_{cooling}$). The cooling-rate cutoff velocity is the maximum velocity of halos below which no gas in the halos will cool. As the cooling cutoff increases, cooling is turned off in halos with higher virial velocities¹ (higher virial masses).

We plot the luminosity function for all of the runs above to explore the simulated Milky Way satellite luminosity function best fitting $v_{cooling}$ with the observed luminosity function within 400 kpc (Figure 4.2). Further exploration of cooling velocities with other parameters reveal that $v_{cooling} = 17 \text{ km/s}$ is the best value for the cooling rate cut off velocity. The best fit model is obtained by comparison of luminosity functions with the observed luminosity function of the Milky Way dwarf galaxies by eye.

¹Virial velocity is the velocity of the halo at virial radius. $v_{vir} = \sqrt{\frac{GM_{vir}}{r_{vir}}}$.

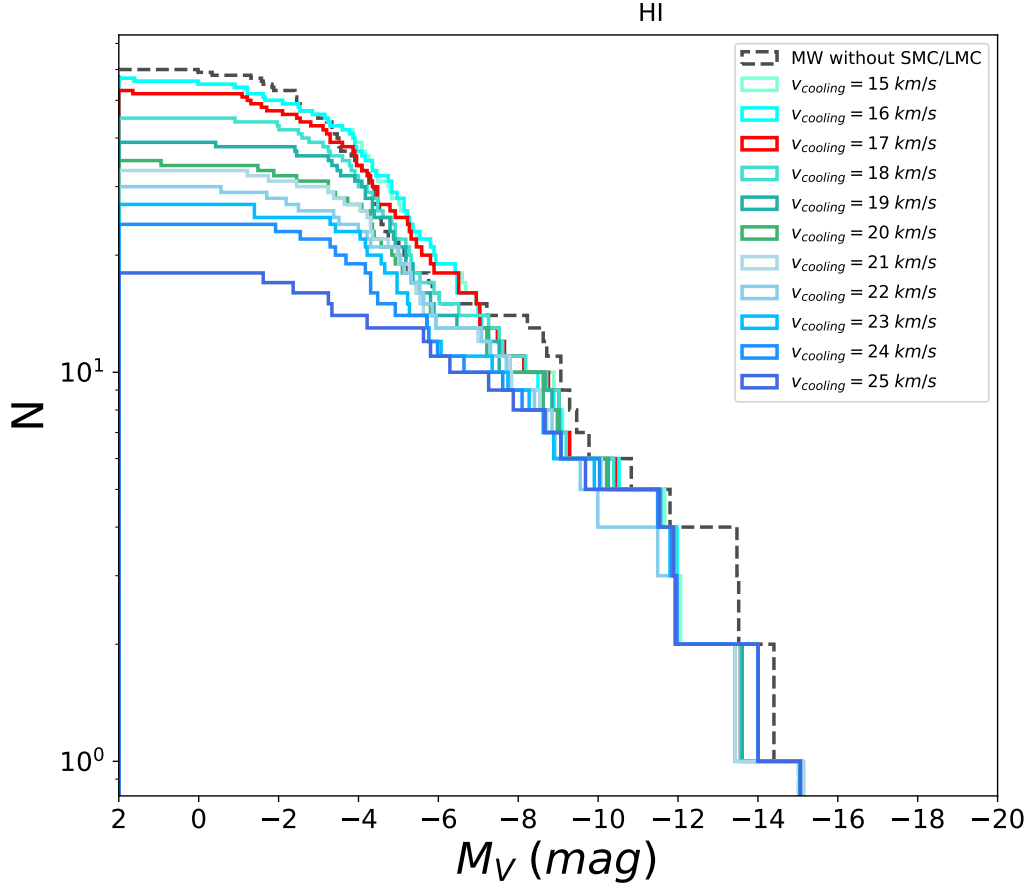


Figure 4.2: Cumulative luminosity function for the Milky Way satellite dwarf galaxies orbiting within 400 kpc as a function of absolute V band magnitude (M_V). The dashed black line shows the luminosity function that do not include the Magellanic Clouds. N denotes the number of satellites galaxies per brightness bin. The observations are retrieved from updated data (October 2019) of McConnachie (2012). Colored curves shows the galaxy models for various cooling rate cut off velocities with red curve showing the best fitting model

4.3 Inflow of Baryons into Halos

The inflow of baryons into halos governs the star formation in galaxies by determining the amount of gas available for star formation. We implement several methods of gas

accretion, and stellar and tidal feedback to simulate the inflow of baryons to our Milky Way satellites.

4.3.1 Mass Accretion:

Mass accretion into halos is determined by several parameters such as reionization suppression redshift ($z_{reionization}$), filtering velocity (v_{filter}), and cooling rate cut off velocity ($v_{cooling}$). It is also regulated by preventive feedback mechanisms. Preventive feedback prevents baryons from accumulating onto halos or their dark matter counterparts (Lu et al. 2017).

The epoch of reionization is the era during which hydrogen atoms were ionized by the light emitted by the first stars (Zaroubi 2013). The universe was dense and opaque before the first stars formed roughly a hundred million years after the big bang. At this time, the IGM was neutral and opaque to many wavelengths. As the first stars emitted light, primarily in the UV, they ionized hydrogen atoms and the IGM became transparent. This is the process of reionization. Accretion of mass into halos was effected by reionization, especially the lowest mass galaxies. In Galacticus this process is parameterized by $z_{reionization}$ and v_{filter}

4.3.1.1 Reionization Suppression Redshift

The region around the local group is believed to have reionized around $z = 9$. We run several models with different reionization suppression redshifts (Figure 4.3). Before introducing stellar feedback effects into the galaxy models, reionization suppression redshift

of $z = 10$ provides the best match with the observed luminosity function. However, upon introducing star formation feedback such as supernovae, a reionization redshift of $z = 9$ is found to be the best fit in agreement with other work. Note that best fit model is primarily constrained by the luminosity function which is the primary constraint.

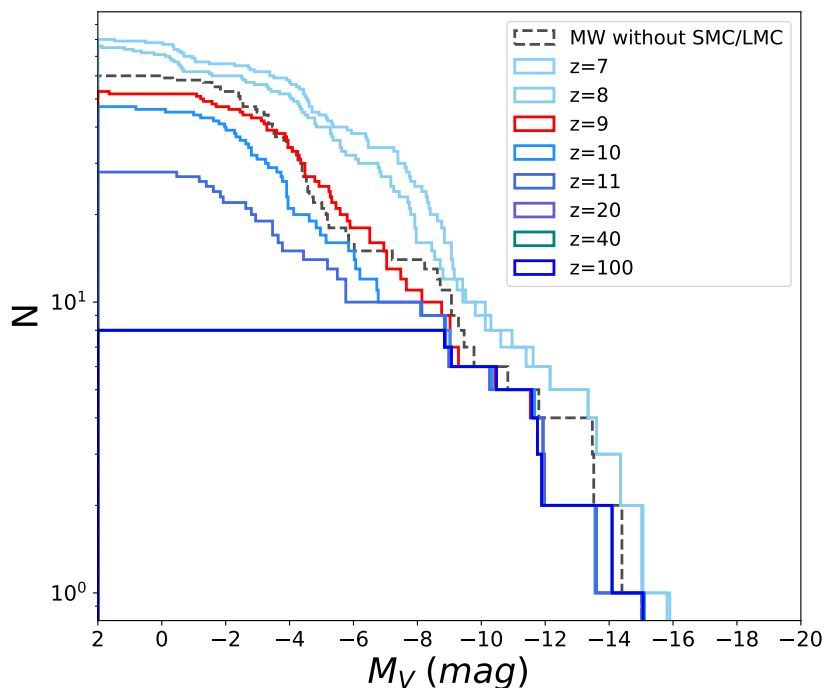


Figure 4.3: Cumulative luminosity function for the Milky Way satellite dwarf galaxies orbiting within 400 kpc as a function of absolute V band magnitude (M_V). The dashed black line shows the luminosity function that do not include the Magellanic Clouds. The observations are from (McConnachie 2012, see table 3.1). N denotes the number of satellites galaxies per brightness bin. Colored curves shows the preliminary galaxy models for different reionization suppression redshifts.

4.3.1.2 Reionization Suppression Velocity

Reionization suppresses the accretion gas into halos from the IGM. When hydrogen atoms are reionized by the first stars and galaxies, the temperature of the IGM increased to

$2 \times 10^4 K$. The reheated IGM sets a minimum halo mass, M_{filter} (Gnedin 2000) below which a halo will be unable to accrete additional material from the IGM. As the maximum circular velocity, v_{max} , of a halo scales with the mass but does not scale with redshift, a filtering velocity v_{filter} is used. The v_{max} of a halo is proportional to its virial mass given by $v_{max} = \sqrt{\frac{GM_{vir}}{R_{vir}}}$. Hence, reionization suppression velocity allows us to set a minimum v_{max} for halos to form stars, analogous to setting a minimum mass to form stars. Although, there are established values in the literature, we test several filtering velocity values from 10, 20, 25, 30, 35, 40, 50 km/s (Figure 4.4). We find 30 km/s to be the best fit value which is also the value suggested in literature (Ricotti & Gnedin 2005, Bovill & Ricotti 2011).

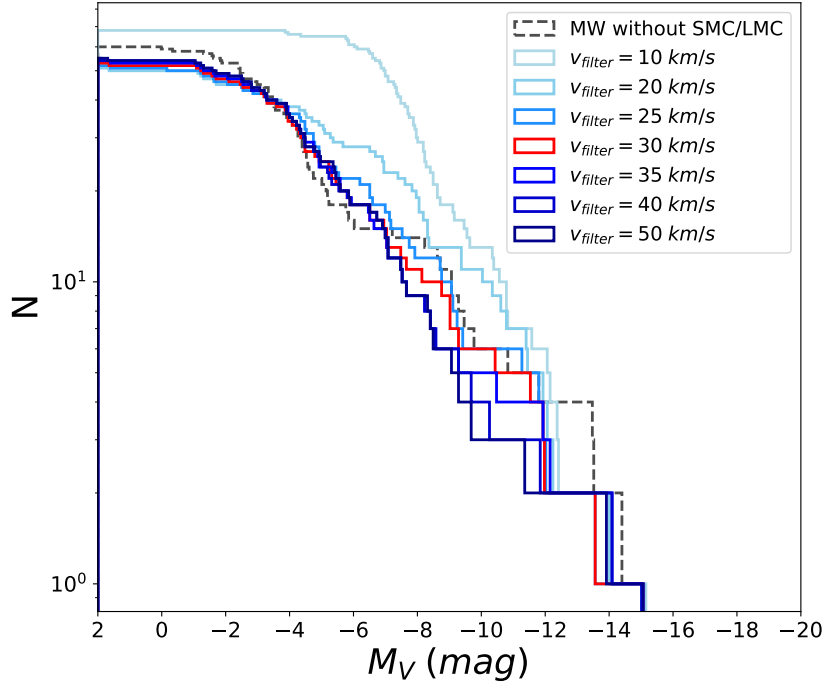


Figure 4.4: We plot the cumulative luminosity function for the Milky Way satellite dwarf galaxies orbiting within 400 kpc as a function of absolute V band magnitude (M_V). The dashed black line shows the luminosity function that do not include the Magellanic Clouds. N denotes the number of satellites galaxies per brightness bin. The observations are retrieved from updated Table 1 (October 2019) of McConnachie (2012). Colored curves shows the galaxy models for various reionization suppression velocities

4.4 Molecular Clouds/Hot Halo Gas Cooling:

While star formation is dependent on factors such as self gravity of the gas cloud and pressure, cooling of gas plays a major role in this process. We use two implementations in Galacticus to formulate gas cooling in halos: cooling due to atomic collisional ionization equilibrium and cooling due to molecular hydrogen.

4.4.1 Cooling Functions:

We incorporate different cooling functions available in Galacticus for our simulated dwarf galaxies. These include cooling due to collisional ionization equilibrium and cooling due to molecular hydrogen. Cooling rates for collisional ionization equilibrium cooling is calculated using the radiative transfer code CLOUDY (Ferland et al. 2017). This method assumes collisional equilibrium without any molecular contribution. *“Abundances are Solar, except for zero metallicity calculations which uses CLOUDY’s “primordial” metallicity”* (Galacticus Documentation). Galacticus formulates $H_2^+ - e^-$, $H - H_2^+$ cooling fitting functions from Suchkov & Shchekinov (1978) and cooling due to molecular hydrogen $H - H_2$ cooling fitting functions from Galli & Palla (1998).

$$\log_{10}\left(\frac{\Lambda(T)}{\text{ergs}^{-1}\text{cm}^3}\right) = C_0 + C_1 \log_{10}\left(\frac{T}{K}\right) + C_2 \left[\log_{10}\left(\frac{T}{K}\right)\right]^2$$

Our default method of gas cooling in Galacticus is cooling due to atomic collisional ionization equilibrium where C_0 , C_1 , C_2 are coefficients of H_2^+ appearing in the fitting function given above. C_0 , C_1 , C_2 values for $H_2^+ - e^-$ are -33.33, 5.565, and 0.4675, while that of $H - H_2^+$ are given by -35.28, 5.862, -0.5124 (Galacticus Documentation). We ran models with cooling due to molecular hydrogen together in addition to collisional ionization equilibrium, however, there minimal effect in the observable properties of the halos resulting models (Figure 4.5 and Figure 4.6). Therefore, we incorporate both cooling functions in our simulated dwarf galaxies.

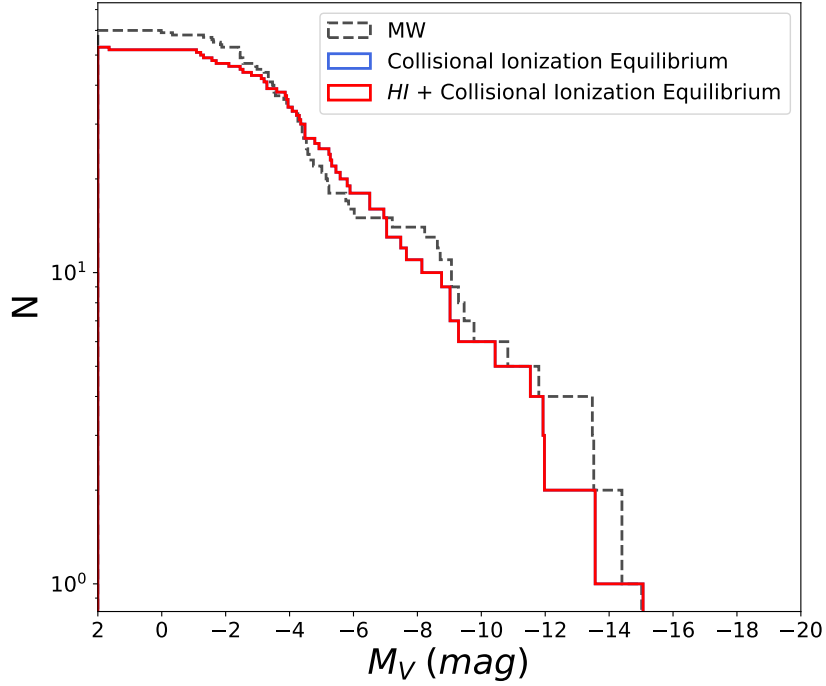


Figure 4.5: Cumulative luminosity function for the Milky Way satellite dwarf galaxies orbiting within 400 kpc as a function of absolute V band magnitude (M_V). The dashed black line shows the luminosity function that do not include the Magellanic Clouds. N denotes the number of satellites galaxies per brightness bin. The observations are retrieved from updated data (October 2019) of McConnachie (2012). Colored curves shows the galaxy models for different cooling functions incorporated. Turquoise curve shows the model with cooling due collisional ionization equilibrium of atomic gas together with molecular hydrogen cooling while the blue curve shows cooling due to atomic collisional ionization equilibrium cooling. Both curves overlap with each other.

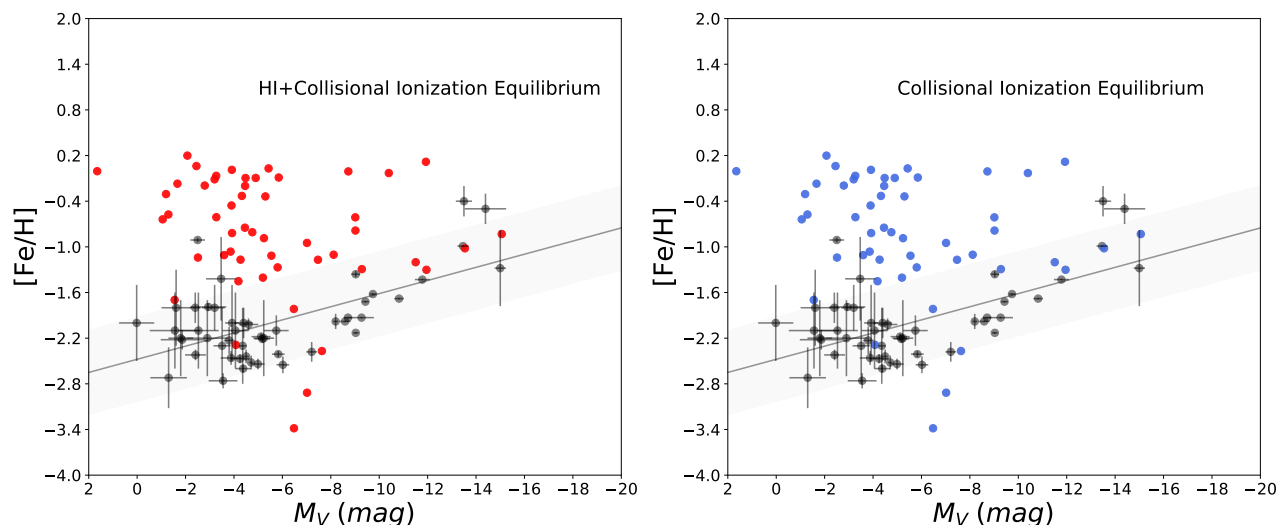


Figure 4.6: This figure shows the luminosity metallicity relation for the Milky Way satellite dwarf galaxies orbiting within 400 kpc as a function of absolute V band magnitude (M_V). The black dots shows the observed metallicity values. Note that these data do not include the Magellanic Clouds. The observations are retrieved from updated data (October 2019) of McConnachie (2012). Left: Turquoise dots shows the model with cooling due collisional ionization equilibrium of atomic gas together with molecular hydrogen cooling while the blue dots shows cooling due to atomic collisional ionization equilibrium cooling.

4.5 Star Formation:

The number of stars formed in halos depends on several factors: cooling of IGM onto the halos, gas cooling the halo, and quantity of gas available. The luminosity of any halo in the simulation is determined by the number of stars formed. Star formation is determined by several methods. Star formation rate densities, time scales, and gas cooling are a few of them. We formulate star formation laws using the star formation rate densities for the disk component and star formation time scales for the spheroid component.

4.5.1 Metal Recycling:

We implement two types of metal recycling for our models, instantaneous and non-instantaneous.

4.5.1.1 Instantaneous

Instantaneous metal recycling consists of stars with the same chemical composition and age. *“Given star formation rate $\phi(t)$, this method assumes a rate of stellar mass of*

$$\dot{M}_*(t) = (1 - R)\phi(t)$$

with a corresponding decrease in fuel mass. The rate of change of metal content from stars follows from the fuel metallicity while that of fuel changes according to

$$\dot{M}_{fuel,Z}(t) = -(1 - R)Z_{fuel}\phi(t) = p\phi(t)$$

In the above R is the instantaneous recycled fraction and p is the yield, both of which are supplied by the IMF subsystem.” (Galacticus Documentation). Rate of change of mass is given in $M_{\dot{o}}/Gyr$

4.5.1.2 Non-Instantaneous

For this method Galacticus assumes fully non-instantaneous recycling and metal enrichment. *“Recycling and metal production rates from simple stellar populations are*

computed, for any given IMF, from stellar evolution models

$$\dot{M}_*(t) = \phi(t) - \int_0^t \phi(t') \dot{R}(t - t'; Z_{fuel}(t')) dt'$$

$$\dot{M}_{fuel}(t) = -\phi(t) + \int_0^t \phi(t') \dot{R}(t - t'; Z_{fuel}(t)) dt$$

$$\dot{M}_{*,Z}(t) = Z_{fuel} \phi(t) - \int_0^t \phi(t') Z_{fuel}(t') \dot{R}(t - t'; Z_{fuel}(t)) dt$$

$$\dot{M}_{fuel,Z}(t) = -Z_{fuel} \phi(t) + \int_0^t \phi(t') Z_{fuel}(t') \dot{R}(t - t'; Z_{fuel}(t')) + \dot{p}(t - t'; Z_{fuel}(t')) dt'$$

where $\dot{R}(t, Z)$ and $\dot{p}(t, Z)$ are the recycling rate and metal yield rates respectively from a stellar population of age t and metallicity Z " (Galacticus Documentation).

Although the luminosity functions look the same (Figure 4.7), the luminosity metallicity relation of models with non-instantaneous metal enrichment is a better match with observations (Figure 4.8). Therefore, from the above two methods, we ran our galaxy models with a non-instantaneous form of metal enrichment.

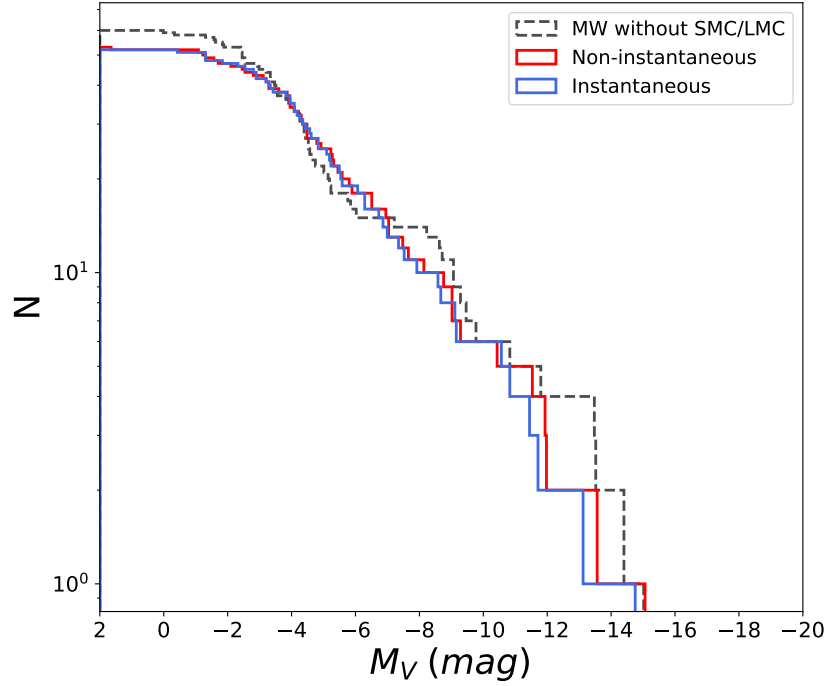


Figure 4.7: Cumulative luminosity function for the Milky Way satellite dwarf galaxies orbiting within 400 kpc as a function of absolute V band magnitude (M_V). The dashed black line shows the observed luminosity function that do not include the Magellanic Clouds. These observations are retrieved from updated data (October 2019) of McConnell (2012). N denotes the number of satellites galaxies per brightness bin. Colored curves shows the galaxy models for different metal enrichment types. Blue curve shows the model with non-instantaneous form of metal enrichment while the yellow curve shows instantaneous form of metal enrichment.

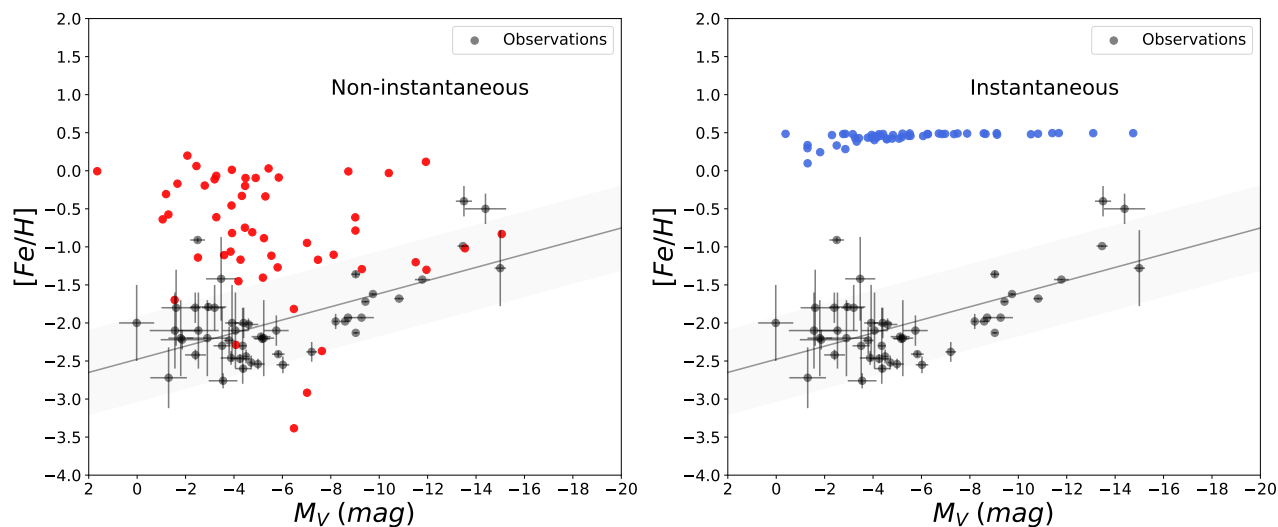


Figure 4.8: Luminosity metallicity relation for the Milky Way satellite dwarf galaxies orbiting within 400 kpc as a function of absolute V band magnitude (M_V). The black dots shows the observed metallicity values from updated data (October 2019) of McConnell (2012). Note that these data do not include the Magellanic Clouds. The observations are retrieved from updated table 1 (October 2019) of McConnell (2012). Left: red dots shows the model with non-instantaneous metal enrichment. Right: blue dots shows instantaneous metal enrichment

4.5.2 Star Formation Rate

The star formation rate is the rate of stars formed in galaxies over time. It determines the number of stars formed, luminosity, and metal enrichment in a galaxy. We use star formation rate density methods available in the Galacticus to form stars in the disk and star formation timescales to determine star formation in the spheroid. Accordingly, stars can form only in halos with gas mass with a surface density higher than a certain threshold.

To determine star formation rate using densities, Galacticus provides several methods including Extended Schmidt 2011 (Shi et al. 2011), Blitz Rosolowsky 2006 (Blitz & Rosolowsky 2006), Kennicutt-Schmidt (Kennicutt 1998), and Krumholz (Krumholz et al. 2009). Each of these methods implements different formulations to calculate star formation rate densities. As, Extended Schmidt and Blitz-Rosolowsky are known to behave well for dwarf galaxies. While we tested all all four methods of these, we focus our discussion on these two.

4.5.2.1 Extended-Schmidt

The Extended-Schmidt method assumes a star formation rate given by (Shi et al. 2011).

$$\dot{\Sigma}_* = A \left(x_H \frac{\Sigma_{gas}}{M_\odot pc^{-2}} \right)^{N_1} \left(\frac{\Sigma_*}{M_\odot pc^{-2}} \right)^{N_2}$$

Parameter A denotes the normalization coefficient while N_1 and N_2 are exponents corresponding to gas and stars. We implement two versions of models for the Extended-Schmidt method for different values of N_1 and N_2 suggested by Shi et al. (2011) and Shi et al.(2018). $N_1 = 1.13$, $N_2 = 0.36$ (Shi et al. 2011) and $N_1 = 1.09$, $N_2 = 0.5$ (Shi et al. 2018).

4.5.2.2 Blitz-Rosolowsky 2006

The star formation method Blitz-Rosolowsky implements a star formation empirical law based on pressure following the the study by (Blitz & Rosolowsky 2006). This method calculates pressure of the Inter-Stellar Medium (ISM) in high and low pressure regimes

based on whether the gas is atomic or molecular (Blitz & Rosolowsky 2006).

The star formation law is given by:

$$\dot{\Sigma}_*(R) = \nu_{SF}(R)\Sigma_{H_2,disk}(R)$$

Here the star formation frequency is given by $\nu_{SF}(R) = \nu_{SF,0} \left[1 + \left(\frac{\Sigma_{HI}}{\Sigma_0} \right)^q \right]$ where Σ_0 is the critical surface density and q is an exponent. The molecular surface density of gas is calculated by

$$\Sigma_{H_2} = \left(\frac{P_{ext}}{P_0} \right)^\alpha \Sigma_{HI},$$

where P_0 is the characteristic pressure and α is the pressure exponent (we use $\alpha = 0.92$ as suggested by Blitz & Rosolowsky (2006)). External hydro-static pressure within a gas cloud in the disk is given by,

$$P_{ext} = \frac{\pi}{4} G \Sigma_{gas} \left[\Sigma_{gas} + \left(\frac{\sigma_{gas}}{\sigma_*} \right) \Sigma_* \right],$$

$\Sigma_* = \sqrt{\pi G h_* \Sigma_*}$ represent the surface density of the stars with $\Sigma_* \gg \Sigma_{gas}$ for h_* disk scale height.

Blitz-Rosolowsky empirical relation overpredicts the luminosity function (Figure 4.9) and luminosity metallicity relation (Figure 4.10). From the above methods we find the Extended-Schmidt to match better with observations (Figure 4.9).

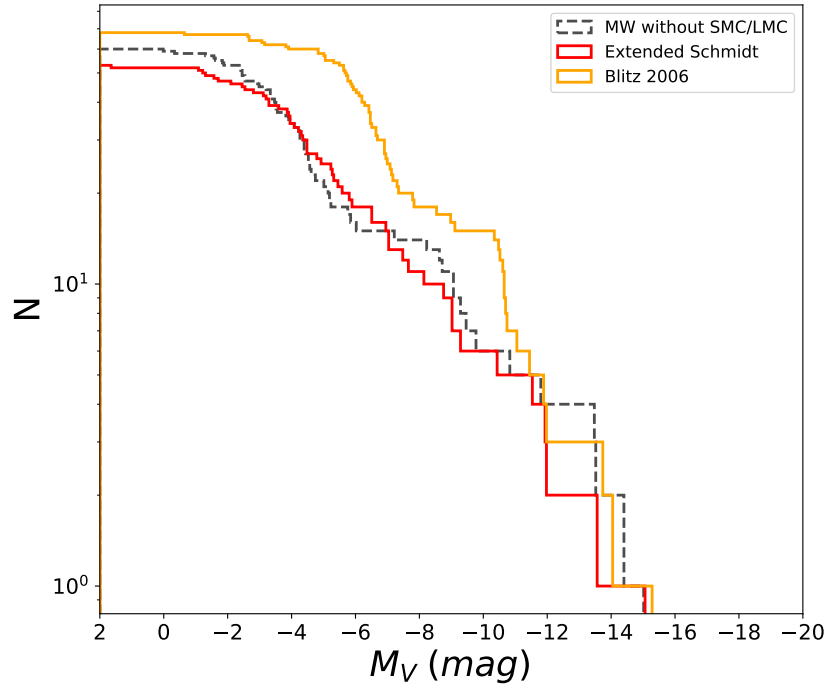


Figure 4.9: Cumulative luminosity function for the Milky Way satellite dwarf galaxies orbiting within 400 kpc as a function of absolute V band magnitude (M_V). The dashed black line shows the observed luminosity function that do not include the Magellanic Clouds. These observations are from updata data (October 2019) of McConnachie (2012). N denotes the number of satellites galaxies per brightness bin. Colored curves shows the galaxy models for different star formation methods. Red curve shows the model with Extended-Schmidt empirical law while the orange curve shows Blitz Rosolowsky empirical law.

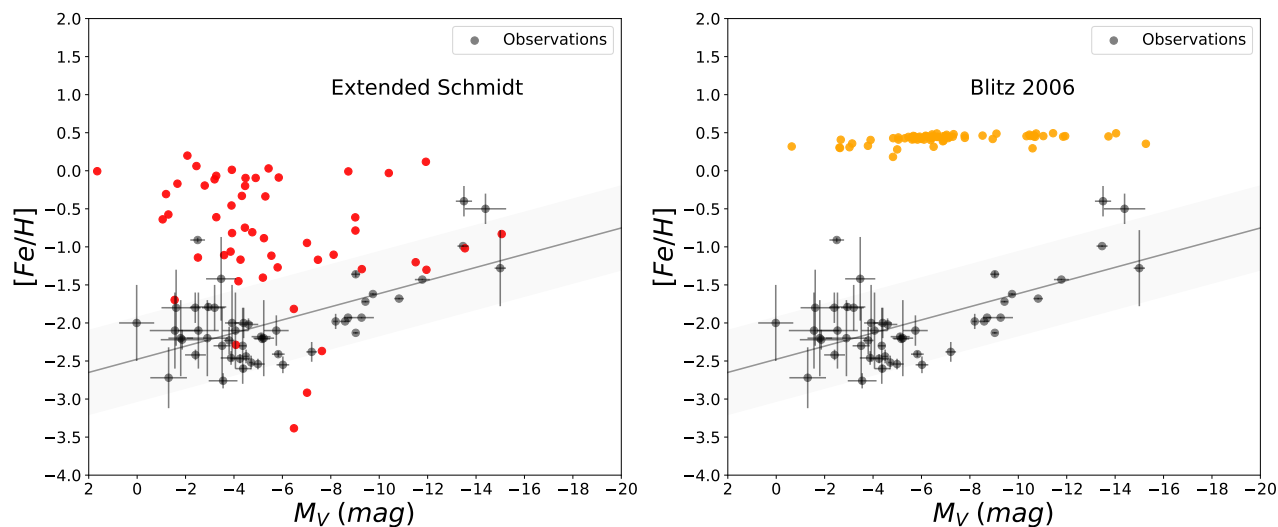


Figure 4.10: Luminosity metallicity relation for dwarf satellites galaxies of the Milky Way within 400 kpc. Observed values are shown in black dots. Observations from updated data (October 2019) of McConnell (2012). Left: Galaxy model where star formation is determined by Extended-Schmidt empirical law. Right: Galaxy model with star formation determined by prescription Blitz Rosolowsky empirical law.

4.6 Outflow of Baryons

Outflow processes are vital for understanding galaxy formation and constraining the properties of dark matter, as the kinematic effects of the outflows can influence the distribution of dark matter (Pontzen & Governato 2012, Sawala et al. 2016). Galacticus has several ejective feedback processes including ram pressure stripping and supernova feedback.

4.6.1 Tidal Stripping

Tidal stripping is the process by which large galaxies strip off gas and . Many dwarf galaxies are subjected to tidal stripping, including the “fossils” which are known to be

relics of the first galaxies (Bovill & Ricotti 2011). Most dwarf spheroidals are shielded from tidal stripping of their stars until $> 90\%$ of the dark matter is lost (Peñarrubia et al. 2008). Tidal stripping, it also instigate metal production and star formation by compressing existing gas reservoirs (Williamson et al. 2016). Hence, these mechanisms have significant effects on the number and luminosity of dwarf galaxies.

According to Williamson et al. (2016), tides can give rise to several effects on a galaxy. They can remove gas from the exterior of a galaxy, produce extended outflows, and decrease velocity dispersion and star formation. However, Williamson et al. (2016) also suggest that tidal stripping from varying tidal fields can create gravitational instabilities fueling star formation and metal production by driving gas towards the halo. Study by Ibata et al. 1994 state that the Saggitarius dwarf is in the process of shedding stars due to interactions with the Milky Way. This shows role of tides in formation and evolution of dwarf galaxies (Williamson et al. 2016). However, studies suggest that the faintest of dwarf galaxies, the ultra faints are less likely to be affected by tidal stripping (Simon 2019). Another study by Errani & Peñarrubia (2020) states that some of the particles bound to cuspy dark matter halos reacts adiabatically to tidal perturbation. Moreover, according to Hayashi et al. (2003), the specific rate of tidal stripping will also depend on the host potential and subhalo orbit.

In order to analyze effects of tidal stripping on Milky Way satellites, we run models with and without tidal striping. Galacticus assumes host halo to be spherically symmet-

ric and calculates its tidal field given using the formula $\mathcal{F} = \frac{GM_{host}(\leq r_p)}{r_p^3} - 4\pi\rho_{host}(r_p) + \omega_p^2$, with pericentric radius r_p . Galacticus calculates the mass loss rate due to tidal stripping by using the formula $\dot{M}_{sat} = -\alpha \frac{M_{sat}(>r_{tidal})}{T_{orbital}}$ with orbital time $T_{orbital} = \frac{1}{\max(\omega/2\pi, v_r/r)}$ with orbital radius r , angular velocity ω , radial velocity v_r , and tidal radius of the satellite galaxy $r_{tidal} = \left(\frac{GM_{sat}}{\omega^2 - d^2\phi/dr^2} \right)^{1/3}$.

Both types of models are run with a reionization suppression redshift of $z = 9$ and filtering velocity of 30 km/s. We compare the simulated luminosity functions and luminosity-metallicity relations to observations. The number of luminous satellites are increased (Figure 4.11). This is probably due to induction of gravitational instability in the the gas clouds that gives rise to star formation. Figure 4.12 shows the luminosity metallicity relation for satellites within 400 kpc of Milky Way for runs with tidal stripping.

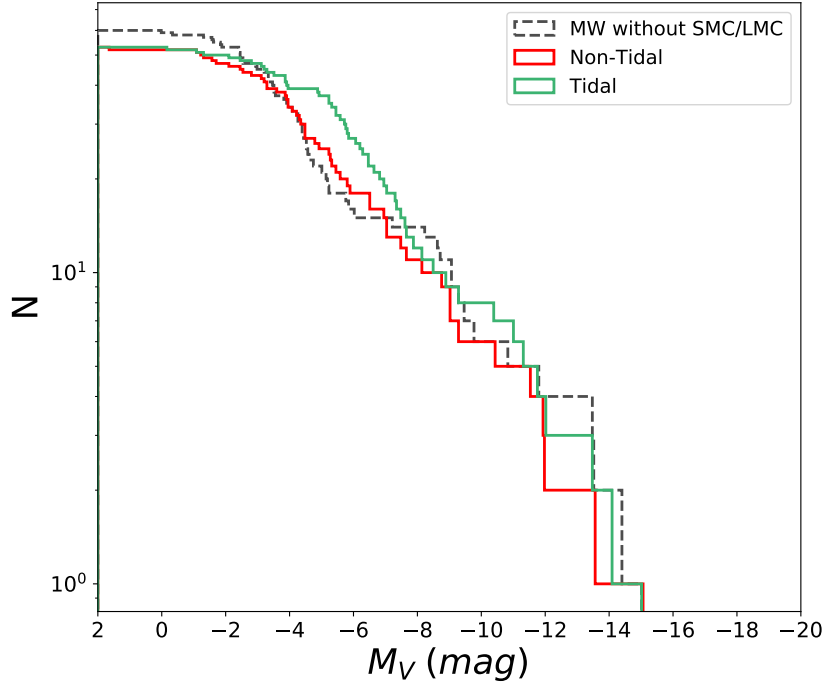


Figure 4.11: Cumulative luminosity function for the Milky Way satellite dwarf galaxies orbiting within 400 kpc as a function of absolute V band magnitude (M_V). The dashed black line shows the observed luminosity function that do not include the Magellanic Clouds. Observations are from updated data (October 2019) of McConnachie (2012). N denotes the number of satellites galaxies per brightness bin. Colored curves shows the galaxy models for galaxy models with non-tidal stripping and tidal stripping respectively. Green curve include only tidal stripping of dark matter while the red curve include tidal stripping of both dark matter and baryons.

Since dark matter is tidally stripped when the N bodysimulation is run, the rest of baryonic matter is stripped by Galacticus when tidal stripping is turned on, but when this mode is turned on it either strips stars from halos very quickly or overproduce stars. Although models run with Galacticus’s tidal stripping produces physical stellar masses, they overestimate the number of satellites between -5 and -8 V band magnitudes. We find the runs without gas/stellar tidal stripping to better match with observations.

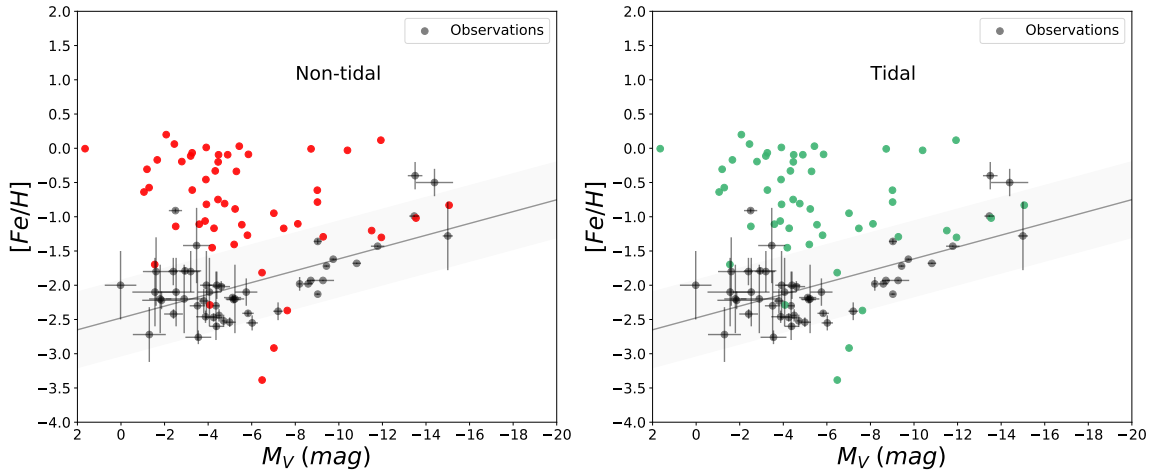


Figure 4.12: Luminosity metallicity relation for the Milky Way satellite dwarf galaxies orbiting within 400 kpc as a function of absolute V band magnitude (M_V). The black dots shows the observed metallicity values. Note that these data do not include the Magellanic Clouds. The observations are retrieved from updated data (October 2019) of McConnachie (2012). Left: green dots shows the model without tidal stripping while the red dots shows galaxy models that include tidal stripping of baryons.

4.6.2 Supernova Feedback

Supernova feedback processes are galactic winds that create massive outflows of gas and dust from galaxies, quenching star formation (Henriques et al. 2019). They play a significant role in star formation physics of dwarf galaxies (Heesen et al. 2019). Given this shallow gravitational potentials of dwarf galaxies, stellar feedback processes can easily expell gas from these galaxies. Supernova explosions, the deaths of massive stars are one of the most powerful events in the universe. They play a significant role in the evolution of dwarf galaxies since they can potentially blow away stars and gas from their shallow potential wells and compress nearby gas to form new stars. There are several classes of supernova based on different progenitors and mechanisms.

Galacticus implements all three types of supernova, Type Ia, II and pair-instability supernovae. Type Ia supernovae are ones that do not exhibit any hydrogen lines but have significant Si II lines in their spectra (Hillebrandt & Niemeyer 2000), while type II contains strong hydrogen lines. Type Ia supernovae are resulted when carbon-oxygen white dwarf in a binary star system goes beyond the Chandrasekhar limit. Typically, the companion star accumulates matter from a donor or they both merge (Hillebrandt & Niemeyer 2000).

Galacticus uses the results from Nagashima et al. (2005) to compute the metal enrichment due to Type Ia supernova (Nagashima et al. 2005). Type II supernova are significantly fainter than type Ia supernova and are the result of core-collapse of massive stars. Their progenitors retain hydrogen and helium envelopes prior to the explosion (Fischera & Schmidt 2009). Pair instability supernova are the explosions of Population III stars. They are believed to be the first stars that enriched the universe with heavy metals (Jeon et al. 2014). Galacticus calculates their properties by computing the energies of pair instability supernovae from the results of Heger and Woosley (2002) (Benson 2011). Pair instability supernova are caused by explosion of stars with cores of about $\sim 40 - 63 M_{\odot}$, $140 M_{\odot} - 260 M_{\odot}$ (Heger & Woosley 2002). The burning of excess helium release thermal energy, which is used up in production of electrons and positrons. Creation of these particles develops a runaway collapse increasing the core temperature. The energy created by fusion exceed the infall collapse which cause the star to explode (Heger & Woosley 2002).

Galacticus provides two types of stellar feedback methods, fixed and power law. These methods calculates the rate of outflow of material from the halos.

Fixed:

If the stellar feedback method is set to fixed, Galacticus assumes an outflow rate of

$$\dot{M}_{outflow} = f_{outflow} \frac{\dot{E}_*}{E_{canonical*}},$$

“where $f_{outflow}$ is the fraction of the star formation rate that goes into outflow, \dot{E}_* is the rate of energy input from stellar populations and $E_{canonical*}$ is the total energy input by a canonical stellar population normalized to $1M_{\odot}$ after infinite time” (Galacticus Documentation).

Power Law:

In the power law method, Galacticus calculates the outflow rate of stellar mass using

$$\dot{M}_{outflow} = \left(\frac{v_{outflow}}{v} \right)^{\alpha_{outflow}} \frac{\dot{E}_*}{E_{canonical*}}$$

“where $v_{outflow} = disk/spheroid$ outflow velocity (in km/s) and $\alpha_{outflow} = disk/spheroid$ outflow velocity exponent are input parameters. v is the characteristic velocity of the component, \dot{E}_* is the rate of energy input from stellar populations and $E_{canonical*}$ is the total energy input by a canonical stellar population normalized to $1 M_{\odot}$ after infinite time” (Galacticus Documentation).

From the above two implementations, we do not see a difference in two galaxy models (Figure 4.13). Therefore, we implement the power law method.

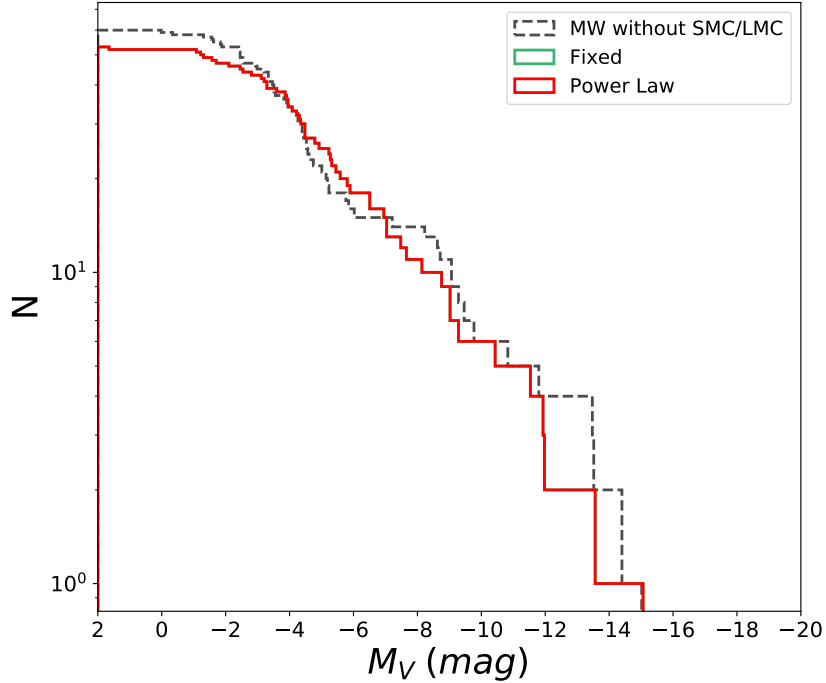


Figure 4.13: Cumulative luminosity function for the Milky Way satellite dwarf galaxies orbiting within 400 kpc as a function of absolute V band magnitude (M_V). The dashed black line shows the observed luminosity function that do not include the Magellanic Clouds. These observations are from updated data (October 2019) of McConnachie (2012). N denotes the number of satellites galaxies per brightness bin. Colored curves shows the galaxy models for galaxy models for different stellar feedback models. Power law in red and fixed method in green (with a fraction of 0.5).

4.7 Best Fit Parameters

Our best fitting model as November 20, 2020 was run with $z_{reionization} v_{filter} = 30 \text{ km/s}$ on AMIGA halo finder outputs. Other notable parameters include $V_{cooling} = 17 \text{ km/s}$, with a non-instantaneous stellar population following a Chabrier Initial Mass Function (IMF

is the initial distribution of stars for a stellar population), and feedback effects following a power law with characteristic velocity 250 km/s and outflow velocity exponent 2.5. A summary of the models we explored and our best fit parameters are shown in Table 4.1.

<i>Notation</i>	<i>Meaning of Parameter</i>	Range of Parameters	<i>Best fit value</i>
$V_{cooling}$	Cooling rate cut off velocity	15 – 25 km/s	17 km/s
$z_{reionization}$	Reionization suppression redshift	7 – 11, 20, 40, 100	9
$V_{reionization}$	Reionization suppression velocity	10, 20, 25, 30, 35, 40, 50 km/s	30 km/s
IMF	Initial mass function	Chabrier 2001 Kennicutt 1983 Kroupa 2001 Miller-Scalo 1979	Chabrier 2001
$\dot{\Sigma}_{SF}$	Star formation rate surface density	Extended Schmidt Blitz Rosolowsky, Kennicutt Schmidt, Krumholz McKee Tumlinson,	$e_* = 0.5, e_{gas} = 1.09$ $\alpha = 0.92$ $e_* = 0.5, e_{gas} = 1.09$ $f = 0.385, C = 5$
$V_{characteristic}$	Characteristic velocity	50, 70, 00, 250 km/s	250 km/s
e	Outflow velocity exponent	2.0, 2.1, 2.2, 2.3, 2.4, 2.5	2.5
$e_{ram\ pressure}$	hotHaloOutflowStrippingEfficiency	Ram pressure stripping efficiency	0.1

Table 4.1: Summary of best fit parameters for satellite dwarf galaxies orbiting within 400 kpc of Milky Way. Note that these simulated models are based on AMIGA’s halo finder.

Chapter 5

Discussion

5.0.1 Gas Cooling

We find reionization to be a major contributor for the cooling of gas from the IIGM and the hot halo. Our model agrees with the epoch of reionization at $z = 9$ with preventive feedback effects turned on. However, each parameter set alone does not result in physical stellar masses. They interplay with each other to produce correct stellar masses especially in low mass halos.

5.0.2 Mass Accretion

Comparison with observed luminosity functions and luminosity metallicity relations for dwarf satellites suggests that mass accretion does not follow separate hot or cold components. We find it important to include preventive feedback in our models in order to simultaneously match the luminosity function and the luminosity metallicity relation. Similar results are also found by previous studies (e.g. Lu et al. 2017, Font et al. 2011).

5.0.3 Star Formation

The stellar population of Milky Way satellites is best matched by a non-instantaneous. Recycling and enrichment of metals. The star formation rate density of the dwarf satellites follow the Extended Schmidt law by (Shi et al. 2011). This law has been tested on low brightness galaxies and hence is known to work well for dwarf galaxies.

5.0.4 Outflow of Baryons

Stellar material takes place due to tidal stripping, and stellar feedback.

Most of the dark matter contained in the satellite galaxies are already tidally stripped in the N-body simulation. Therefore, we find it counterproductive to turn on tidal stripping in the Galacticus since it strips off most of the stars in halos.

Supernova feedback and stellar winds control the amount of gas and stars in the dwarf satellites, due to their shallow gravitational potential. Feedback effects due to type Ia, II and pair instability supernova expels mass from the halos at a rate that follows a power law. This mass flow rate is inversely proportional to characteristic velocity. We find characteristic velocity to be $v_{characteristic} = 250 \text{ km/s}$ for the best fitting model. Moreover, rate of mass expelled also depends on the exponent which is $e \sim 2.5$. We do not find efficiency of ram pressure stripping to have an effect on the luminosity and luminosity relations for our models.

5.1 Properties of Best Fit Model

Luminosity Function: Luminosity function of the best fitting model described above matches well for faint satellites. However, our model does not produce enough luminous satellites past -16 magnitudes to match well with observations. Luminosity function of the simulated galaxies matches with observations once the SMC/LMC is excluded from the sample. Our results agree with the hydrodynamic simulation, “Ruth” by (Akins et al. 2020). Further analysis shows that our Milky Way satellites do not contain the Small Magellanic Cloud (SMC) and the Large Magellanic Cloud (LMC). Thus, comparison of luminosity functions of observed dwarf satellites without the LMC/SMC pair yields a better fit (Figure 5.1). Previous studies suggests that it is extremely rare to have Magellanic clouds in Milky Way type simulations. According to Liu et al. (2011), 81% of Milky Way analogs have no such satellites, 11% have one and 3.5% have no hosts. Given this fact and that we have one Milky Way analog, it is reasonable for our simulation to not include an SMC/LMC pair.

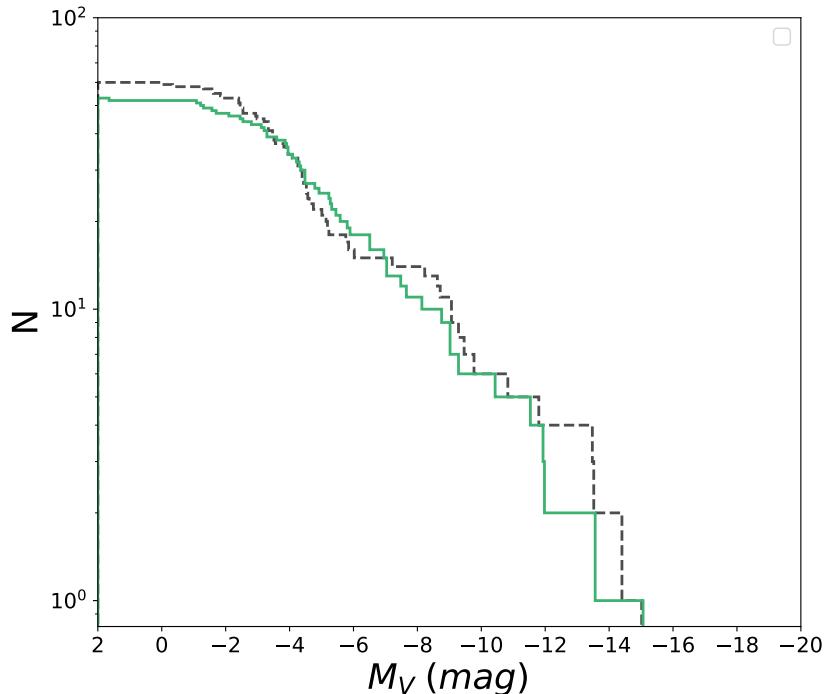


Figure 5.1: Cumulative luminosity function for the Milky Way satellite dwarf galaxies orbiting within 400 kpc as a function of M_V . N denotes the number of satellite galaxies per brightness bin. The dashed black line shows the observed luminosity function that do not include the Magellanic Clouds. Observations are from McConnachie (2012) (see table 3.1). Galaxy models run with AMIGA and ROCKSTAR halo finder outputs are color coded with green and blue respectively.

Luminosity Metallicity Relation:

¹ The luminosity-metallicity relation of our model is well within the observed values between $-8 \leq M_V \leq -20 \text{ mag}$. However, the metallicity of fainter satellites between $-4 \leq M_V \leq -8 \text{ mag}$ are overestimated. We find it difficult to constrain the luminosity function and the luminosity metallicity relation at the same time. Our metallicity values are very high for some faint halos (Figure 5.2). Therefore, further exploration of the parameter space is required to refine the fit.

¹The global metallicity for the simulated dwarfs is calculated using the formula $[Z/H] = \log_{10}(\frac{M_Z}{M_*}) - [Z/H]_{\odot}$.

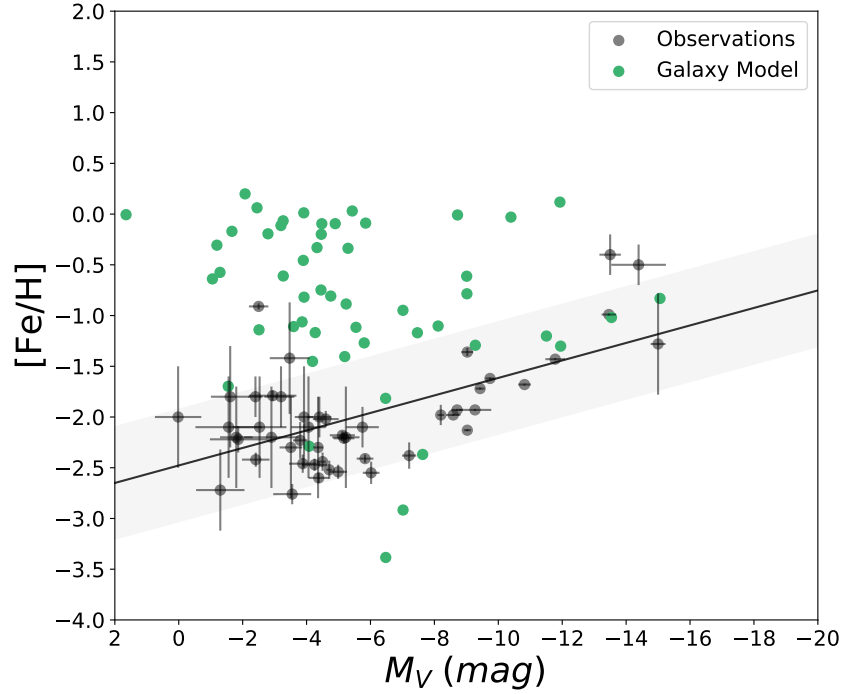


Figure 5.2: Luminosity metallicity relation for the Milky Way satellite dwarf galaxies orbiting within 400 kpc as a function of M_V . The black dots shows the observed metallicity values retrieved from updated data (October 2019) of McConnell (2012). Note that these data do not include the Magellanic Clouds. Green dots shows the model the current best fit galaxy model.

Velocity Dispersion:

Stellar velocity dispersion of the dwarf satellites for the best fit model is well within the observed values although slightly overestimated for luminous satellites (Figure 5.3). This suggests that our modeled satellites contain the right amount of dark matter mass for faint halos and more dark matter on luminous satellites when compared to observed galaxies.

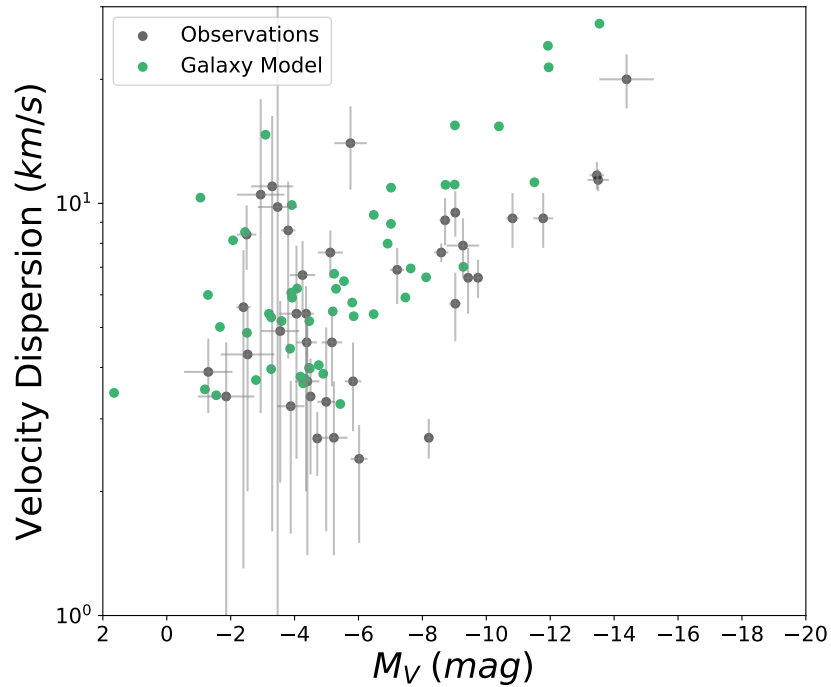


Figure 5.3: Velocity dispersion vs luminosity relation of Milky Way satellites. Black points represents the observations while green points represents the best fit galaxy model. See table 3.1 for observations from McConnachie (2012).

Mass to Light Ratio:

The mass to light ratio of the modelled Milky Way satellites agrees well with the observations (Figure 5.4). This suggests that the halos produce sufficient stars at a given dark matter mass.

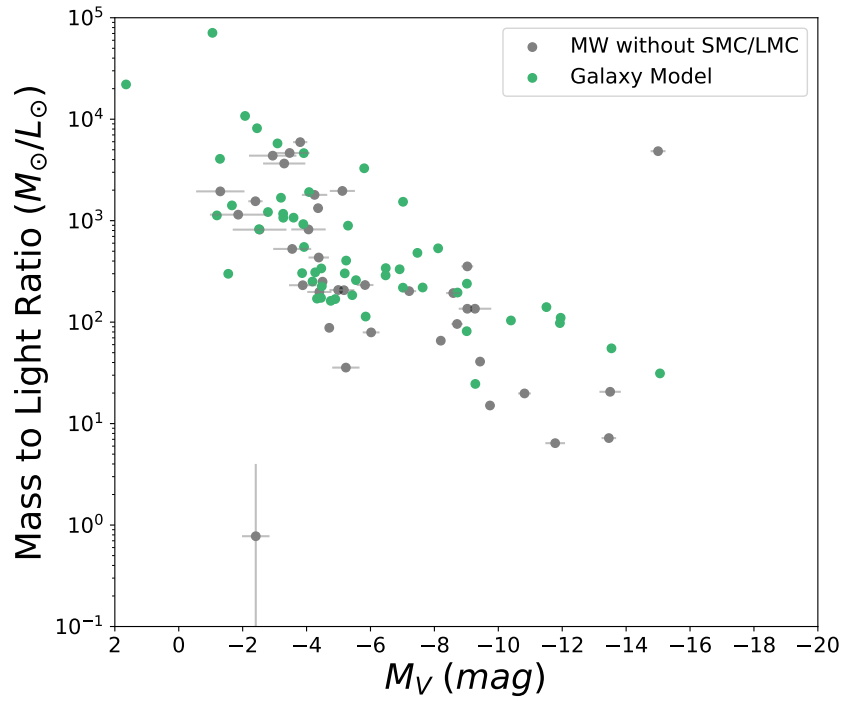


Figure 5.4: Mass to Light ratio of dwarf satellites orbiting Milky Way. We plot mass to light ratio of galaxies in solar units as a function of absolute V band magnitude. Black points represents the observations while green points represents the best fit galaxy model. See table 3.1 for observations from McConnachie (2012).

Luminosity vs Half Light Radius:

Luminosity vs Half light radius of the modelled halos match well with the observed properties (Figure 5.5).

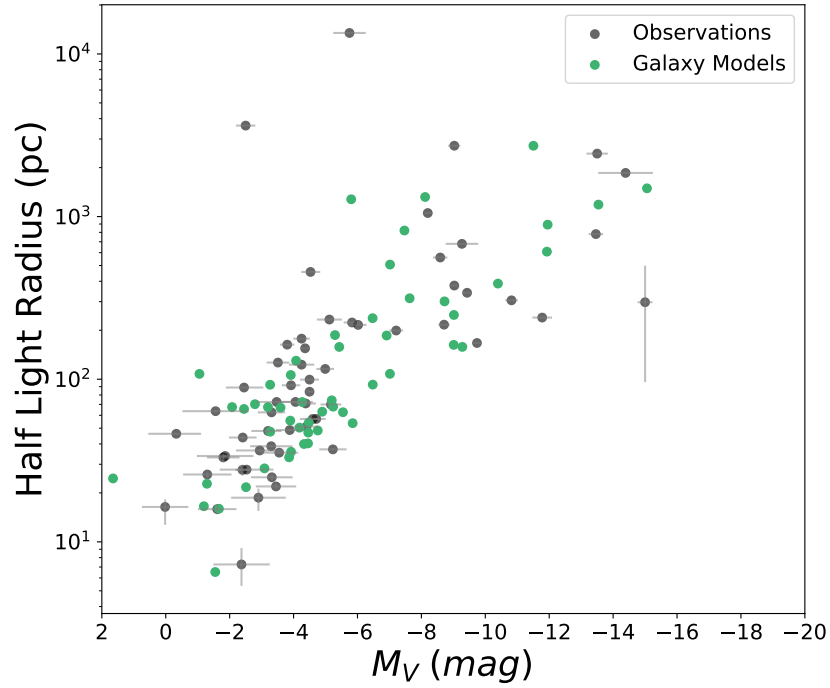


Figure 5.5: Luminosity vs half light radius relation of Milky Way satellites. Black points represents the observations while green points represents the best fit galaxy model. See table 3.1 for observations from McConnell (2012).

Luminosity vs Distance:

The distribution of the distances of our modeled dwarfs from the Milky Way is consistent with observations. (Figure 5.6). However, the majority of the modelled galaxies lie beyond 50 kpc from the center of the Milky Way analog, as expected given the detection biases of the halo finders.

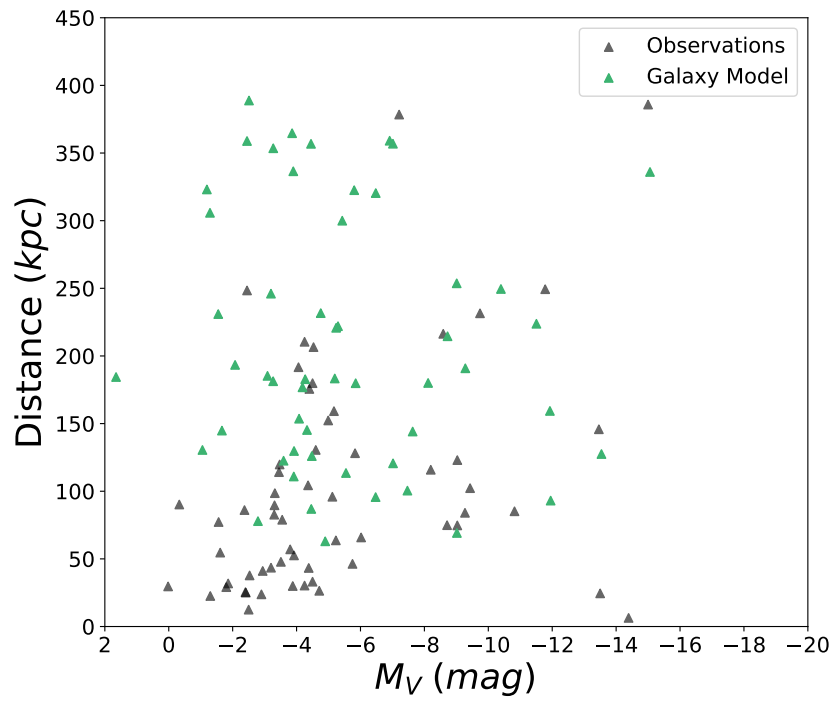


Figure 5.6: Distance of the dwarf satellites orbiting Milky Way (in kpc) as a function of absolute V band magnitude. Observed distances are shown in black triangles. Green triangles shows the distances predicted by the best fit model. See table 3.1 for observations from McConnachie (2012).

Chapter 6

Conclusion

In this project we explored the extensive parameter space of a semi-analytic galaxy formation model Galacticus (Benson 2011) within the cosmological evolution of Λ CDM the satellite system of a Milky Way analog. We find that galaxy models produced by AMIGA halo finder matches better with observations. The Milky Way satellite population in our models match well with observed luminosities, mass to light ratios, velocity dispersion, half light radius luminosity relations and luminosity distance relations. We find it necessary to suppress star formation in low mass halos in order to produce the observed luminosity metallicity relation. Our best fit model produces luminosity functions that match well with observations without the SMC/LMC pair. Therefore, our simulation do not produce the SMC/LMC pair, in agreement with previous studies it is extremely rare to have LMC in Milky Way analogs (Tollerud et al. 2011, Liu et al. 2011). Although, our luminosity function matches well for most halos, we have a few that exhibit higher metallicities than expected. This may be either due to over stripping of stars in halos or overproducing metals in stars.

Chapter 7

Future Work

In the future, we hope to test constrained star formation physics parameters of Milky Way satellites on Centaurus A. Centaurus A is a galaxy located about 3.7 Mpc away and host to a number of dwarf galaxies. It is much more massive than Milky Way, but less massive than a galaxy cluster like Fornax or Virgo. Centaurus A is the closest elliptical and its estimated virial mass places it between group and cluster scales, making it ideal for investigating the effects of local environment on the formation and evolution of dwarf galaxy populations. Current dwarf galaxy studies have explored only star formation physics of Dwarf Galaxies in the Local Group and ones that reside in massive clusters. Therefore, this project will explore the universality of the star formation in dwarf galaxies of the Local Volume.

We will model the dwarf satellite populations of Centaurus A using a suite of high resolution N-body simulations and Galacticus (Benson 2011). Given the relatively low computational cost of N-body simulations and SAMs, we will be able to explore the ef-

fects of uncertainties in the Centaurus A system, including its relatively unconstrained virial mass.

At the time of submission several specific questions need to be answered.

- What causes the difference in galaxy models based on the two different halo finders?
We will investigate the cause for the different results produced by the ROCKSTAR and AMIGA halo finders. Although AMIGA produced best results for Milky Way, it is likely not feasible to process large simulations of Centaurus A. Therefore, further analysis needs to be undertaken on ROCKSTAR in order to produce the same results as AMIGA.
- Why do some halos have metallicity values higher than the observed? We will further explore the parameter space to obtain a better fit for the luminosity-metallicity relation.
- Galacticus produces galaxy models of the ultra faint dwarf galaxies fairly well. This is contrary to what we expected. What would happen if we model the Milky Way satellites without the ultra faint dwarf galaxy population?

Appendix A

Halo Finders

A.1 AMIGA Halo Finder

AHF uses adaptive mesh refinement technique to identify halos in the simulation. First the particles are grouped according to their densities. Once the particle density contours are identified density profiles are calculated. Here, density profile is the distribution of density of particles within halo radius. Next, halo edges are calculated and outliers are removed based on escape velocity of dark matter particles. Unbound particles are removed iteratively if $v_i \geq v_{esc} = \sqrt{2\phi(i)}$, i.e. where $\phi(i)$ is the potential and v_{esc} is the escape velocity of the particle respectively. One disadvantage to this algorithm is that it may group particles belonging to a subhalo as part of the host halo if the particles are located too close to the halo. This dependence of the algorithm density of halos and may result in missing halos.

A.2 ROCKSTAR Halo Finder

We use Robust Overdensity Calculation using K-Space Topologically Adaptive Refinement (ROCKSTAR) by Behroozi et al. (2013a) to explore properties of the simulation. It is a 6D FOF algorithms and runs faster compared to spherical overdensity algorithms. Unbinding criteria is given by the minimum distance based on relative error of particle potential θ ,

$$d(\theta) \geq \frac{r_{max}}{2} + \sqrt{\left(\frac{r_{max}}{2}\right)^2 + \frac{\sigma_x^2}{\theta}},$$

where r_{max} is the maximum distance of the particle from the halo center and σ_x is the standard deviation of the particle with respect to the center of the halo (Behroozi et al. 2013a). We process each snapshot in the simulation through ROCKSTAR halo finder. ROCKSTAR takes around 10 minutes per snapshot for a total of 222 snapshots in the Milky Way simulation.

A.3 Other Parameters for Models based on AMIGA

A.3.1 Ram Pressure Stripping

The ram pressure is an additional pressure created by movement of a galaxy through a medium. As satellite galaxies fall into the host halo, gas is stripped off from the halos of satellites galaxies due to ram pressure. Galacticus computes the ram pressure force due to the hot halo using the algorithm of Font et al. (2008),

$$\mathcal{F}_{hot,host} = \rho_{hot,host}(r_{peri})v^2(r_{peri}),$$

where $v(r)$ is the orbital velocity of the node in that host, r_{peri} is the pericentric radius of the node's orbit, and $\rho_{hot,host}(r)$ is the hot halo density profile of the node's host halo. The ram pressure stripping force is calculated using Font et al. 2008,

$$\alpha_{rp} \frac{GM_{satellite}(r_{rp})\rho_{hot,satellite}(r_{rp})}{r_{rp}} = \mathcal{F}_{hot,host},$$

where $\mathcal{F}_{hot,host}$ is the ram pressure force induced in the hot halo, and $M_{satellite}(r)$ is the total mass of a satellite galaxy within radius r . “The parameter α_{rp} is a geometric factor of order unity” (Galacticus Documentation).

Galacticus calculates the ram pressure stripping timescale from the acceleration which is derived from the ram pressure force following Roediger & Brüggen (2008),

$$\alpha_{rampressure} = P_{rampressure}/\Sigma$$

“where $P_{rampressure}$ is the ram pressure force per unit area, and Σ is the surface density of gas. The associated timescale to accelerate gas over a distance r_{outer} (the current outer radius of the hot halo) is then:”

$$\tau_{rampressure} = \sqrt{2R_{outer}\Sigma_{outer}/P_{rampressure}},$$

Galacticus calculates the mass loss rate due to tidal stripping by:

$$\dot{M}_{gas,disk} = \min\left(\frac{\mathcal{F}_{hot,host}}{2\Sigma_{gas}(r_{half})\Sigma_{total}(r_{half})}, R_{max}\right) \frac{M_{gas,disk}}{\tau_{dyn,disk}}$$

“where $\mathcal{F}_{hot,host}$ is the ram pressure force due to the hot halo of the node’s host computed using the selected hot halo ram pressure force method” (Galacticus Documentation). Parameters $\Sigma_{total}(r)$ represents total surface density in the disk, $\Sigma_{gas}(r)$ - gas surface density in the disk, r_{half} - disk half-mass radius, $M_{gas,disk}$ - total gas mass in the disk, and $\tau_{dyn,disk} = r_{disk}/v_{disk}$ - the dynamical time in the disk where “ $\alpha = \mathcal{F}_{hot,host}/\mathcal{F}_{gravity}$ and, $\mathcal{F}_{gravity} = \frac{4}{3}\rho_{gas}r_{1/2}\frac{GM_{total}(r_{1/2})}{r_{1/2}}$ is the gravitational restoring force in the spheroid at the half-mass radius, $r_{1/2}$ ” (Galacticus Documentation). Mass loss rate of the satellite spheroids is given by $\dot{M}_{gas} = -max(\alpha, R_{max})M_{gas}\tau_{spheroid}$, where R_{max} is maximum ram pressure stripping mass loss rate Spheroid simple fractional rate (Galacticus Documentation).

We use a default value of 0.1 for the ram pressure stripping efficiency. Although models with $e=0.01$, 0.05, and 0.1 were run to test the effect of ram pressure stripping efficiency, it has little to no effect on the luminosity and metallicity of the models (Figure A.1).

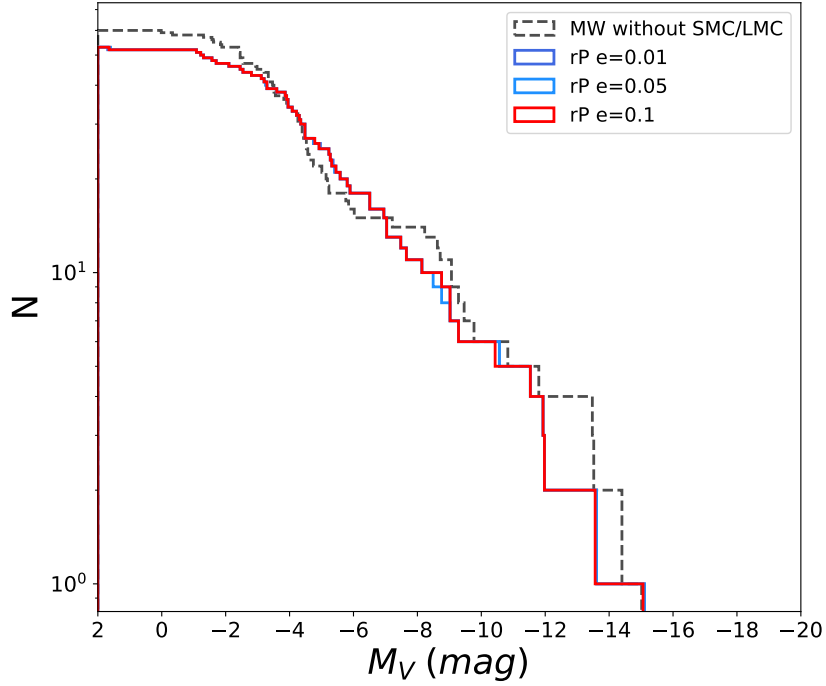


Figure A.1: Cumulative luminosity function for the Milky Way satellite dwarf galaxies orbiting within 400 kpc as a function of M_V . N denotes the number of satellite galaxies per brightness bin. The dashed black line shows the observed luminosity function that do not include the Magellanic Clouds. Observations are from McConnachie (2012) (see table 3.1). Colored lines shows the simulated dwarf galaxies for different ram pressure stripping efficiencies.

A.3.2 Characteristic Velocity and Outflow Rate Exponent

We test two parameters for this method: characteristic velocity and exponent. Varying characteristic velocity for 50, 70, 100, 250 km/s produce models with same luminosity functions when run with rest of the best fit parameters given in Table 4.1 for both instantaneous and non-instantaneous types of metal enrichment. Corresponding luminosity metallicity relations are also the same for all models (Figure A.2, and Figure A.4). We do not find any difference in luminosity functions for models based on non-instantaneous

metal enrichment. Therefore we use $v_{characteristic} = 250 \text{ km/s}$.

Next, we vary outflow velocity exponent for $e=2.0, 2.1, 2.2, 2.3, 2.4, 2.5$. These models also seem to produce similar luminosity functions and luminosity metallicity relations.

Therefore, we choose $e = 2.5$ for this parameter.

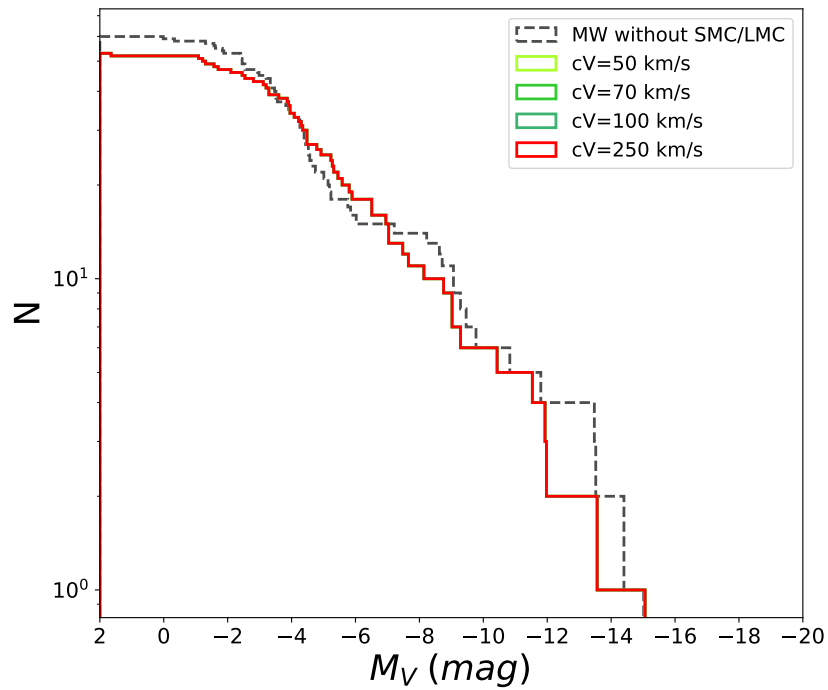


Figure A.2: Luminosity function of dwarf satellites within 400 kpc of the Milky Way. Observations are from McConnachie (2012). See Table 3.1 for details. Colored curves represent simulated models with different characteristic velocities.

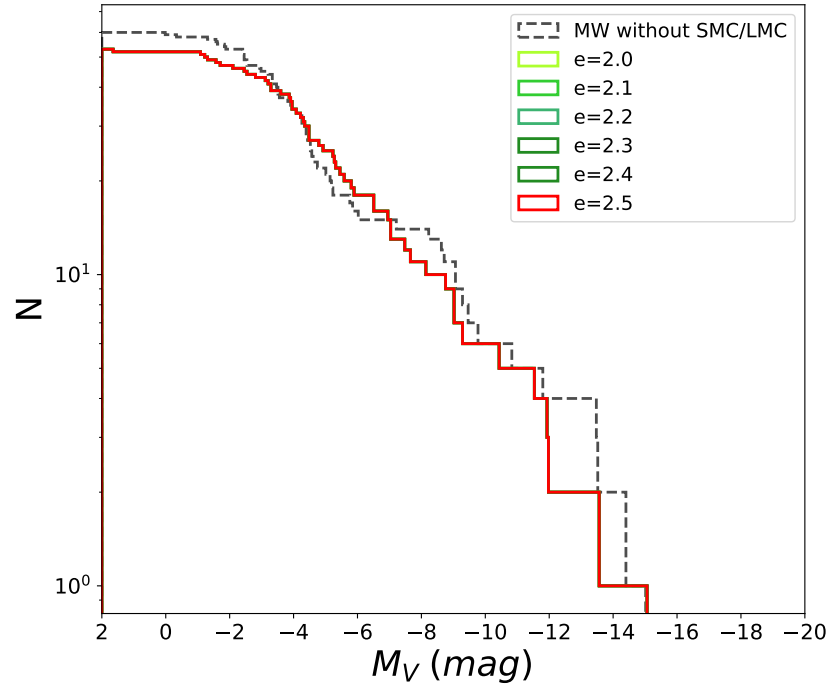


Figure A.3: Luminosity function of dwarf satellites within 400 kpc of the Milky Way. Observations are from McConnachie (2012). See Table 3.1 for details. Colored curves represent simulated models with different outflow velocity exponents.

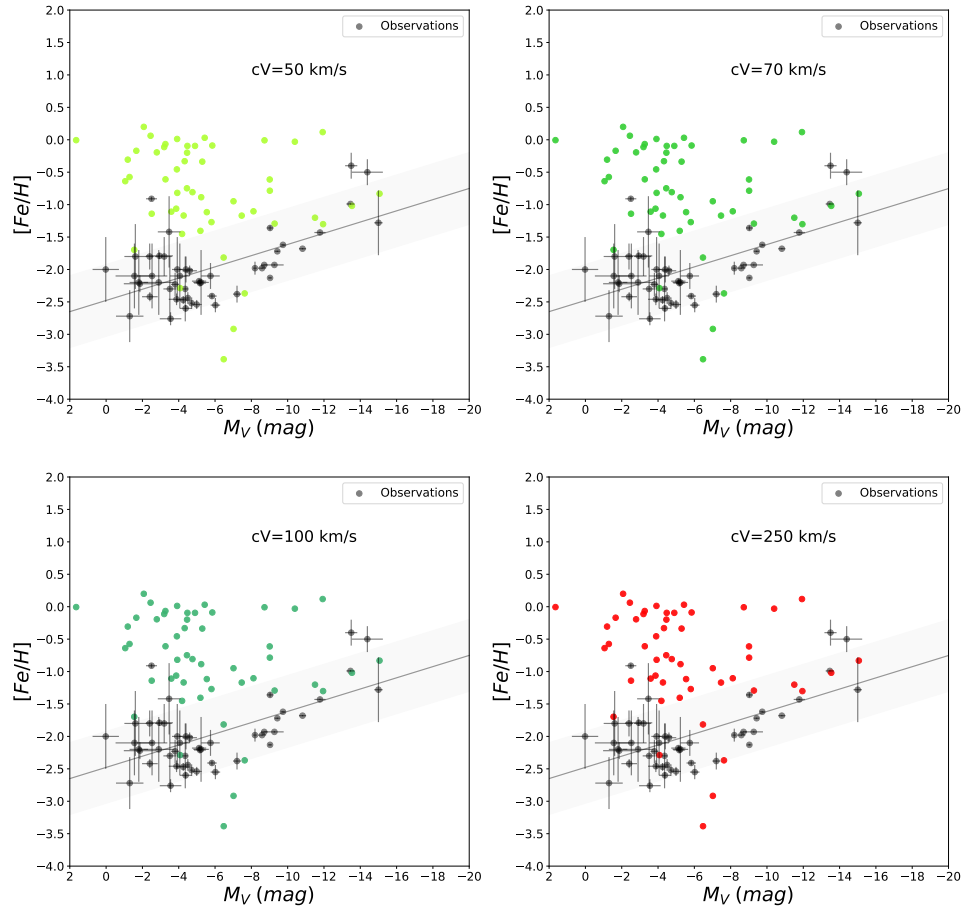


Figure A.4: Luminosity function of galaxy models based on AMIGA with non-instantaneous stellar population for different characteristic velocities. (b) Luminosity function of galaxy models based on AMIGA with non-instantaneous stellar population for different outflow velocity exponents

A.3.3 Star Formation Laws

Kennicutt-Schmidt

The Kennicutt Schmidt law is a simple gas density power law. It is known to work

well for starburst galaxies (Kennicutt 1998). The star formation density rate is given by

$$\dot{\Sigma}_* = A \left(\frac{\Sigma_H}{M_\odot pc^{-2}} \right)^N,$$

where A is a normalization constant and N is the star formation exponent. We use a value of $N = 1.4$ as suggested by Kennicutt (1998).

Krumholz-McKee-Tumlinson

The default star formation rate density method for Galacticus is Krumholz-McKee-Tumlinson. This method assumes a star formation rate given by (Krumholz et al. 2009). This method determines the star formation rate density by Krumholz (2005). In this model, Galacticus calculates the star formation rate surface density by

$$\dot{\Sigma}_* = \nu_{SF} f_{H_2}(R) \Sigma_{HI,disk}(R) \begin{cases} (\Sigma_{HI}/\Sigma_0)^{-1/3}, & \text{if } \Sigma_{HI}/\Sigma_0 \leq 1 \\ 0, & \text{if } \Sigma_{HI}/\Sigma_0 > 1 \end{cases}$$

where ν_{SF} is the star formation frequency and $\Sigma_0 = 85 M_\odot pc^{-1}$.

“The molecular fraction is given by $f_{H_2} = 1 - \frac{3s/4}{1+s/4}$, where $\delta = 0.0712[0.1s^{-1} + 0.065]^{-1/5}$ and $s = \frac{\ln(1+0.6\chi+0.01\chi^2)}{0.04\Sigma_{comp,0}Z}$, with $\chi = 0.77[1+3.1Z^{0.365}]$ and $\Sigma_{comp,0} = c\Sigma_{HI}/M_\odot pc^{-2}$ ”

(Galacticus Documentation).

Both simulated galaxies produced with Kennicutt-Schmidt and Krumholz McKee Tumlinson methods overpredict the luminosities of the dwarf satellite population. (Figure A.5)

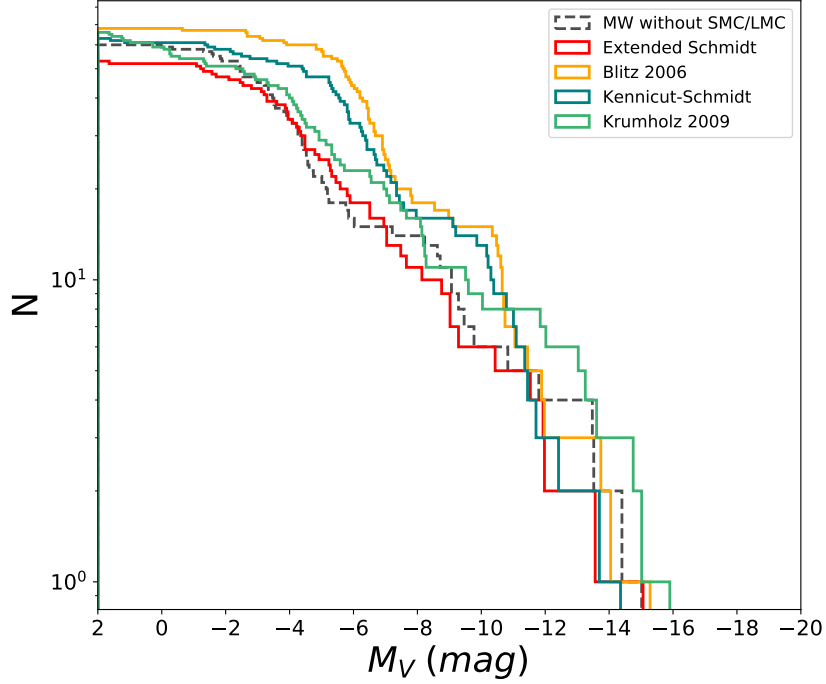


Figure A.5: Cumulative luminosity function for the Milky Way satellite dwarf galaxies orbiting within 400 kpc as a function of M_V . N denotes the number of satellite galaxies per brightness bin. The dashed black line shows the observed luminosity function that do not include the Magellanic Clouds. Observations are from McConnachie (2012) (see Table 3.1). Colored curves shows the luminosity functions for different star formation rate density empirical laws.

A.3.4 Initial Mass Function (IMF)

The initial mass function (IMF) represents the distribution of stellar masses in a cluster of stars based on an average from observations of stars in our Milky Way (Villaume et al. 2017). Galacticus provides us with four initial mass functions, Chabrier 2001, Kennicutt 1983, Kroupa 2001 and Miller Scalo 1979. Our default IMF is Chabrier 2001. Analysis of luminosity functions and luminosity metallicity relations reveal that they are not very different from each other (Figure A.6 and Figure A.7). Therefore, we use the default

IMF (Chabrier 2001) for our models.

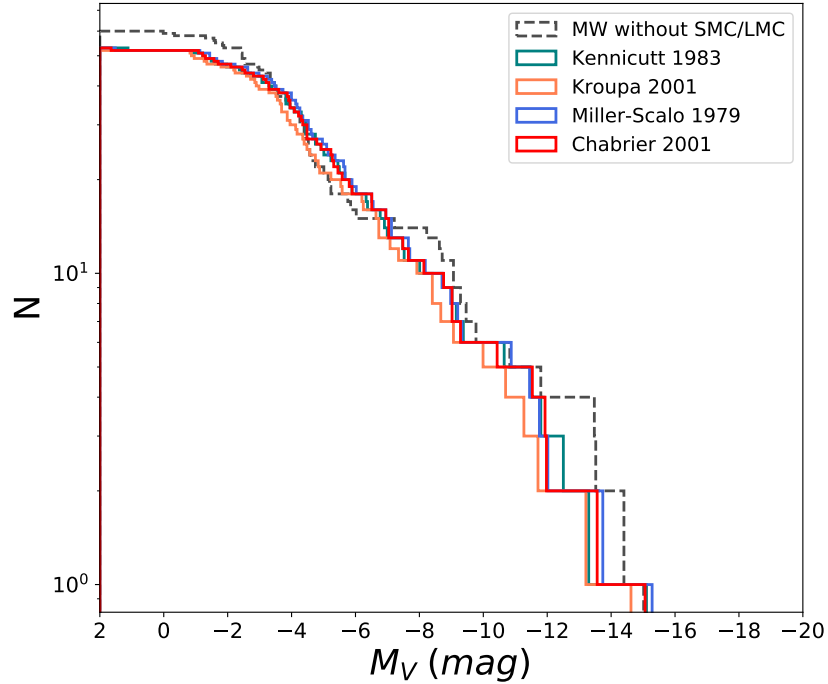


Figure A.6: Cumulative luminosity function of the simulated Milky Way satellites within 400 kpc for different initial mass functions. Number of satellites as a function of M_V . Black dashed curve shows the observed luminosity function. These observations are from updated data (October 2019) of McConnachie (2012). Colored curves shows luminosity functions for different IMFs.

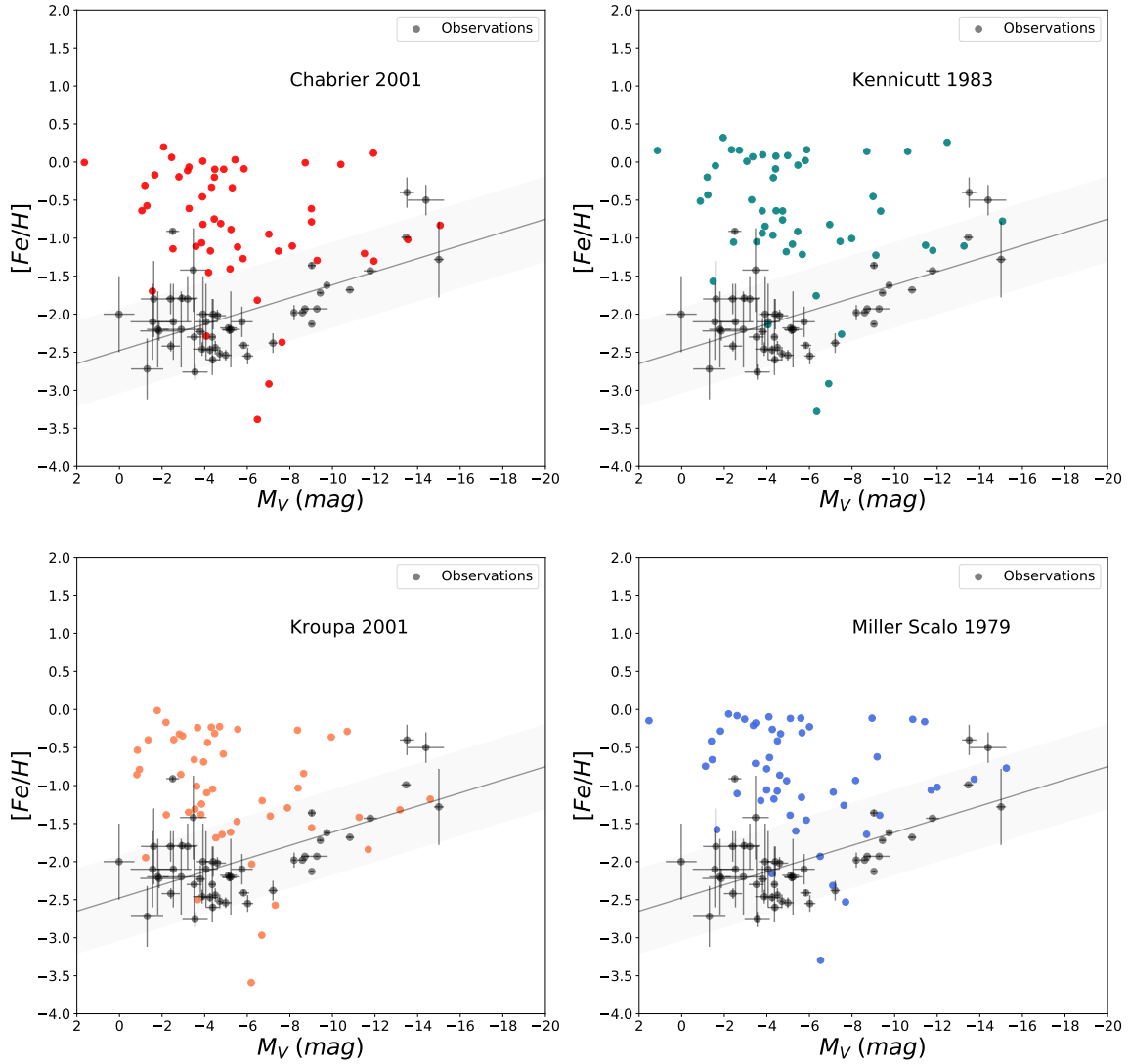


Figure A.7: Cumulative luminosity function for the Milky Way satellite dwarf galaxies orbiting within 400 kpc as a function of M_V . denotes the number of satellites galaxies per brightness bin. The dashed black line shows the observed luminosity function that do not include the Magellanic Clouds. Observations are from McConnachie (2012) (Table 3.1). Galaxy models run with different IMFs are shown in different colors. Top left: Chabrier 2001, Top right: Kennicutt 1983, Bottom left: Kroupa 2001, Bottom Right: Miller-Scalo 1979.

Bibliography

Abbott, T. M. C., Abdalla, F. B., Alarcon, A., Aleksić, J., Allam, S., Allen, S., Amara, A., Annis, J., Asorey, J., Avila, S., Bacon, D., Balbinot, E., Banerji, M., Banik, N., Barkhouse, W., Baumer, M., Baxter, E., Bechtol, K., Becker, M. R., Benoit-Lévy, A., Benson, B. A., Bernstein, G. M., Bertin, E., Blazek, J., Bridle, S. L., Brooks, D., Brout, D., Buckley-Geer, E., Burke, D. L., Busha, M. T., Campos, A., Capozzi, D., Carnero Rosell, A., Carrasco Kind, M., Carretero, J., Castander, F. J., Cawthon, R., Chang, C., Chen, N., Childress, M., Choi, A., Conselice, C., Crittenden, R., Crocce, M., Cunha, C. E., D’Andrea, C. B., da Costa, L. N., Das, R., Davis, T. M., Davis, C., De Vicente, J., DePoy, D. L., DeRose, J., Desai, S., Diehl, H. T., Dietrich, J. P., Dodelson, S., Doel, P., Drlica-Wagner, A., Eifler, T. F., Elliott, A. E., Elsner, F., Elvin-Poole, J., Estrada, J., Evrard, A. E., Fang, Y., Fernandez, E., Ferté, A., Finley, D. A., Flaughner, B., Fosalba, P., Friedrich, O., Frieman, J., García-Bellido, J., Garcia-Fernandez, M., Gatti, M., Gaztanaga, E., Gerdes, D. W., Giannantonio, T., Gill, M. S. S., Glazebrook, K., Goldstein, D. A., Gruen, D., Gruendl, R. A., Gschwend, J., Gutierrez, G., Hamilton, S., Hartley, W. G., Hinton, S. R., Honscheid, K., Hoyle, B., Huterer, D., Jain, B., James, D. J., Jarvis, M., Jeltema, T., Johnson, M. D., Johnson, M. W. G., Kacprzak, T., Kent, S., Kim, A. G., King, A., Kirk, D., Kokron, N., Kovacs, A., Krause, E., Krawiec, C., Kremin, A., Kuehn, K., Kuhlmann, S., Kuropatkin, N., Lacasa, F., Lahav, O., Li, T. S., Liddle, A. R., Lidman, C., Lima, M., Lin, H., MacCrann, N., Maia, M. A. G., Makler, M., Manera, M., March, M., Marshall, J. L., Martini, P., McMahon, R. G., Melchior, P., Menanteau, F., Miquel, R., Miranda, V., Mudd, D., Muir, J., Möller, A., Neilsen, E., Nichol, R. C., Nord, B., Nugent, P., Ogando, R. L. C., Palmese, A., Peacock, J., Peiris, H. V., Peoples, J., Percival, W. J., Petravick, D., Plazas, A. A., Porredon, A., Prat, J., Pujol, A., Rau, M. M., Refregier, A., Ricker, P. M., Roe, N., Rollins, R. P., Romer, A. K., Roodman, A., Rosenfeld, R., Ross, A. J., Rozo, E., Rykoff, E. S., Sako, M., Salvador, A. I., Samuroff, S., Sánchez, C., Sanchez, E., Santiago, B., Scarpine, V., Schindler, R., Scolnic, D., Secco, L. F., Serrano, S., Sevilla-Noarbe, I., Sheldon, E., Smith, R. C., Smith, M., Smith, J., Soares-Santos, M., Sobreira, F., Suchyta, E., Tarle, G., Thomas, D., Troxel, M. A., Tucker, D. L., Tucker, B. E., Uddin, S. A., Varga, T. N., Vielzeuf, P., Vikram, V., Vivas, A. K., Walker, A. R., Wang, M., Wechsler, R. H., Weller, J., Wester, W., Wolf, R. C., Yanny, B., Yuan, F., Zenteno, A., Zhang, B., Zhang, Y., Zuntz, J., & Dark Energy Survey Collaboration. 2018, , 98, 043526

Aguado, D. S., Ahumada, R., Almeida, A., Anderson, S. F., Andrews, B. H., Anguiano, B., Aquino Ortíz, E., Aragón-Salamanca, A., Argudo-Fernández, M., Aubert, M.,

Avila-Reese, V., Badenes, C., Barboza Rembold, S. r., Barger, K., Barrera-Ballesteros, J., Bates, D., Bautista, J., Beaton, R. L., Beers, T. C., Belfiore, F., Bernardi, M., Ber-shady, M., Beutler, F., Bird, J., Bizyaev, D., Blanc, G. A., Blanton, M. R., Blomqvist, M., Bolton, A. S., Boquien, M., Borissova, J., Bovy, J., Brand t, W. N., Brinkmann, J., Brownstein, J. R., Bundy, K., Burgasser, A., Byler, N., Cano Diaz, M., Cappellari, M., Carrera, R., Cervantes Sodi, B., Chen, Y., Cherinka, B., Choi, P. D., Chung, H., Coffey, D., Comerford, J. M., Comparat, J., Covey, K., da Silva Ilha, G., da Costa, L., Dai, Y. S., Damke, G., Darling, J., Davies, R., Dawson, K., de Sainte Agathe, V., Deconto Machado, A., Del Moro, A., De Lee, N., Diamond-Stanic, A. M., Domínguez Sánchez, H., Donor, J., Drory, N., du Mas des Bourboux, H., Duckworth, C., Dwelly, T., Ebelke, G., Emsellem, E., Escoffier, S., Fernández-Trincado, J. G., Feuillet, D., Fischer, J.-L., Fleming, S. W., Fraser-McKelvie, A., Freisclad, G., Frinchaboy, P. M., Fu, H., Galbany, L., Garcia-Dias, R., García-Hernández, D. A., Garma Oehmichen, L. A., Geimba Maia, M. A., Gil-Marín, H., Grabowski, K., Gu, M., Guo, H., Ha, J., Harrington, E., Hasselquist, S., Hayes, C. R., Hearty, F., Hernandez Toledo, H., Hicks, H., Hogg, D. W., Holley-Bockelmann, K., Holtzman, J. A., Hsieh, B.-C., Hunt, J. A. S., Hwang, H. S., Ibarra-Medel, H. J., Jimenez Angel, C. E., Johnson, J., Jones, A., Jönsson, H., Kinemuchi, K., Kollmeier, J., Krawczyk, C., Kreckel, K., Kruk, S., Lacerna, I., Lan, T.-W., Lane, R. R., Law, D. R., Lee, Y.-B., Li, C., Lian, J., Lin, L., Lin, Y.-T., Lintott, C., Long, D., Longa-Peña, P., Mackereth, J. T., de la Macorra, A., Majewski, S. R., Malanushenko, O., Manchado, A., Maraston, C., Mariappan, V., Marinelli, M., Marques-Chaves, R., Masseron, T., Masters, K. L., McDermid, R. M., Medina Peña, N., Meneses-Goytia, S., Merloni, A., Merrifield, M., Meszaros, S., Min-niti, D., Minsley, R., Muna, D., Myers, A. D., Nair, P., Correa do Nascimento, J., Newman, J. A., Nitschelm, C., Olmstead, M. D., Oravetz, A., Oravetz, D., Ortega Minakata, R. A., Pace, Z., Padilla, N., Palicio, P. A., Pan, K., Pan, H.-A., Parikh, T., Parker, James, I., Peirani, S., Penny, S., Percival, W. J., Perez-Fournon, I., Peterken, T., Pinsonneault, M. H., Prakash, A., Raddick, M. J., Raichoor, A., Riffel, R. A., Riffel, R., Rix, H.-W., Robin, A. C., Roman-Lopes, A., Rose, B., Ross, A. J., Rossi, G., Rowlands, K., Rubin, K. H. R., Sánchez, S. F., Sánchez-Gallego, J. R., Sayres, C., Schaefer, A., Schiavon, R. P., Schimoia, J. S., Schlafly, E., Schlegel, D., Schneider, D. P., Schultheis, M., Seo, H.-J., Shamsi, S. J., Shao, Z., Shen, S., Shetty, S., Simonian, G., Smethurst, R. J., Sobek, J., Souter, B. J., Spindler, A., Stark, D. V., Stassun, K. G., Steinmetz, M., Storchi-Bergmann, T., Stringfellow, G. S., Suárez, G., Sun, J., Taghizadeh-Popp, M., Talbot, M. S., Tayar, J., Thakar, A. R., Thomas, D., Tissera, P., Tojeiro, R., Troup, N. W., Unda-Sanzana, E., Valenzuela, O., Vargas-Magaña, M., Vázquez-Mata, J. A., Wake, D., Weaver, B. A., Weijmans, A.-M., Westfall, K. B., Wild, V., Wilson, J., Woods, E., Yan, R., Yang, M., Zamora, O., Zasowski, G., Zhang, K., Zheng, Z., Zheng, Z., Zhu, G., Zinn, J. C., & Zou, H. 2019, *Astrophysical Journal Supplement*, 240, 23

Akins, H. B., Christensen, C. R., Brooks, A. M., Munshi, F., Applebaum, E., Angelhardt, A., & Chamberland, L. 2020, arXiv e-prints, arXiv:2008.02805

Albaret, F. D., Allende Prieto, C., Almeida, A., Anders, F., Anderson, S., Andrews,

B. H., Aragón-Salamanca, A., Argudo-Fernández, M., Armengaud, E., Aubourg, E., Avila-Reese, V., Badenes, C., Bailey, S., Barbuy, B., Barger, K., Barrera-Ballesteros, J., Bartosz, C., Basu, S., Bates, D., Battaglia, G., Baumgarten, F., Baur, J., Bautista, J., Beers, T. C., Belfiore, F., Bershady, M., Bertran de Lis, S., Bird, J. C., Bizyaev, D., Blanc, G. A., Blanton, M., Blomqvist, M., Bolton, A. S., Borissova, J., Bovy, J., Brandt, W. N., Brinkmann, J., Brownstein, J. R., Bundy, K., Burtin, E., Busca, N. G., Orlando Camacho Chavez, H., Cano Díaz, M., Cappellari, M., Carrera, R., Chen, Y., Cherinka, B., Cheung, E., Chiappini, C., Chojnowski, D., Chuang, C.-H., Chung, H., Cirolini, R. F., Clerc, N., Cohen, R. E., Comerford, J. M., Comparat, J., Correa do Nascimento, J., Cousinou, M.-C., Covey, K., Crane, J. D., Croft, R., Cunha, K., Darling, J., Davidson, James W., J., Dawson, K., Da Costa, L., Da Silva Ilha, G., Deconto Machado, A., Delubac, T., De Lee, N., De la Macorra, A., De la Torre, S., Diamond-Stanic, A. M., Donor, J., Downes, J. J., Drory, N., Du, C., Du Mas des Bourboux, H., Dwelly, T., Ebelke, G., Eigenbrot, A., Eisenstein, D. J., Elsworth, Y. P., Emsellem, E., Eracleous, M., Escoffier, S., Evans, M. L., Falcón-Barroso, J., Fan, X., Favole, G., Fernandez-Alvar, E., Fernandez-Trincado, J. G., Feuillet, D., Fleming, S. W., Font-Ribera, A., Freislad, G., Frinchaboy, P., Fu, H., Gao, Y., Garcia, R. A., Garcia-Dias, R., Garcia-Hernández, D. A., Garcia Pérez, A. E., Gaulme, P., Ge, J., Geisler, D., Gillespie, B., Gil Marin, H., Girardi, L., Goddard, D., Gomez Maqueo Chew, Y., Gonzalez-Perez, V., Grabowski, K., Green, P., Grier, C. J., Grier, T., Guo, H., Guy, J., Hagen, A., Hall, M., Harding, P., Harley, R. E., Hasselquist, S., Hawley, S., Hayes, C. R., Hearty, F., Hekker, S., Hernandez Toledo, H., Ho, S., Hogg, D. W., Holley-Bockelmann, K., Holtzman, J. A., Holzer, P. H., Hu, J., Huber, D., Hutchinson, T. A., Hwang, H. S., Ibarra-Medel, H. J., Ivans, I. I., Ivory, K., Jaehnig, K., Jensen, T. W., Johnson, J. A., Jones, A., Jullo, E., Kallinger, T., Kinemuchi, K., Kirkby, D., Klaene, M., Kneib, J.-P., Kollmeier, J. A., Lacerna, I., Lane, R. R., Lang, D., Laurent, P., Law, D. R., Leauthaud, A., Le Goff, J.-M., Li, C., Li, C., Li, N., Li, R., Liang, F.-H., Liang, Y., Lima, M., Lin, L., Lin, L., Lin, Y.-T., Liu, C., Long, D., Lucatello, S., MacDonald, N., MacLeod, C. L., Mackereth, J. T., Mahadevan, S., Maia, M. A. G., Maiolino, R., Majewski, S. R., Malanushenko, O., Malanushenko, V., Mallmann, N. D., Manchado, A., Maraston, C., Marques-Chaves, R., Martinez Valpuesta, I., Masters, K. L., Mathur, S., McGreer, I. D., Merloni, A., Merrifield, M. R., Mészáros, S., Meza, A., Miglio, A., Minchev, I., Molaverdikhani, K., Montero-Dorta, A. D., Mosser, B., Muna, D., Myers, A., Nair, P., Nandra, K., Ness, M., Newman, J. A., Nichol, R. C., Nidever, D. L., Nitschelm, C., O'Connell, J., Oravetz, A., Oravetz, D. J., Pace, Z., Padilla, N., Palanque-Delabrouille, N., Pan, K., Parejko, J., Paris, I., Park, C., Peacock, J. A., Peirani, S., Pellejero-Ibanez, M., Penny, S., Percival, W. J., Percival, J. W., Perez-Fournon, I., Petitjean, P., Pieri, M., Pinsonneault, M. H., Pisani, A., Prada, F., Prakash, A., Price-Jones, N., Raddick, M. J., Rahman, M., Raichoor, A., Barboza Rembold, S., Reyna, A. M., Rich, J., Richstein, H., Ridl, J., Riffel, R. A., Riffel, R., Rix, H.-W., Robin, A. C., Rockosi, C. M., Rodríguez-Torres, S., Rodrigues, T. S., Roe, N., Roman Lopes, A., Román-Zúñiga, C., Ross, A. J., Rossi, G., Ruan, J., Ruggeri, R., Runnoe, J. C., Salazar-Albornoz, S., Salvato, M., Sanchez, S. F., Sanchez, A. G., Sanchez-Gallego, J. R., Santiago, B. X., Schiavon, R., Schimoia, J. S., Schlafly, E., Schlegel, D. J., Schneider, D. P., Schönrich, R., Schultheis, M.,

- Schwöpe, A., Seo, H.-J., Serenelli, A., Sesar, B., Shao, Z., Shetrone, M., Shull, M., Silva Aguirre, V., Skrutskie, M. F., Slosar, A., Smith, M., Smith, V. V., Sobek, J., Somers, G., Souto, D., Stark, D. V., Stassun, K. G., Steinmetz, M., Stello, D., Storchi Bergmann, T., Strauss, M. A., Streblyanska, A., Stringfellow, G. S., Suarez, G., Sun, J., Taghizadeh-Popp, M., Tang, B., Tao, C., Tayar, J., Tembe, M., Thomas, D., Tinker, J., Tojeiro, R., Tremonti, C., Troup, N., Trump, J. R., Unda-Sanzana, E., Valenzuela, O., Van den Bosch, R., Vargas-Magaña, M., Vazquez, J. A., Villanova, S., Vivek, M., Vogt, N., Wake, D., Walterbos, R., Wang, Y., Wang, E., Weaver, B. A., Weijmans, A.-M., Weinberg, D. H., Westfall, K. B., Whelan, D. G., Wilcots, E., Wild, V., Williams, R. A., Wilson, J., Wood-Vasey, W. M., Wylezalek, D., Xiao, T., Yan, R., Yang, M., Ybarra, J. E., Yeche, C., Yuan, F.-T., Zakamska, N., Zamora, O., Zasowski, G., Zhang, K., Zhao, C., Zhao, G.-B., Zheng, Z., Zheng, Z., Zhou, Z.-M., Zhu, G., Zinn, J. C., & Zou, H. 2017, *Astrophysical Journal Supplement*, 233, 25
- Behroozi, P. S., Wechsler, R. H., & Wu, H.-Y. 2013a, *The Astrophysical Journal*, 762, 109
- Behroozi, P. S., Wechsler, R. H., Wu, H.-Y., Busha, M. T., Klypin, A. A., & Primack, J. R. 2013b, *The Astrophysical Journal*, 763, 18
- Belokurov, V., Walker, M. G., Evans, N. W., Gilmore, G., Irwin, M. J., Just, D., Koposov, S., Mateo, M., Olszewski, E., Watkins, L., & Wyrzykowski, L. 2010, *The Astrophysical Journal Letters*, 712, L103
- Belokurov, V., Walker, M. G., Evans, N. W., Gilmore, G., Irwin, M. J., Mateo, M., Mayer, L., Olszewski, E., Bechtold, J., & Pickering, T. 2009, *Monthly Notices of the Royal Astronomy Society*, 397, 1748
- Belokurov, V., Zucker, D. B., Evans, N. W., Kleyna, J. T., Koposov, S., Hodgkin, S. T., Irwin, M. J., Gilmore, G., Wilkinson, M. I., Fellhauer, M., Bramich, D. M., Hewett, P. C., Vidrih, S., De Jong, J. T. A., Smith, J. A., Rix, H. W., Bell, E. F., Wyse, R. F. G., Newberg, H. J., Mayeur, P. A., Yanny, B., Rockosi, C. M., Gnedin, O. Y., Schneider, D. P., Beers, T. C., Barentine, J. C., Brewington, H., Brinkmann, J., Harvanek, M., Kleinman, S. J., Krzesinski, J., Long, D., Nitta, A., & Snedden, S. A. 2007, *The Astrophysical Journal*, 654, 897
- Belokurov, V., Zucker, D. B., Evans, N. W., Wilkinson, M. I., Irwin, M. J., Hodgkin, S., Bramich, D. M., Irwin, J. M., Gilmore, G., Willman, B., Vidrih, S., Newberg, H. J., Wyse, R. F. G., Fellhauer, M., Hewett, P. C., Cole, N., Bell, E. F., Beers, T. C., Rockosi, C. M., Yanny, B., Grebel, E. K., Schneider, D. P., Lupton, R., Barentine, J. C., Brewington, H., Brinkmann, J., Harvanek, M., Kleinman, S. J., Krzesinski, J., Long, D., Nitta, A., Smith, J. A., & Snedden, S. A. 2006, *The Astrophysical Journal Letters*, 647, L111
- Benson, A. 2011, *Galacticus: A Semi-Analytic Model of Galaxy Formation*
- Blitz, L. & Rosolowsky, E. 2006, *The Astrophysical Journal*, 650, 933

- Bovill, M. S. & Ricotti, M. 2011, *The Astrophysical Journal*, 741, 17
- Boylan-Kolchin, M., Springel, V., White, S. D. M., Jenkins, A., & Lemson, G. 2009, *Monthly Notices of the Royal Astronomy Society*, 398, 1150
- Busha, M. T., Wechsler, R. H., Behroozi, P. S., Gerke, B. F., Klypin, A. A., & Primack, J. R. 2011, *The Astrophysical Journal*, 743, 117
- Cantiello, M., Blakeslee, J. P., Ferrarese, L., Côté, P., Roediger, J. C., Raimondo, G., Peng, E. W., Gwyn, S., Durrell, P. R., & Cuillandre, J.-C. 2018, *The Astrophysical Journal*, 856, 126
- Chisholm, J. & Matsushita, S. 2016, *The Astrophysical Journal*, 830, 72
- Colless, M. *The 2dF Galaxy Redshift Survey*, ed. P. Murdin, E5485
- Crnojevic, D. 2020, in *American Astronomical Society Meeting Abstracts*, American Astronomical Society Meeting Abstracts, 207.13
- Dalal, N., Lithwick, Y., & Kuhlen, M. 2010, arXiv e-prints, arXiv:1010.2539
- Drlica-Wagner, A., Bechtol, K., Allam, S., Tucker, D. L., Gruendl, R. A., Johnson, M. D., Walker, A. R., James, D. J., Nidever, D. L., Olsen, K. A. G., Wechsler, R. H., Cioni, M. R. L., Conn, B. C., Kuehn, K., Li, T. S., Mao, Y. Y., Martin, N. F., Neilsen, E., Noel, N. E. D., Pieres, A., Simon, J. D., Stringfellow, G. S., van der Marel, R. P., & Yanny, B. 2016, *The Astrophysical Journal Letters*, 833, L5
- Drlica-Wagner, A., Bechtol, K., Rykoff, E. S., Luque, E., Queiroz, A., Mao, Y. Y., Wechsler, R. H., Simon, J. D., Santiago, B., Yanny, B., Balbinot, E., Dodelson, S., Fausti Neto, A., James, D. J., Li, T. S., Maia, M. A. G., Marshall, J. L., Pieres, A., Stringer, K., Walker, A. R., Abbott, T. M. C., Abdalla, F. B., Allam, S., Benoit-Lévy, A., Bernstein, G. M., Bertin, E., Brooks, D., Buckley-Geer, E., Burke, D. L., Carnero Rosell, A., Carrasco Kind, M., Carretero, J., Crocce, M., da Costa, L. N., Desai, S., Diehl, H. T., Dietrich, J. P., Doel, P., Eifler, T. F., Evrard, A. E., Finley, D. A., Flaugher, B., Fosalba, P., Frieman, J., Gaztanaga, E., Gerdes, D. W., Gruen, D., Gruendl, R. A., Gutierrez, G., Honscheid, K., Kuehn, K., Kuropatkin, N., Lahav, O., Martini, P., Miquel, R., Nord, B., Ogando, R., Plazas, A. A., Reil, K., Roodman, A., Sako, M., Sanchez, E., Scarpine, V., Schubnell, M., Sevilla-Noarbe, I., Smith, R. C., Soares-Santos, M., Sobreira, F., Suchyta, E., Swanson, M. E. C., Tarle, G., Tucker, D., Vikram, V., Wester, W., Zhang, Y., Zuntz, J., & DES Collaboration. 2015, *The Astrophysical Journal*, 813, 109
- Errani, R. & Peñarrubia, J. 2020, *Monthly Notices of the Royal Astronomy Society*, 491, 4591
- Ferland, G. J., Chatzikos, M., Guzmán, F., Lykins, M. L., van Hoof, P. A. M., Williams, R. J. R., Abel, N. P., Badnell, N. R., Keenan, F. P., Porter, R. L., & Stancil, P. C. 2017, , 53, 385

- Fischera, J. & Schmidt, B. 2009, in *Astronomical Society of the Pacific Conference Series*, Vol. 414, *Cosmic Dust - Near and Far*, ed. T. Henning, E. Grün, & J. Steinacker, 266
- Font, A. S., Benson, A. J., Bower, R. G., Frenk, C. S., Cooper, A., De Lucia, G., Helly, J. C., Helmi, A., Li, Y. S., McCarthy, I. G., Navarro, J. F., Springel, V., Starkeburg, E., Wang, J., & White, S. D. M. 2011, *Monthly Notices of the Royal Astronomy Society*, 417, 1260
- Frebel, A., Kirby, E. N., & Simon, J. D. 2010, , 464, 72
- Galli, D. & Palla, F. 1998, *Astronomy and Astrophysics*, 335, 403
- Garrison-Kimmel, S., Boylan-Kolchin, M., Bullock, J. S., & Lee, K. 2014, *Monthly Notices of the Royal Astronomy Society*, 438, 2578
- Gerard Lemson & the Virgo Consortium. 2020, *Halo and Galaxy Formation Histories from the Millennium Simulation*
- Gnedin, N. Y. 2000, *The Astrophysical Journal*, 542, 535
- Gottloeber, S., Hoffman, Y., & Yepes, G. 2010, arXiv e-prints, arXiv:1005.2687
- Griest, K. *WIMPs and MACHOs*, ed. P. Murdin, E2634
- Hahn, O. & Abel, T. 2011, *Monthly Notices of the Royal Astronomy Society*, 415, 2101
- Hayashi, E., Navarro, J. F., Taylor, J. E., Stadel, J., & Quinn, T. 2003, *The Astrophysical Journal*, 584, 541
- Heesen, V., Basu, A., Brinks, E., Heald, G., Fletcher, A., Horellou, C., Hoefft, M., & Chyży, K. 2019, in *Dwarf Galaxies: From the Deep Universe to the Present*, ed. K. B. W. McQuinn & S. Stierwalt, Vol. 344, 255–258
- Heger, A. & Woosley, S. E. 2002, *The Astrophysical Journal*, 567, 532
- Henriques, B. M. B., White, S. D. M., Lilly, S. J., Bell, E. F., Bluck, A. F. L., & Terrazas, B. A. 2019, *Monthly Notices of the Royal Astronomy Society*, 485, 3446
- Hillebrandt, W. & Niemeyer, J. C. 2000, *Annual Review of Astronomy and Astrophysics*, 38, 191
- Hopkins, P. F., Kereš, D., Oñorbe, J., Faucher-Giguère, C.-A., Quataert, E., Murray, N., & Bullock, J. S. 2014, *Monthly Notices of the Royal Astronomy Society*, 445, 581
- Irwin, M. J., Belokurov, V., Evans, N. W., Ryan-Weber, E. V., de Jong, J. T. A., Koposov, S., Zucker, D. B., Hodgkin, S. T., Gilmore, G., Prema, P., Hebb, L., Begum, A., Fellhauer, M., Hewett, P. C., Kennicutt, R. C., J., Wilkinson, M. I., Bramich, D. M., Vidrih, S., Rix, H. W., Beers, T. C., Barentine, J. C., Brewington, H., Harvanek, M., Krzesinski, J., Long, D., Nitta, A., & Snedden, S. A. 2007, *The Astrophysical Journal Letters*, 656, L13

- Jeon, M., Pawlik, A. H., Bromm, V., & Milosavljević, M. 2014, *Monthly Notices of the Royal Astronomy Society*, 444, 3288
- Karachentsev, I. D., Sharina, M. E., Makarov, D. I., Dolphin, A. E., Grebel, E. K., Geisler, D., Guhathakurta, P., Hodge, P. W., Karachentseva, V. E., Sarajedini, A., & Seitzer, P. 2002, *Astronomy and Astrophysics*, 389, 812
- Karachentseva, V. E. & Karachentsev, I. D. 1998, *Astronomy and Astrophysics Supplement*, 127, 409
- Karachentseva, V. E., Karachentsev, I. D., & Richter, G. M. 1999, *Astronomy and Astrophysics Supplement*, 135, 221
- Kennicutt, Robert C., J. 1998, *The Astrophysical Journal*, 498, 541
- Knollmann, S. R. & Knebe, A. 2009, *Astrophysical Journal Supplement*, 182, 608
- Krumholz, M. R., McKee, C. F., & Tumlinson, J. 2009, *The Astrophysical Journal*, 699, 850
- Lin, D. N. C. & Murray, S. D. 1994, in *European Southern Observatory Conference and Workshop Proceedings*, Vol. 49, *European Southern Observatory Conference and Workshop Proceedings*, 535
- Liu, L., Gerke, B. F., Wechsler, R. H., Behroozi, P. S., & Busha, M. T. 2011, *The Astrophysical Journal*, 733, 62
- Lu, Y., Benson, A., Wetzel, A., Mao, Y.-Y., Tonnesen, S., Peter, A. H. G., Boylan-Kolchin, M., & Wechsler, R. H. 2017, *The Astrophysical Journal*, 846, 66
- Martin, N. F., Ibata, R. A., Lewis, G. F., McConnachie, A., Babul, A., Bate, N. F., Bernard, E., Chapman, S. C., Collins, M. M. L., Conn, A. R., Crnojević, D., Fardal, M. A., Ferguson, A. M. N., Irwin, M., Mackey, A. D., McMonigal, B., Navarro, J. F., & Rich, R. M. 2016, *The Astrophysical Journal*, 833, 167
- McConnachie, A. W. 2012, *The Astronomical Journal*, 144, 4
- Nagashima, M., Lacey, C. G., Baugh, C. M., Frenk, C. S., & Cole, S. 2005, *Monthly Notices of the Royal Astronomy Society*, 358, 1247
- Oppenheimer, B. D. & Davé, R. 2008, *Monthly Notices of the Royal Astronomy Society*, 387, 577
- Peñarrubia, J., Navarro, J. F., & McConnachie, A. W. 2008, *The Astrophysical Journal*, 673, 226
- Planck Collaboration, Ade, P. A. R., Aghanim, N., Arnaud, M., Ashdown, M., Aumont, J., Baccigalupi, C., Banday, A. J., Barreiro, R. B., Bartolo, N., Battaner, E., Battye, R., Benabed, K., Benoît, A., Benoit-Lévy, A., Bernard, J. P., Bersanelli, M., Bielewicz, P., Bock, J. J., Bonaldi, A., Bonavera, L., Bond, J. R., Borrill, J., Bouchet, F. R.,

Bucher, M., Burigana, C., Butler, R. C., Calabrese, E., Cardoso, J. F., Catalano, A., Challinor, A., Chamballu, A., Chiang, H. C., Christensen, P. R., Church, S., Clements, D. L., Colombi, S., Colombo, L. P. L., Combet, C., Couchot, F., Coulais, A., Crill, B. P., Curto, A., Cuttaia, F., Danese, L., Davies, R. D., Davis, R. J., de Bernardis, P., de Rosa, A., de Zotti, G., Delabrouille, J., Désert, F. X., Diego, J. M., Dole, H., Donzelli, S., Doré, O., Douspis, M., Ducout, A., Dupac, X., Efstathiou, G., Elsner, F., Enßlin, T. A., Eriksen, H. K., Fergusson, J., Finelli, F., Forni, O., Frailis, M., Fraisse, A. A., Franceschi, E., Frejsel, A., Galeotta, S., Galli, S., Ganga, K., Giard, M., Giraud-Héraud, Y., Gjerløw, E., González-Nuevo, J., Górski, K. M., Gratton, S., Gregorio, A., Gruppuso, A., Gudmundsson, J. E., Hansen, F. K., Hanson, D., Harrison, D. L., Heavens, A., Helou, G., Henrot-Versillé, S., Hernández-Monteagudo, C., Herranz, D., Hildebrandt, S. R., Hivon, E., Hobson, M., Holmes, W. A., Hornstrup, A., Hovest, W., Huang, Z., Huppenberger, K. M., Hurier, G., Jaffe, A. H., Jaffe, T. R., Jones, W. C., Juvela, M., Keihänen, E., Keskitalo, R., Kisner, T. S., Knoche, J., Kunz, M., Kurki-Suonio, H., Lagache, G., Lähteenmäki, A., Lamarre, J. M., Lasenby, A., Lattanzi, M., Lawrence, C. R., Leonardi, R., Lesgourgues, J., Levrier, F., Lewis, A., Liguori, M., Lilje, P. B., Linden-Vørnle, M., López-Cañiego, M., Lubin, P. M., Ma, Y. Z., Macías-Pérez, J. F., Maggio, G., Maino, D., Mandolesi, N., Mangilli, A., Marchini, A., Maris, M., Martin, P. G., Martinelli, M., Martínez-González, E., Masi, S., Matarrese, S., McGehee, P., Meinhold, P. R., Melchiorri, A., Mendes, L., Mennella, A., Migliaccio, M., Mitra, S., Miville-Deschênes, M. A., Moneti, A., Montier, L., Morgante, G., Mortlock, D., Moss, A., Munshi, D., Murphy, J. A., Narimani, A., Naselsky, P., Nati, F., Natoli, P., Netterfield, C. B., Nørgaard-Nielsen, H. U., Noviello, F., Novikov, D., Novikov, I., Oxborrow, C. A., Paci, F., Pagano, L., Pajot, F., Paoletti, D., Pasian, F., Patanchon, G., Pearson, T. J., Perdureau, O., Perotto, L., Perrotta, F., Pettorino, V., Piacentini, F., Piat, M., Pierpaoli, E., Pietrobon, D., Plaszczynski, S., Pointecouteau, E., Polenta, G., Popa, L., Pratt, G. W., Prézeau, G., Prunet, S., Puget, J. L., Rachen, J. P., Reach, W. T., Rebolo, R., Reinecke, M., Remazeilles, M., Renault, C., Renzi, A., Ristorcelli, I., Rocha, G., Rosset, C., Rossetti, M., Roudier, G., Rowan-Robinson, M., Rubiño-Martín, J. A., Rusholme, B., Salvatelli, V., Sandri, M., Santos, D., Savelainen, M., Savini, G., Schaefer, B. M., Scott, D., Seiffert, M. D., Shellard, E. P. S., Spencer, L. D., Stolyarov, V., Stompor, R., Sudiwala, R., Sunyaev, R., Sutton, D., Suur-Uski, A. S., Sygnet, J. F., Tauber, J. A., Terenzi, L., Toffolatti, L., Tomasi, M., Tristram, M., Tucci, M., Tuovinen, J., Valenziano, L., Valiviita, J., Van Tent, B., Viel, M., Vielva, P., Villa, F., Wade, L. A., Wandelt, B. D., Wehus, I. K., White, M., Yvon, D., Zacchei, A., & Zonca, A. 2016, *Astronomy and Astrophysics*, 594, A14

Pontzen, A. & Governato, F. 2012, *Monthly Notices of the Royal Astronomy Society*, 421, 3464

Ricotti, M. & Gnedin, N. Y. 2005, *The Astrophysical Journal*, 629, 259

Roediger, E. & Brügggen, M. 2008, *Monthly Notices of the Royal Astronomy Society*, 388, 465

Rong, Y., Puzia, T. H., Eigenthaler, P., Ordenes-Briceño, Y., Taylor, M. A., Muñoz,

- R. P., Zhang, H., Galaz, G., Alamo-Martínez, K., Ribbeck, K. X., Grebel, E. K., Ángel, S., Côté, P., Ferrarese, L., Hilker, M., Mieske, S., Miller, B. W., Sánchez-Janssen, R., & Johnston, E. J. 2019, *The Astrophysical Journal*, 883, 56
- Sawala, T., Frenk, C. S., Fattahi, A., Navarro, J. F., Bower, R. G., Crain, R. A., Dalla Vecchia, C., Furlong, M., Helly, J. C., Jenkins, A., Oman, K. A., Schaller, M., Schaye, J., Theuns, T., Trayford, J., & White, S. D. M. 2016, *Monthly Notices of the Royal Astronomy Society*, 457, 1931
- Sawala, T., Scannapieco, C., & White, S. 2012, *Monthly Notices of the Royal Astronomy Society*, 420, 1714
- Shi, Y., Helou, G., Yan, L., Armus, L., Wu, Y., Papovich, C., & Stierwalt, S. 2011, *The Astrophysical Journal*, 733, 87
- Simon, J. D. 2019, *Annual Review of Astronomy and Astrophysics*, 57, 375
- Springel, V. 2005, *Monthly Notices of the Royal Astronomy Society*, 364, 1105
- Springel, V., Wang, J., Vogelsberger, M., Ludlow, A., Jenkins, A., Helmi, A., Navarro, J. F., Frenk, C. S., & White, S. D. M. 2008, *Monthly Notices of the Royal Astronomy Society*, 391, 1685
- Springel, V., White, S. D. M., Jenkins, A., Frenk, C. S., Yoshida, N., Gao, L., Navarro, J., Thacker, R., Croton, D., Helly, J., Peacock, J. A., Cole, S., Thomas, P., Couchman, H., Evrard, A., Colberg, J., & Pearce, F. 2005, , 435, 629
- Suchkov, A. A. & Shchekinov, I. A. 1978, *Pisma v Astronomicheskii Zhurnal*, 4, 301
- Tammann, G. A. 1994, in *European Southern Observatory Conference and Workshop Proceedings*, Vol. 49, European Southern Observatory Conference and Workshop Proceedings, 3
- Taylor, M. A., Muñoz, R. P., Puzia, T. H., Mieske, S., Eigenthaler, P., & Bovill, M. S. 2016, arXiv e-prints, arXiv:1608.07285
- Tollerud, E. J., Barton, E. J., Bullock, J. S., & Trinh, C. 2011, in *EAS Publications Series*, Vol. 48, *EAS Publications Series*, ed. M. Koleva, P. Prugniel, & I. Vauglin, 455–457
- Torrealba, G., Belokurov, V., Kuposov, S. E., Bechtol, K., Drlica-Wagner, A., Olsen, K. A. G., Vivas, A. K., Yanny, B., Jethwa, P., Walker, A. R., Li, T. S., Allam, S., Conn, B. C., Gallart, C., Gruendl, R. A., James, D. J., Johnson, M. D., Kuehn, K., Kuropatkin, N., Martin, N. F., Martinez-Delgado, D., Nidever, D. L., Noël, N. E. D., Simon, J. D., Stringfellow, G. S., & Tucker, D. L. 2018, *Monthly Notices of the Royal Astronomy Society*, 475, 5085
- Torrealba, G., Belokurov, V., Kuposov, S. E., Li, T. S., Walker, M. G., Sanders, J. L., Geringer-Sameth, A., Zucker, D. B., Kuehn, K., Evans, N. W., & Dehnen, W. 2019, *Monthly Notices of the Royal Astronomy Society*, 488, 2743

- van Dokkum, P., Abraham, R., Brodie, J., Conroy, C., Danieli, S., Merritt, A., Mowla, L., Romanowsky, A., & Zhang, J. 2016, *The Astrophysical Journal Letters*, 828, L6
- Villaume, A., Brodie, J., Conroy, C., Romanowsky, A. J., & van Dokkum, P. 2017, *The Astrophysical Journal Letters*, 850, L14
- Vogelsberger, M., Genel, S., Springel, V., Torrey, P., Sijacki, D., Xu, D., Snyder, G., Nelson, D., & Hernquist, L. 2014, *Monthly Notices of the Royal Astronomy Society*, 444, 1518
- Walsh, S. M., Jerjen, H., & Willman, B. 2007, *The Astrophysical Journal Letters*, 662, L83
- White, S. D. M. 1988, in *Astronomical Society of the Pacific Conference Series*, Vol. 5, *The Minnesota lectures on Clusters of Galaxies and Large-Scale Structure*, ed. J. M. Dickey, 197–229
- Whiting, A. B., Irwin, M. J., & Hau, G. K. T. 1997, *The Astronomical Journal*, 114, 996
- Williamson, D., Martel, H., & Romeo, A. B. 2016, *The Astrophysical Journal*, 831, 1
- Willman, B., Blanton, M. R., West, A. A., Dalcanton, J. J., Hogg, D. W., Schneider, D. P., Wherry, N., Yanny, B., & Brinkmann, J. 2005, *The Astronomical Journal*, 129, 2692
- Wolf, J., Martinez, G. D., Bullock, J. S., Kaplinghat, M., Geha, M., Muñoz, R. R., Simon, J. D., & Avedo, F. F. 2010, *Monthly Notices of the Royal Astronomy Society*, 406, 1220
- Zaroubi, S. *The Epoch of Reionization*, ed. T. Wiklind, B. Mobasher, & V. Bromm, Vol. 396, 45
- Zucker, D. B., Belokurov, V., Evans, N. W., Kleyna, J. T., Irwin, M. J., Wilkinson, M. I., Fellhauer, M., Bramich, D. M., Gilmore, G., Newberg, H. J., Yanny, B., Smith, J. A., Hewett, P. C., Bell, E. F., Rix, H. W., Gnedin, O. Y., Vidrih, S., Wyse, R. F. G., Willman, B., Grebel, E. K., Schneider, D. P., Beers, T. C., Kniazev, A. Y., Barentine, J. C., Brewington, H., Brinkmann, J., Harvanek, M., Kleinman, S. J., Krzesinski, J., Long, D., Nitta, A., & Snedden, S. A. 2006, *The Astrophysical Journal Letters*, 650, L41

VITA

Sachi Weerasooriya was born March 11th, 1994, in Kandy, Sri Lanka. She is the youngest daughter of Wijeratne Weerasooriya and Muthumenike Kulasekare. A 2013 graduate of Hillwood College Kandy, Sri Lanka she received a Bachelor of Science degree with a double major in Mathematics and Physics from Midwestern State University, Wichita Falls in 2018. In August, 2018, she enrolled in graduate study at Texas Christian University, and is working towards her doctorate in Astronomy. Since August, 2018, she has been an teaching assistant in Astronomy and Physics.

Personal Background	Sachi Weerasooriya Fort Worth, TX Daughter of Wijeratne and Muthumenike Weerasooriya
Education	Advanced Level, Hillwood College, Kandy, Sri Lanka, 2013 Bachelor of Science, Physics and Mathematics, Midwestern State University, Fort Worth, TX, 2018
Experience	Teaching assistantship, Midwestern State University, Wichita Falls, TX, 2015-2018 Math/Physics Tutor, Midwestern State University, Wichita Falls, TX, 2015-2018 Teaching assistantship, Texas Christian University, Fort Worth, 2018-2020
Professional Memberships	American Astronomical Society International Students Association (Texas Christian University) International Students Association (Midwestern State University) Sigma Phi Sigma Pi Mu Epsilon

ABSTRACT

MODELING DWARF SATELLITES OF THE MILKY WAY

by Sachi Weerasooriya, MSc., 2020
Department of Physics and Astronomy
Texas Christian University

Mia S. Bovill Assistant Professor of Physics

Dwarf galaxies are the most abundant type of galaxies in the universe. They are the building blocks of hierarchical structure formation, and their shallow gravitational potentials make them extremely sensitive to internal and environmental feedback (e.g. star formation, ram pressure stripping). Their sensitivity makes them excellent probes of the physics of star formation. While the Milky Way type galaxies are well simulated with hydrodynamic simulations, the study of dwarf populations beyond the Local Group remains largely unexplored. Hence, how universal star formation processes are in dwarf galaxies is undetermined. In this project, we determine the parameters of a semi-analytic model (SAM), which will best fit the extensive observations and hydrodynamic simulations available for Milky Way satellites using high-resolution N body simulation. This will allow us to calibrate our SAM for well-known Milky Way satellites, thereby allowing us to explore the stellar physics of local volume dwarf galaxies in the future.